Development of a Darkfield Internal Reflection Illumination (DIRI) Microscopy for Biomedical Applications

	Tohoku University
	11301 17110
URL	http://hdl.handle.net/10097/00096755

Development of a Darkfield Internal Reflection Illumination (DIRI) Microscopy for Biomedical Applications

（医工学への応用を目指した暗視野反射照明顕微鏡の開発）

Yoshihiro Kawano
(Doctoral Program in Biomedical Engineering)

Submitted to the Graduate School of
Biomedical Engineering
in Partial Fulfillment of the Requirements
for the Degree of Doctor of Philosophy in
Biomedical Engineering

at the
Tohoku University

January 2016

Table of Contents

Acknowledgements

I would like to express my sincere gratitude to my advisor Prof. Takuji Ishikawa for his continuous support of my Ph.D. study and related research, for his patience, motivation, and immense knowledge. His guidance helped me throughout the research and writing of this thesis. He has been an excellent advisor and mentor for my Ph.D. study.

Second, I would like to sincerely thank Prof. Takami Yamaguchi, in Recurrent Education, for the Development of Engineering Enhanced Medicine (REDEEM). He gave me an opportunity to attend the REDEEM course. If I had not met Prof. Yamaguchi, I would not have thought to enter Tohoku University. Without his valuable support it would not be possible to do this research.

I would like to thank the rest of my thesis committee: Prof. Yoshifumi Saijo, Prof. Yuji Matsuura, and Ass. Prof. Makoto Kanzaki, for their insightful comments and encouragement, but also for the hard questions which incented me to widen my research from various perspectives.

I would like to thank someone who gave me great motivation for lifelong study -- Prof. Masako Sasaki, Tokai University. She was my undergraduate course adviser. She explained to me about the importance of lifelong education. Prof. Sasaki also advised me in my studies from the point of view of Chemistry and Photonics. Without her valuable support it would not be possible to conduct this research.

I would like to thank my mentors and collaborators, Dr. Amy Bernard, Prof. Hong-Wei Dong, Prof. Harvey J. Karten, Prof. Atsushi Miyawaki, Dr. Kana Namiki, Ms. Julie Nyhus, Prof. Susumu Terakawa and Prof. Ikuo Tofukuji. They gave me so much advice on my research. Without their help I could not have done my scientific papers. Prof. Michael W. Davidson provided tremendous information about microscopy. Thank you very much.

My sincere thanks also go to Mr. Katsuyuki Abe, Mr. Yasushi Aono, Mr. Christopher Higgins, Mr. Brendan Brinkman, Dr. Hiroshi Ishiwata, Mr. Toru Kaneda, Mr. Tatsuo Nirei, Ms. Chino Otsuka, Dr. James Sanzo, Dr. Tobias Schilling and Mr. Keisuke Tamura in Olympus Group who helped my experiments and gave me tremendous scientific advice regarding my thesis. We had stimulating discussions and working together on various problems was enlightening. Without their valuable support it would not be possible to conduct this research.

My sincere thanks also go to Mr. Chikara Abe, Mr. Osamu Joji, Dr. Kiyotsugu Kojima, Mr. Chikara Nagano, Mr. Hidenao Tsuchiya, and Mr. Yuichi Watanabe in Olympus Group who are past and current supervisors in Olympus Corporation. They gave me a lot of support for my thesis from their supervisory, as well as scientific, points of view. Without their valuable support it would not be possible to conduct this research. And, Ms. Ilene Semiatin helped edit all contents, which I very much appreciate.

Last but not the least, I would like to thank my family, Yukako Kawano and Arisa Kawano for supporting me spiritually throughout writing this thesis and my life in general. And thank you very much to my parents for always encouraging me.

Abstract

The core of our research and development is the implementation of a new imaging method to expand the capability of the automated multi-modality microscope to encompass darkfield imaging.

Microscopy ideally collects as much information from the sample as possible. To help make this possible, imaging systems should be automated and have diverse capabilities. Sharing and analyzing the image data are also important; this requires internet of things (IoT) capability. In order to collect as much sample information as possible, the imaging technique is highly important. Because of these considerations, we selected Whole Slide Imaging (WSI) and a motorized Total Internal Reflection Fluorescence (TIRF) microscope for the base systems. These systems can provide automation. WSI was combined with many different modalities to extend the capabilities of the system to allow multi-modality imaging.

Darkfield microscopy provides the capability of observing non-stained samples. It also provides the capability of observing small samples such as nanometer-level materials. However, attaching an automated microscope to traditional darkfield is not easy and has some limitations. Oil immersion objectives, for example, always require immersion oil on the darkfield condenser, though the traditional darkfield unit is very hard to maintain. To overcome this issue, we developed a new technique -- Darkfield Internal Reflection Microscopy (DIRI). DIRI can easily be used with WSI and motorized TIRF microscopy.

DIRI is based on a very simple design. It is made of a thin, white-LED array or three-color LEDs, and these are mounted on the stage beside the sample. DIRI can be controlled from the computer. It can illuminate a wide area of the sample, and be used with high-magnification and high-numerical-aperture objective lenses very easily. Using the described setup, DIRI works well for 10×, 20×, 30x water-immersion, 40×, 60x water-immersion, and 60x oil-immersion objectives, and may work with other higher-magnification objective lenses.

Using our prototype for DIRI, we experimented with Brain tissue, TMA (tissue micro arrays) and microfluidics. The DIRI system has four main advantages over traditional darkfield: (1) no oil condenser is required for high-resolution imaging (2) there is less scatter from dust and dirt on the slide specimen (3) there is less halo, providing a more natural darkfield contrast image, (4) the motorized system produces darkfield, brightfield and fluorescence images, and (5) there is color control capability, providing a natural-color DIRI image.

Microfluidics is used increasingly for engineering and biomedical applications. Visualization of bubbles, tracer particles, and cells in a microfluidic device is important for designing a device and analyzing results. However, with conventional methods, it is difficult to observe the channel geometry and such particles simultaneously. Our results showed that the developed system could clearly visualize both microbubbles and the channel wall by utilizing brightfield and DIRI illumination simultaneously. Whole-slide imaging also was conducted successfully using this system. The tiling function significantly expands the observation area for microfluidics.

Adapting DIRI to WSI and TIRF microscopy are very useful, particularly when researchers require structural information without the use of further staining. In addition, DIRI may be useful for a wide variety of engineering and biomedical applications.

Acronyms

CCD	Charge coupled device
CFM	Conventional fluorescence microscopy
CTF	Contrast transfer function
CM	Confocal microscope
CMOS	Complementary metal–oxide–semiconductor
CTIRDF	Coherent total internal reflection dark-field
CWFM	Conventional widefield fluorescence microscopy
DAB	3, 3'-diaminobenzidine
DIC	Differential interference contrast
DIRI	Darkfield Internal Reflection Illumination
EMCCD	Electron multiplying charge coupled device
ENTl	lateral part of entorhinal cortex
FLM	Fluorescence microscope
IoT	Internet of Things
IPSF	Intensity point spread function
LED	Light emitting diode
NA	Numerical Aperture
Nd-YAG	neodymium-doped yttrium aluminum garnet; $Nd:Y_3Al_5O_{12}$
PBS	Phosphate buffered saline
PDMS	Polydimethylsiloxane
PHAL	Phaseolus vulgaris leucoagglutinin
PMT	Photomultiplier tube
PSF	Point spread function
sCMOS	scientific Complementary metal–oxide–semiconductor
SIT	Silicon-intensifier target
TIR	Total internal reflection
TIRF	Total internal reflection fluorescence
TIRFM	Total internal reflection fluorescence microscopy
TMA	Tissue micro array
TRITC	Tetramethylrhodamine isothiocyanate
WSI	Whole slide imaging

_____

Chapter 1　　Introduction

The human body is a very complicated and difficult to understand system. There are 50 to 75 trillion cells comprising the human body, and more than 20 thousand proteins are created by the genes. Optical microscopy is a key tool to investigate the structure and function of the organs in the human body.

To help understand complicated biological environments, scientists use many techniques and tools to examine biological samples, including automation, computation, imaging, image analysis technologies and IoT.

Whole Slide Imaging System (WSI) is often selected as a core imaging system to investigate biological systems. Importantly, the observation area of WSI is not limited to the field of view of the objective lens. WSI provides automated imaging, which makes it possible to observe a large-size sample. It can be connected to the internet easily and allow the sharing of information with collaborators.

Most commercially available WSI systems are capable of brightfield and fluorescence. This, however, limits the number of applications for WSI, since either fluorescent or other staining is required in order to provide sufficient contrast. DIRI was developed in order to extract more information from samples. To observe the samples, thin white LEDs were added to the DIRI system, and later, as part of this study, color DIRI was used to expand the system's capabilities. This newly developed method is a kind of darkfield microscopy, that offers significantly improved imaging capabilities.

It is also important to understand Total Internal Reflection Fluorescence (TIRF) Microscopy, which was developed in 1999. As part of this study, we incorporated TIRF microscopy with Darkfield Internal Reflection Illumination (DIRI). Using the system, we observed beads flowing in microfluidics. TIRF microscopy with DIRI was useful for microfluidics applications. Overall, we found that WSI/DIRI and TIRF/DIRI both were very helpful imaging methods for research and clinical applications. The developed systems could potentially prove useful for diagnostic applications as well.

In this chapter, I explain why I developed Darkfield Internal Reflection Illumination (DIRI). In section 1.1, I will discuss the history of a microscopy, WSI, darkfield microscopy, brain mapping, microfluidics, and TIRF microscopy. Then, this paper will discuss the requirements for my robotic microscope and IoT capability. In section 1.2, I delve into the purpose of this study. In section 1.3, I explain the structure of the thesis and describe the development of DIRI for various applications including brain research, microfluidics, and TIRF microscopy. Chapter 2 provides an overview of materials and methods. Chapter 3 delves into experimental results. Chapter 4 offers this study's conclusions.

_____

1.1 Historical background

1.1.1 Optical microscopy

There is a long history of observing a magnified image of an object. The Roman philosopher Seneca (3 B.C.E. - 65 A.D.) pointed out that water filling a glass globe could be used for magnifying purposes. And it is certainly possible that some Roman artisans may have used magnifying glasses to facilitate very fine detailed work (Hecht (2001)).

Researchers have been using optical microscopes to investigate tissue and cells for more than 400 years. The compound microscope was invented by the Dutchman Zacharias Janssen (1588-1632). The microscope's concave eyepiece was replaced with a convex lens by Francisco Fontana (1580-1656) of Naples. In 1611, Kepler published his Dioptric. He had discovered Total Internal Reflection in 1611. The law of refraction was discovered by Willebrord Snell in 1621. He was a professor at Leyden University. His discovery opened the door to modern applied optics (Hecht (2001)).

A Dutch draper and scientist, Antony Van Leeuwenhoek (1632-1723) made the first high-magnification microscope. At that time, most microscopes were achieving a maximum of 50x magnification. Van Leeuwenhoek made a 270x microscope that had a single lens and was handheld. Van Leeuwenhoek achieved greater success than his contemporaries by developing a microscope created via the grinding and polishing of a ball lens. He used this lens to make the world's first practical microscope (History of the microscope.org). Joseph Jackson Lister created an achromatic lens to eradicate the chromatic effect caused by different wavelengths of light in 1826. Philipp Ludwig von Seidel decomposed first-order monochromatic aberrations into five constituent aberrations in 1857. They are now commonly referred to as the five Seidel Aberrations. His idea of aberrations is still used when engineers are developing new microscopes.

The optical microscope is widely used for biomedical research. The microscope is generally considered one of the easiest, most direct and least expensive methods for observing specimens at higher resolution. One of the most widely used optical microscopy methods is fluorescence. With the wide variety of molecular tags available today, scientists consider fluorescence one of the techniques of choice for collecting data on biological samples.

These days, the optical microscope serves as a convenient tool for observing organisms from whole (small) organisms, to the organ, tissue, cell, and even molecular level. The microscope is applicable for many different observation methods including brightfield, phase contrast, polarized light, differential interference contrast (DIC), darkfield, fluorescence and two-photon imaging. At the time the Human Genome Project was launched, scientists greatly expanded the number of chemical and biological imaging tags for fluorescence microscopy. Thus, imaging methods have been improved for analyzing biological samples such as tissues, cells, and molecules.

Today, fluorescence microscopes are used for observing single-molecule phenomena. Some research groups use super-resolution techniques to observe individual molecules at higher resolution (Hung et al. (2009)). In our work, we did not use super-resolution microscopy. I focused instead on using basic microscopy techniques that are available to more researchers.

_____

1.1.2   Whole slide imaging

Optical microscopy is used to observe the details of tissue and cell structures. However, there are notable limitations. When a specimen is observed at low magnification and/or using a low numerical aperture (NA) objective lens, the obtained widefield image has low resolution. We had developed high-numerical-aperture (NA), low-magnification macro optical systems before. However, the NA of these systems did not reach the optical performance level that we requred (Kawano (2000)).

Using higher magnification objective lenses with greater NAs (such as a typical 20×; NA: 0.75 objective lens), resolution is improved at the expense of the field of view, which is markedly reduced. In neuroscience and other fields requiring detailed images of samples with a large area, this limitation is particularly obvious. For instance, detailed analysis of the cortex requires direct sampling and comparison of vast areas of tissue. This requires images as large as 200 × 250 mm. A resolution of at least 0.5 micrometers/pixel is needed for the observation of relevant cellular properties.

WSI is an imaging method that uses numerous microscope images to build a single high-resolution image over a much wider field of view. The technique creates a pyramidical structure for accessing any part or all of the collected image data (Fig. 1-1). This imaging method allows the display of high-resolution images over the wide areas that typically are viewed using low-resolution imaging (DICOM. WG26 Supplement 145, Draft 9).

_____
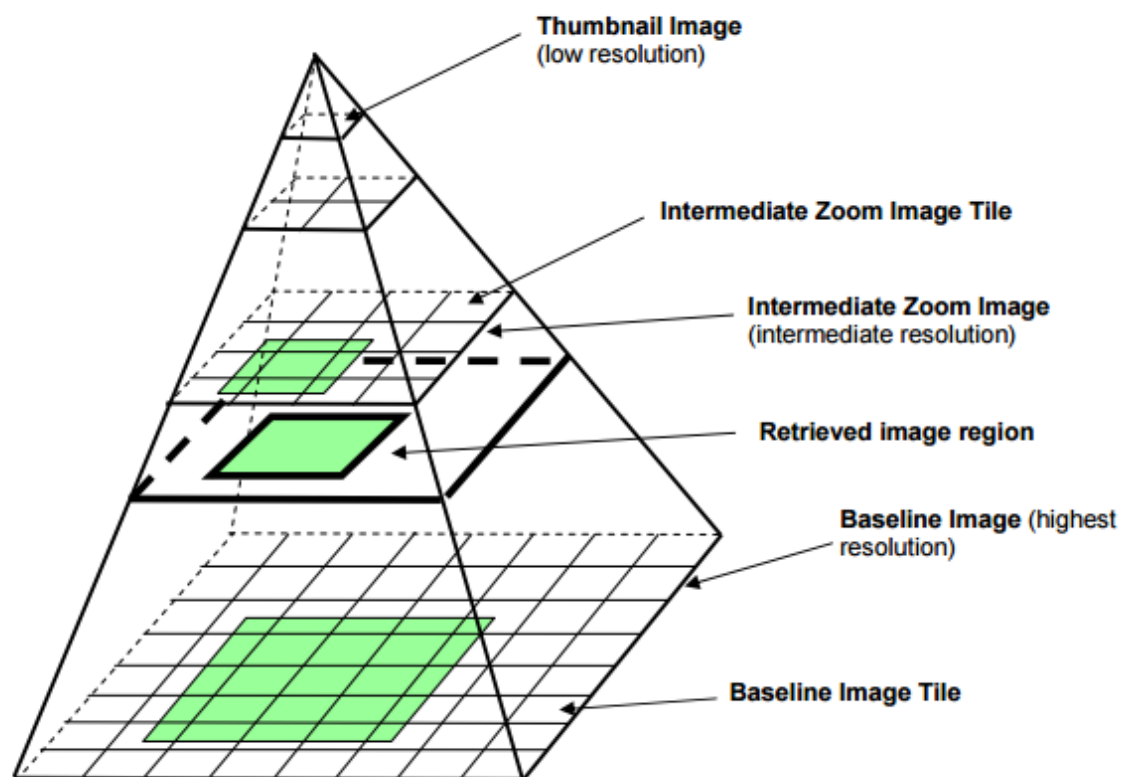
Fig. 1-1   WSI as a "Pyramid" of Image Data. From Digital Imaging and Communications in Medicine (DICOM). WG26 Supplement 145 Draft 9: Whole Slide Microscopic Image IOD and SOP Classes.

WSI produces images that simultaneously provide high resolution and a wide field of observation, extending far beyond any single field of microscopic view. For example, a brain slice can be imaged to show both overall morphology and individual neuronal detail. If we use microfluidics imaging, WSI technology helps to observe an entire area of microfluidics. Most current commercially available WSI systems are capable of brightfield and fluorescence observation. By adding additional imaging modalities, we can expand the usefulness of WSI for imaging key biological specimens.

Recently, WSI color, particularly its standardization and validation, has become a hot issue among scientists. Managing color is now considered an important aspect of imaging (Yagi (2011)).

1.1.3   Darkfield microscopy

The history of modern darkfield microscopy begins with Gage's article (1920) "Modern dark-field microscopy and the history of its development." This article said that even as early as the Descartes microscope (1637) there was some provision for transmitting light through the object. The author felt that even then, microscope users may have had the capability to change the illumination angle to observe samples with the dark background characteristic of darkfield.

The article said the first appreciation of darkfield as a method for studying microscopic objects came in papers published by Lister (1830), Reade (1838), Wenham (1850), and Edmunds (1877). It added that the appreciation of the microscopist's role in general, came only after the invention of what was called the ultra-microscope (1903) and the application of darkfield methods to the study and detection of pathologic microorganisms, especially the *Spirochaeta pallida* (1905). After the technology was developed, it applied in the manufacture of darkfield apparatus by microscope manufacturers (1904, 1905).

Darkfield illumination allows samples to be observed without the need for staining, which makes it useful for the observation of biological specimens. The typical setup required to produce an image using transmitted darkfield illumination consists of a halogen bulb with either a dedicated substage darkfield condenser or a darkfield central stop in a standard brightfield condenser. Central axial illumination is blocked by the darkfield central stop. Peripheral illumination obliquely illuminates the specimen on the slide from below. Thus, only forward-scattered or refracted light from the specimen enters the objective lens (Fig. 1-2 (a)). This creates darkfield images. If the refractive index of the sample changes, an image with a higher signal-to-noise ratio can be obtained using darkfield microscopy. If light scattered due to a refractive mismatch passes through the optical path of the darkfield microscope, the background image is dark, and the specimen appears bright. If the image background is bright, detection sensitivity is considerably reduced, resulting in conditions similar to brightfield microscopy. Enhanced detection sensitivity and contrast can be obtained using darkfield microscopy for specimens that cannot be imaged effectively using brightfield illumination.

_____

The advantage of darkfield microscopy can be described using actual samples. Fig. 1-2 (b) shows a brightfield image of a cheek cell using 60× oil with an extended magnification lens of 2.5×; the cheek sample was freshly collected and diluted in phosphate buffered solution (PBS). The image contrast was low so that it was difficult to observe the cells. A darkfield image of the cheek cells is shown in Fig. 1-2 (c); in this image, the background is very dark; thus, the granules inside the cells are clearly resolved.

Conventional darkfield units are commercially available for many standard microscopes. There are two types of darkfield condensers: dry and oil. Some phase turret condensers include the required darkfield annulus within the condenser turret. The dry darkfield condenser, schematically shown in Fig. 1-2 (a), illuminates a spot; however, the illuminated area is very limited. Normally, with 10× to 20× objective lenses of NA < 0.5, dry darkfield condensers are capable of illuminating the field of view. A dry darkfield condenser cannot be used with objective lenses with NA > 0.8, such as a 40×, NA 0.95 lens, because the illumination cone passes directly through the objective lens and eliminates the dark background of the image. Using an oil darkfield condenser to provide optical coverage, a 40× objective lens with NA = 0.95 can be used for darkfield imaging.

A common practice when taking sets of microscope images is to find the required field of view using a 10× or 20× lens, and then to switch to a higher magnification and higher NA objective lens (such as the 40×, NA 0.95 lens) for image acquisition. However, if the user needs to switch back to the 20×, NA 0.75 dry lens later on, the condenser also has to be switched back to the dry darkfield condenser. This necessitates the disruptive and somewhat laborious process of removing the oil from the slide, and requires the investigator to begin again with dry optics. The procedure of switching back and forth between dry and oil systems poses a considerable inconvenience to investigators and may introduce an unacceptable delay into the experimental protocol. This can render some experiments too arduous to perform. Thus, it can be difficult to obtain images using traditional darkfield illumination with an automated microscope.

Currently, real-time brightfield, darkfield, and phase contrast imaging in an LED-array microscopes are available. This technology uses two-dimensional LED arrays to illuminate the sample. The illumination light pass is basically on the above the sample and the LED is not located on the side of the sample, it is located on above the sample (Liu et. al. (2014)). The location for the LED is not same as DIRI. This Liu's technology is a useful technology; however, whether darkfield illumination can be used depends on the condenser lens's numerical aperture. However, DIRI illumination does not use a condenser lens. So, we have enhanced capability to attach various objective lenses such as oil objectives or higher-NA lenses.

Recently, some scientists are using nanoparticles as imaging agents. Noble metal nanoparticles exhibit a plasmon resonance that provides them with unique optical properties. The spectral characteristics are related to particle diameter and size. The nanoparticles enable simultaneous molecular imaging and environmental sensing through the use of darkfield microscopy (Wax et. Al. (2009)). In this case, illumination light employed should be of a shorter wavelength. DIRI is capable of changing illumination wavelengths. This wavelength changing capability has proven to be useful.

_____
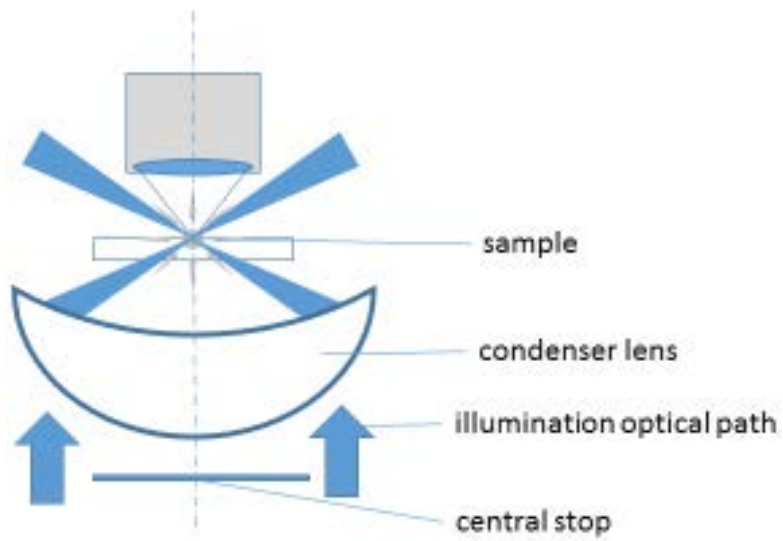
(a)

(b)   (c)

Fig. 1-2 Transmitted darkfield microscope, with cheek cell images captured using brightfield and darkfield microscopy.

(a) darkfield condenser. (b) brightfield microscopy image (c) darkfield microscopy image

_____

1.1.4 **Brain mapping**

In the past, scientists including Korbinian Brodmann and Cécile and Oskar Vogt used high-resolution emulsion films designed for astronomy to attempt to capture the fine detail essential to their cytoarchitectural analysis. However, the larger field of view in their photographs resulted in lower optical resolution consequent to the limitations of the NA. In order to compensate for the optical and emulsion deficiencies of their photographic apparatus, they attempted to capture the complexity of the neural tissue by using a microscope drawing tube to sketch a high-resolution image in widefield (Gilbert et al. (1983)). But sketching multiple fields of microscope images proved to be difficult and time consuming, and it often introduced errors in the system, including both major sampling bias and inaccuracies arising from the burdensome procedure of attempting to represent the cell density and cell size accurately. We recognized that the ability to observe in widefield using higher resolution is very important.

Neuroscientists have recognized several advantages that WSI imaging presents when compared with conventional optical microscopy. Remote viewing, data sharing, and various forms of data mining are just some of these advantages (Mikula et al. (2007); Bohland et al. (2009)). The large field of view is another advantage: the brain has complicated and inter-tangled masses of neural networks and structures that extend beyond the field of view of almost any conventional microscope objective lens.

WSI has enabled neuroscientists to provide internet-enabled high-resolution brain maps and atlases to display neural connections and image protein expression (Mikula, et al. (2007); Bohland et al. (2009); Lein et al. (2007); Ng et al. (2009)). Virtual slide technology provides the high-resolution imaging required for widefield observation. It also provides an excellent tool for observing brain neural systems and structures that are widely distributed over many serial sections. If we use most current microscope technology, archiving a whole mouse brain takes more than a day. And it is not easy for many laboratory data systems to manage more than several thousand images. One of the most powerful applications of WSI is the ability to scan a complete set of serial sections within a short period of time and transfer the data to an all-digital format. This advantage greatly simplifies the task of analysis and allows researchers to share research results with colleagues thousands of miles away.

Darkfield microscopy, in particular, has been widely used for many years to detect silver grains consequent to autoradiography (ARG), gene expression, and immunohistochemically-labeled cell bodies in sliced brain tissue (Reyes-Irisarri et al. (2005)). It also has been used to observe and analyze complex patterns of axonal projections labeled with anterograde tracers, providing enhanced signal-to-noise ratios (SNR). Darkfield images can reveal exquisitely detailed morphologies, such as axonal boutons and varicosities (Miyawaki et al. (1996), Dong et al. (2001, 2003)).

Dr. Sebastian Seung gave a TED Talk (2010) in which he said, "you are more than your genes. You are your connectome." Scientists believe that the connectome provides inside of memory information in brain. Unfortunately, we cannot read all of the connectome for the human brain at this time. The human brain is big and complicated. Currently, we only know the connectome for Nematoda. If we could access and observe all of the neural connections made by the human brain, then we could potentially copy or at least better understand all of human memories. Scientists are interested to know much more about human brain connectivity. This is one of the reasons scientists are interested in building a network map of the brain to understand the anatomical and functional connectivity in the brain. If we can read the brain, we can produce a body of data that will facilitate research into brain disorders

_____

such as dyslexia, autism, Alzheimer's disease, and schizophrenia. In clarifying the brain in detail, we need both a wider field of view and high-resolution images. This makes the fact that most conventional microscopes can only produce a small-area image with high resolution a key limiting factor in current advanced brain research.

Although commercial WSI systems have been made available by various companies and might be used to collect high-resolution widefield microscope images, virtual slide systems have been mostly limited to brightfield and fluorescence imaging; they did not provide high-magnification darkfield imaging until 2009. Our collaborator Dr. Harvey Karten and pioneering brain mapping researcher Dr. Partha Mitra invited me to participate in the Mouse Brain Architecture Project at Cold Spring Harbor Laboratory in the autumn of 2009. Interestingly, Nobel laureate Dr. James D. Watson also was at the meeting. At that time, Dr. Karten discussed with me the importance of darkfield illumination to improve the sensitivity for detecting immune-histochemical stained samples. We came to believe that we needed to develop a new imaging method by combining darkfield imaging and WSI technology.

1.1.5   Microfluidics

Micro total analysis systems (μTASs) have become popular over the last two decades (Manz et al. (1990)). Microscale tools to control fluid flow, such as micro valves, pumps, and flow sensors have been developed (Gravesen et al. (1993)). Microfluidics technologies are now capable of manipulating nanoliters of fluid, molecules, bubbles, particles, and cells (Whitesides et al. (2006)), and these have been used for micro-fabrication in engineering settings as well as diagnosis in clinical settings (Sackmann et al. (2014)). Recently, techniques for producing microbubbles using microfluidic devices have been developed, and the two-phase flow in microchannels has been measured (Theberge et al. (2010); Choi et al. (2011); Garstecki et al. (2004, 2006); Epstein et al. (2007); Prakash et al. (2007), Teh et al. (2008); Zhang et al. (2013); Anna et al. (2003)). Some groups have succeeded in fabricating monodispersed microbubbles for drug delivery, and in clinical diagnosis, they have been used as contrast agents. Droplets and vesicles can also be fabricated by microfluidic devices, which can then be used in synthesizing molecules, such as proteins and DNA (Prakash et al. (2007)).

To design such microfluidic devices appropriately requires an accurate dynamic analysis of the motion of bubbles and droplets, with high resolution in time and space. In particular, interactions between bubbles and channel walls are important because microbubbles may block microchannels, which alters the flow compared to what was expected (i.e., clogging). Moreover, bubble shape is important in the breakup and coalescing of microbubbles in microfluidics. Thus, visualization techniques that enable detection of the surfaces of bubbles and walls are important (Anna et al. (2003); i Solvas et al. (2011); Link et al. (2004)).

In microfluidics research, the velocity field is often measured using microparticle image velocimetry (μPIV) (Adrian et al. (1991); Prasad et al. (1992); Santiago et al. (1998); Meinhart et al. (1999)). Recently, confocal laser scanning microscopes (CLSM) such as disk scanning confocal systems have been adapted to μPIV systems to improve image contrast and reduce the depth of field of the image (Park et al. (2004); Bourdon et al. (2006)). Three-dimensional (3D) optical sectioning has become possible and semi-3D velocity measurements have been performed (Kinoshita et al. (2007); Lima et al. (2006, 2007, 2008, 2009); Ishikawa et al. (2011); Leble et al. (2011)). To enable highly accurate velocity measurements, high-contrast images of tracer particles are required. Moreover, the wall

_____

configuration must be observed clearly to evaluate the wall shear stress, which can be calculated from the velocity gradient observed in the wall. Thus, it is necessary to simultaneously and clearly observe the wall configuration within channels and fluorescent tracer particles flowing through the channels.

Microfluidics technologies have also been used in cancer diagnosis. For example, an antibody-based microfluidics platform can capture cervical cancer cells using immunocytochemistry techniques (Du et al. (2006)). Oral squamous cell carcinoma (OSCC) cells were detected with a microfluidic device using magnetic beads conjugated with antibodies plus real-time polymerase chain reaction (RT-PCR) (Mauk et al. (2007)). Microfluidic devices have been used to identify circulating tumor cells (CTCs) in the peripheral blood of patients with metastatic lung, prostate, pancreatic, breast, colon, and ovarian cancers (Nagrath et al. (2007); Maheswaran et al. (2008); Song et al. (2009); Yung et al. (2009); Kim et al. (2010); Kirby et al. (2012); Das et al. (2013); Tanaka et al. (2012); Hou et al. (2009); Hung et al. (2011); Schleifman et al. (2014); Chen et al. (2014); Sorger (2008); Heath et al. (2008); Wlodkowic et al. (2010); Chakraborty (2013); Zhang et al. (2013)).

In the design of such microfluidic devices, it is important to observe the behavior of cells within channels with complex geometry. Moreover, cancer cell adhesion and invasion have been investigated using microfluidics to assess the mechanisms of cancer metastasis (Prabhakarpandian et al. (2008, 2011); Rosano et al. (2009); Tousi et al. (2010); Zervantonakis et al. (2012); Bersini et al. (2014)). As the interactions between cancer cells and vessel walls are important, visualization techniques to detect cancer cells and their relationships to channel walls are critical to understanding cell behavior (Anna et al. (2003); Solvas et al. (2011); Link et al. (2004)). Such techniques are investigated in this study.

The most common illumination systems used for cell and microfluidics observation in previous studies were brightfield, darkfield, fluorescence, and confocal imaging. Regular darkfield illumination is typically used for particle observations (Hu et al. (2008)). An example is its use in a blood cell counting application (Smith et al. (2014)). Fluorescence and confocal techniques are useful for observing specific cell markers.

The simultaneous detection of the channel wall and the cell marker is difficult. Lima combined transmitted halogen illumination and confocal imaging to increase the visibility of fluorescently labeled cells and walls (Lima et al. (2009)). However, observing widefield views of microfluidics and channel walls has remained technically difficult.

1.1.6 Total internal reflection fluorescence (TIRF) microscopy

Total Internal Reflection Fluorescence (TIRF) microscopy is an optical technique that is used to observed the surfaces of the cells for many years. The use of total internal reflection to illuminate the cell surface close to the interface between the glass and water was first described by Ambrose in 1956 (Ambrose (1956)). He explained using the illuminator for total reflection angle, and he set up the mercury light source to illuminate and received scattering from the sample. He explained how to observe the cell surface using totally reflected illumination.

This idea was then extended by Daniel Axelrod at the University of Michigan, Ann Arbor in the early 1980s as Total Internal Reflection Fluorescence Microscopy (TIRFM). He switched to mercury light source to Argon Laser to increase the illumination power. And, he explained using total internal illumination for excitation light for the fluorescent molecule. And he conjugated sample with fluorescence molecules. The cell surface image was clearly observed by fluorescence (Axelrod (1981, 1990)).

In the 1990s, the research method for single molecule imaging was becoming very popular. The Total Internal Reflection Fluorescence (TIRF) microscopy was a very nice tool to observe single molecules because the signal-to-ratio for the image was very high compared with regular fluorescence microscopy. Thus, scientists used TIRF microscopy to observe single molecules images from the surface of cells (Funatsu et al. (1995); Tokunaga et al. (1997); Steyer et al. (1997)).

In this thesis, we explain our study and development of Total Internal Reflection Fluorescence (TIRF) microscopy. Many investigators were using magnification 100×, NA 1.40 objective lens for observing the cellular and molecular event in living cells using TIRF microscopy in 1998. The TIRF microscopy had been gaining popularity among many biological applications. Especially, the objective lens type TIRF microscopy was a very useful tool for observing cells and single molecules using near-field fluorescence imaging. The objective type TIRF microscopy had more potential, and it could be combined with other imaging methods such as scanning probe microscopy or Differential Interference Contrast (DIC) microscopy.

Our original study was done on 1998-2000. At that time, the TIRF microscopy was difficult to handle due to the complexity of the microscope setup and the difficulty in achieving an acceptable image brightness. As far as I know there were no commercially available TIRF microscopy system at the time. Some scientists with a little experience in aligning optical systems tended to have difficulties, because the laser needs to pass through the very perimeter of the 100×NA 1.40 objective lens. Here, explains the technical points in detail. The critical angle for the 100×NA 1.40 objective lens with a water-immersed specimen (cells) is 65.63 degrees, and the maximum light pass angle is 67.53 degrees. The angle available for the total internal reflection illumination is only 1.9 degrees. It is a very narrow margin for setting. As a result, it is very difficult to align the laser beam into the margin of this NA 1.40 objective lens, which makes the evanescent wave illumination failed most of the times (see Fig. 2-15).

One of the issues of TIRFM was a requirement of using a prism. The sample always stayed between the prism and the cover glass. Some group uses the longer working distance and the lower numerical aperture objectives observing TIRF image. Collected image was dimmer and hard to observe the image. It was hard to reach the samples because the evanescent field located top side of the sample (see Fig. 2-14). Toshio Yanagida in Osaka University and another group was developed the objective type TIRFM (Tokunaga et al. (1997)). This design provided the open space above the sample. It places the atomic force microscope (AFM) above the sample. Then the objective type TIRFM system could be provided the dual observation (TIRFM and AFM). The sophisticated system was exploited by biophysicists for single molecule imaging (Tokunaga et al. (1997); Steyer et al. (1997)). At the almost same time, Dr. Terakawa was interested in observing the high resolution image. He made a custom made objective lens 100X, NA 1.65 objective lens with Olympus (Terakawa et al. (1997, 1998, and 2001).

The TIRFM method was rapidly spreading in the cell biology field and the neuroscience field. Many scientists use TIRF microscopy for observing physiological phenomenon from the cell

_____

membranes (Loerke et al. (2000); Schmoranzer et al. (2000); Sonnleitner et al. (2002); Ohara-Imaizumi et al. (2002); Oheim et al. (2002, 2005); Schapper et al. (2003); Jaiswal et al. (2003, 2007); van't Hoff (2008); Fish (2009)). Development of membrane specific dyes and green fluorescent protein (GFP) had accelerated this spread (Haugland et al. (1996).

When I was in New York, I helped setup the TIRF microscope in Dr. Sanford M. Simon's lab (Schmoranzer et al. (2000). They observed very clear and dynamic exocytosis image using TIRF microscopy.

Then, here we explain the recent studies for DIRI combine with TIRF microscopy observing for samples. Many scientists use fluorescent dye stained samples for observing the dynamic or static event for the biological materials. In most of the cases, the sample is not stained with visible dyes. Thus, it is not easy to find the samples using brightfield microscopy.

For example, in some cases, scientists use microfluidics for samples. In this case, it is hard to observe the channel side wall for microfluidics with using brightfield illumination or fluorescence illumination. For example, if the sample such as cells are in the microfluidics it is very important to find channel side wall. We try to solve this problem using DIRI.

1.1.7   Robotic microscopes and internet of things (IoT)

Technological advances have led to the creation of robotic microscopes. In addition, image-stitching technologies, cost-effective data storage systems and local- and wide-area networks (LAN and WAN) are now widely available. Pathology is one area that has compelling application and utility for WSI and image servers (Leong et al. (2001); Costello et al. (2003); Blake et al. (2003)). In the fields of research pathology, education and nonclinical environments, widefield microscope images today often are acquired using whole-slide or virtual-slide-scanning microscopes (Weinstein et al. (2009), Pantanowitz et al. (2011); Yagi et al. (2005); Long et al. (2013)). Thus, in the microscopy environment, image sharing is becoming an integral part of the workflow.

The Internet of Things (IoT) is a scenario in which objects, animals, and people are provided with unique identifiers and the ability to transfer data over a network with or without requiring human-to-human or human-to-computer interaction. Dr. John Barrett, Cork Institute of Technology (CIT), explained that the web browser was introduced in 1993. Since then, interest has grown for connecting everything from sensors and cameras to automated machines, pets, humans, etc. People are keen to learn as much as possible from so-called big data using computers. This is not only true in industry; biological research and medical fields also are part of the big data phenomenon. One vision of the future of science includes incorporating image data in such explorations to help advance science. To accomplish this, both robotics and IoT capability with a microscope are needed, both for information collection and image analysis.

_____

1.2   Purpose of the study

Development of darkfield internal reflection illumination (DIRI) system and total internal reflection fluorescence (TIRF) microscopy

As explained in chapter 1.1, current brain and microfluidics research applications need new methodologies for observing sample structure. One important issue is how to observe wide-sized samples, such as whole-glass-slide or whole-microfluidics samples, with high resolution. In this study, we set out to solve this issue, utilizing WSI technology and a motorized TIRF microscope as our basis.

In order to collect as much sample information as possible, imaging technique is highly important. Thus, the core of our research and development was about how to implement a new imaging method to expand the capability of the automated multi-modality microscope.

Our first aim was thus developing DIRI, and then combining DIRI with WSI and TIRF microscopy. Darkfield microscopy is a traditional imaging method, with great utility in providing the ability to observe unstained samples. However, attaching automated microscopes to traditional darkfield is not easy and has some limitations. Using such a system with oil-immersion objectives, for example, always requires the immersion oil on the darkfield condenser. Traditional darkfield units can be hard to maintain.

To overcome this issue, we developed DIRI, setting out to make it easily adaptable to WSI and motorized TIRF microscopy so that it could serve as a practical alternative for use with automated microscopes.

We developed the darkfield internal reflection illuminator using thin-array LEDs. This method has advantages in comparison to conventional methods such as using a regular optical microscope with traditional darkfield microscopy. It provides more automation and more sample information from the images.

Up to now, TIRF microscopy has had a number of issues: (a) Technically the setup is tough, and (b) TIRF microscopy only provides images from a very narrow-depth evanescent field, so sample information is very much limited.

The TIRF microscope we developed, combined with DIRI, can overcome these issues. The advantages of combining TIRF and DIRI include the benefit of eliciting far more sample structure information from captured images.

Applications for brain research

Our second aim was to utilize the developed system to observe tissue slides such as brain tissue or TMA (tissue micro array) specimens. The WSI method sometimes allowed us to image using fewer stains with brain samples. For instance, diaminobenzidine (DAB) and fluorescent staining are helpful tools for observing protein localization and volume in tissues. However, these methods usually require counterstaining in order to visualize tissue

_____

structure, limiting the accuracy of the localization of labeled cells within the complex multiple regions of typical neurohistological preparations. The DIRI technique is a label-free method of producing contrast in a sample. Thus, adapting DIRI imaging to WSI may be useful, particularly when researchers require additional structural information without the use of further staining.

Overcoming this problem, we adopted the DIRI system for WSI for use in wide-area, high-resolution imaging of brain slices. We sought information on DIRI's usefulness for observing brain slice structure without using counterstaining. The WSI system is also capable of observing fluorescence and DAB images. Fluorescence and DAB imaging produce functional information such as the location of proteins or specific neurons. We sought the ability to glean both structural and functional information.

Applications to microfluidics researches

As previously mentioned, microfluidics is used increasingly for engineering and biomedical applications due to recent advances in microfabrication technologies. Visualization of bubbles, tracer particles, and cells in a microfluidic device is important for designing a device and analyzing results. However, with conventional methods, it is hard to observe both channel geometry and such particles simultaneously.

Microfluidic devices with multiple reactor areas and/or multiple measurement sites are often larger than the field of view of a typical microscope objective lens. Thus, WSI is useful for observing the entirety of these areas. WSI technology is well suited for observing areas larger than one field of view under a microscope and is used for tile imaging, remote viewing, archiving, and analyzing images for neuroscience and pathology. As far as I know, currently there is no WSI system that automatically observes the entire field of fluorescence or brightfield image as well as a darkfield image using both dry and oil objective lenses.

In order to overcome this problem, we adopted the DIRI system for WSI of microfluidics. The proposed methodology should be useful in the future for controlling microfluidics by monitoring multiple locations.

_____

1.3 Structure of the thesis

This thesis consists of 4 chapters. Chapter 1 is the introduction of the thesis. We review historical background and former studies in the fields of optical microscopy, whole slide imaging, brain mapping, microfluidics, TIRF microscopy, robotics microscopes and the Internet of Things. Then, we explain the aims of the study and the thesis structure.

Chapter 2 explains the materials and methods used in: (1) the development of DIRI for brain research applications, (2) the development of DIRI for microfluidics applications, and (3) the development of a combined DIRI and TIRF microscopy system. The brain application section explains methodologies using DAB-stained and fluorescent fixed-brain-tissue samples with DIRI. We also used selected non-brain TMA samples for evaluating the DIRI system. The microfluidics application section explains methodologies using the micro-blood vessel to evaluate static imaging and dynamic flow imaging using DIRI. The TIRF application section explains methodologies using fluorescent beads and fluorescent dye-stained cells to check TIRF performance. It also explains methodologies using floated fluorescent beads with micro blood vessels to evaluate static imaging using TIRF and DIRI.

Chapter 3 explains the experimental results. Section 3.1 shows that the newly developed DIRI system, applied it to brain application, has several key benefits over traditional darkfield: (1) No oil condenser is required for high-resolution imaging, (2) There is less scatter from dust and dirt on the slide specimen, (3) There is less halo, providing a more natural darkfield contrast image, (4) The motorized system produces darkfield, brightfield and fluorescence images and (5) there is color control capability, providing a natural-color DIRI image. These results indicate that DIRI is useful for brain side sample imaging.

Section 3.2 shows how DIRI was applied to microfluidics applications. We found the WSI, combined with DIRI, extended the capabilities of the system to allow multi-modal imaging. Multi-modal imaging allowed clear visualization of both microbubbles and channel walls by utilizing DIRI and fluorescence or brightfield illumination simultaneously. The imaging methodology is useful not only for examination of static phenomena, but also for observation of dynamic phenomena, such as the detection of bubbles, fluorescent tracer particles or labeled cells flowing through a channel. Observation of these dynamics makes possible a whole range of physical and physiological measurements of systems used for modeling more complex in vivo situations. These results indicate DIRI is useful for microfluidics applications.

Section 3.3 shows how DIRI was applied to TIRF microscopy. Here, we introduce the solution for an easy-setup TIRF illuminator. Then, we compare the regular fluorescence image, image captured using a 60x, NA1.45 objective lens, and an image captured using a 100x, NA1.65 objective lens. The 100x, NA1.65 objective is five times brighter than 100x, NA1.40 lens. Also, the setup time was reduced dramatically compared with the optical bench TIRF system. I then explain the experimental conditions for combining DIRI and TIRFM. DIRI microscopy helps to observe the edge of microfluidics. The results indicate that DIRI, combine with TIRF microscopy, is useful for microfluidics applications.

In chapter 4, we present the overall conclusions of my research. This section explains the usefulness of WSI with DIRI and TIRF with DIRI. Comparing darkfield systems, DIRI is easier to use than a traditional darkfield condenser. DIRI proves to be a very useful observation method when used with the automated microscope.

_____

In the Appendix, we explain the basics of optical microscopy by referring to existing studies and books. If readers are not familiar with optical microscopy, this section will be helpful to understand the basics.

In the Research Accomplishments section, I have listed scientific papers related to DIRI. I also have included proceedings, posters, and other relevant scientific activities and presentations.

_____

Chapter 2   Materials and methods

In this chapter we explain the materials and methods employed in this study. Chapter 2.2 explains materials and methods in the development of DIRI for brain research applications. Chapter 2.3 explains materials and methods in the development of DIRI for microfluidics applications. Chapter 2.4 explains materials and methods in the development of DIRI combined with TIRF Microscopy.

_____

2.1 Development of DIRI for brain research applications

2.1.1   Darkfield microscopy

Brightfield imaging is the most commonly used light microscope illumination method. It uses transmitted light to illuminate a specimen. Light travels from one side of the specimen through the specimen to a detector on the other side. As a result, the specimen is displayed on a bright background.

In the case of a darkfield microscopy, illumination light enters the specimen at an oblique angle and the illumination light is blocked from the detector. Therefore, a darkfield image background is dark, and the specimen appears bright against the background. If there is a mismatch between the refractive index of the specimen and the mounting media light will scatter or refract. This darkfield illumination method provides enhanced detection sensitivity and contrast for specimens that are not imaged well using brightfield illumination (Pluta (1989); Abramowitz (1987, 1990); Hecht (2002); Murphy (2001); Bass (1995)). Using darkfield imaging, researchers in a wide variety of fields have detected very small refractive-index mismatches to elucidate specimen structural and surface attributes in detail (Dong et al. (2001); Miyawaki et al. (1996)).

A darkfield microscope can detect very small samples. Hotani et al. (1988) reported they observed dynamics of microtubules visualized by darkfield microscopy. Probably their detectable sample diameters were smaller than 40 nanometers, or one-fifth the 220-nanometer resolution limit with oil immersion of the 1.4 NA objective. In biological applications, the movements of living bacterial flagella that average about 20 nanometers in diameter can be observed. This sample size is too small to be seen in brightfield or DIC illumination.

There are several types of darkfield illumination available. Transmitted darkfield is widely used for biological specimen observation. Typically, a transmitted darkfield illuminator uses a halogen bulb with either a dedicated substage darkfield condenser or a darkfield central stop in a standard brightfield condenser. Central axial illumination is blocked by the darkfield central stop and the peripheral illumination obliquely illuminates the specimen from below. Thus, only forward-scattered or refracted light from the specimen enters the objective lens. This light creates the darkfield images (Pluta (1989); Abramowitz (1987, 1990)). Fig. 2-1 is a schematic of the darkfield illuminator using transmitted light path.
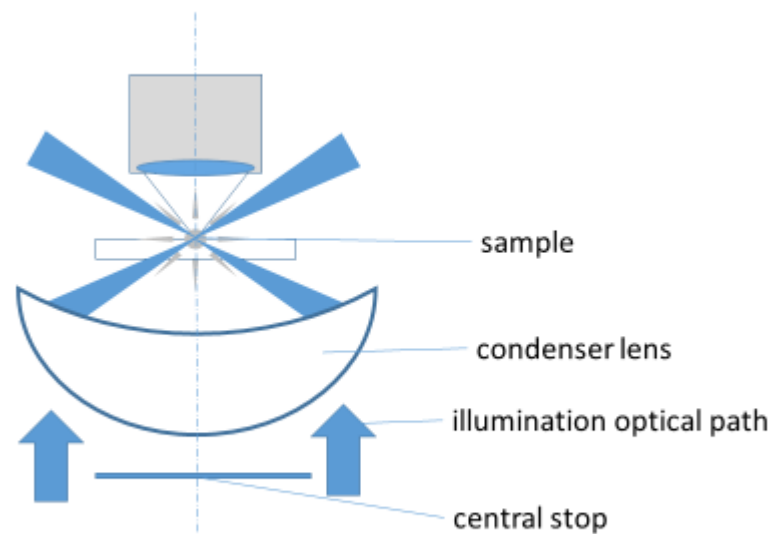
Fig. 2-1   Darkfield illumination using transmitted light path

The second type is reflected darkfield illumination. This method is commonly used to visualize metallurgical specimens and is not commonly used for biological specimens. Reflected darkfield illumination employs a vertical illuminator mounted above the objective lens. Only peripheral rays of light from the illuminator reach the deflecting mirror above the objective lens. The peripheral rays are deflected downward and around the periphery of a specially modified darkfield objective lens with a circum-objective condenser in the form of a doughnut. Only backward-scattered or reflected light from the specimen enters the objective lens, creating the darkfield image (Pluta (1989); Abramowitz (1987, 1990)). This method is of limited value with typical histological slides, as the light reflects off the coverslip. Fig. 2-2 is a schematic of the reflected darkfield illuminator using the incident light path.
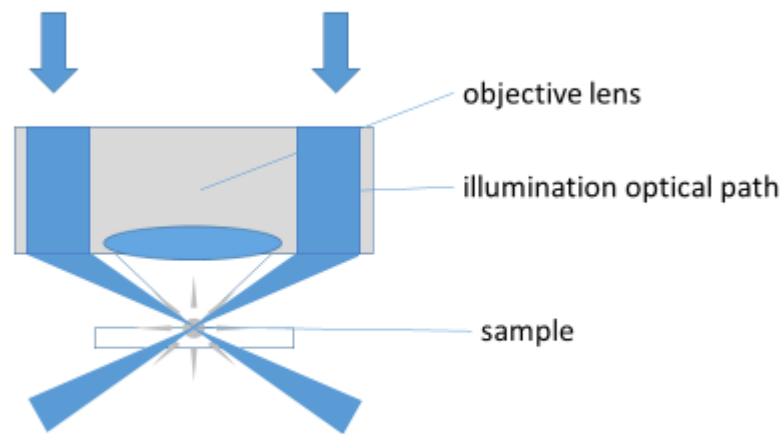
Fig. 2-2 Reflected darkfield illumination using the incident light path

The third type of darkfield illumination is side-illuminated darkfield. This method eliminates light sources from both top and bottom. A fiber-optic bundle is mounted horizontally on the edge of the specimen slide, so that light strikes the specimen from the side. A typical setup uses a fiber bundle with a halogen light bulb to illuminate the sample from the side. Only side-scattered or reflected light from the specimen enters the objective lens. The surrounding regions of the microscopic field present as a darkfield image (Pluta (1989); Abramowitz (1987)). This configuration is sometimes called a Hausmann's darkfield illuminator and is employed, for instance, in the commercially available Darklite Illuminator (Micro Video Instruments, Inc. Avon, MA).

2.1.2 Theory of darkfield internal reflection imaging (DIRI)

We used a Hausmann's darkfield illuminator for our basic design. However, due to the constraints imposed by the use of a motorized stage with illuminator, the fiber bundle is rigid and can impede stage movement. We therefore chose LED illumination in place of the more-often-used rigid fiber bundle with halogen light illumination.

The LED is directly connected to the side of the slide glass. Only side-scattered or reflected light from the specimen enters the objective lens. The surrounding regions of the

microscopic field present as a darkfield image. We refer to this as darkfield internal reflection imaging (DIRI).
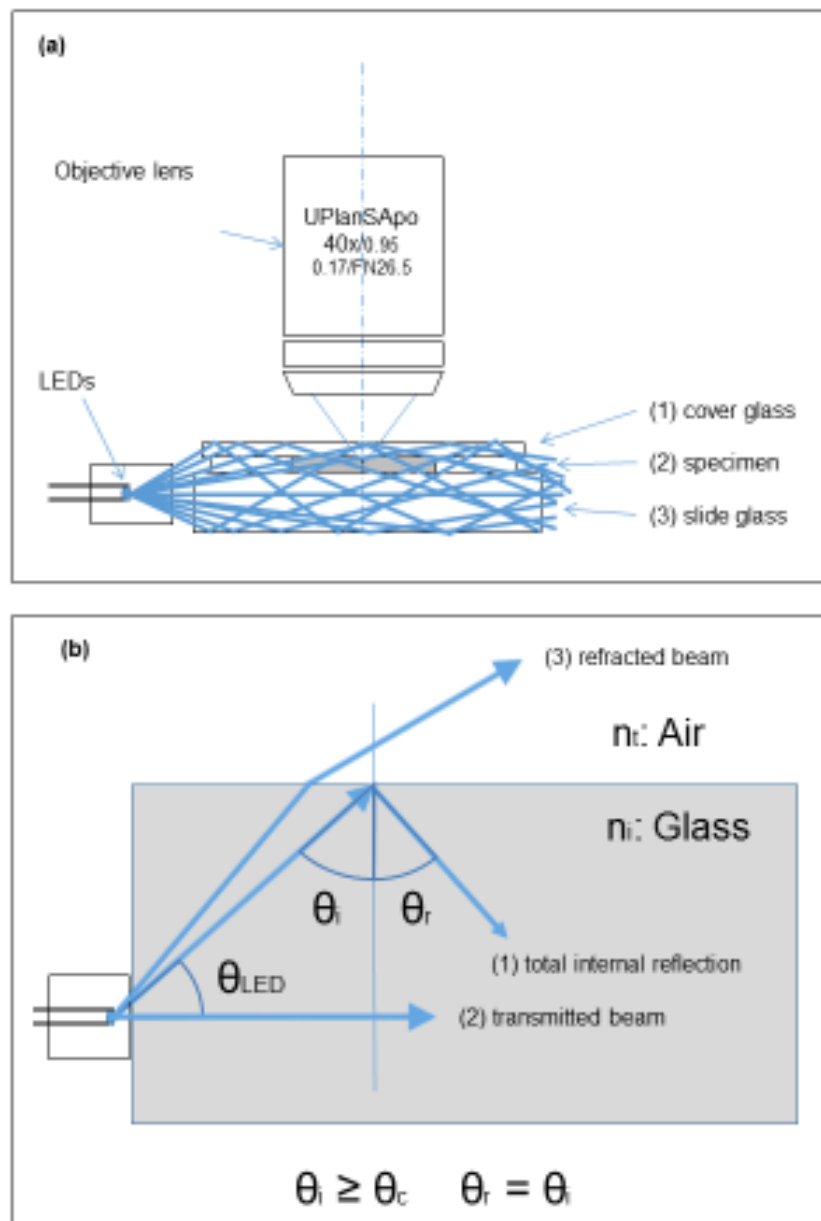
Fig. 2-3 Mechanism of darkfield internal reflection illumination.
(Kawano et al. (2013)).

(2-3a) Light hits the surface where air (n_t) meets glass (n_i). If light enters the surface, θ_i is more than the critical angle necessary to cause reflection from the surface.

(2-3b) Light path within the sample when the angle of light is greater than the critical angle.

_____

Before explaining darkfield microscopy imaging methods, it is important to discuss microscope slide glass and how specimen slides are assembled. A typical WSI specimen slide consists of three parts: a slide glass, the cells or tissue together with their mounting media, and a cover glass. The cells or tissue and mounting media are slightly different refractive indexes. We observe this slide sample using a microscope.

Snell's Law, a formula describing how light travels through a boundary between two media with different refractive indices, helps elucidate the mechanism for the DIRI system. Typically, the refractive index ni of the cover glass, tissue or cells with mounting media and glass slide is 1.4 to 1.5. In contrast to this, the refractive index for air nt is 1. Internal reflection (Fig. 2-3a) occurs when $n_i > n_t$ and the incident beam angle θ_i is equal to or greater than θc, the so-called critical angle (Hecht (2002)). If the incident beam angle is greater than the critical angle, light reflects off of the surface between n_t and n_i (Fig. 2-3b).

$$sin\ \theta_i = \left(\frac{n_t}{n_i}\right) sin\ \theta_t \qquad\qquad (2.1)$$

To find the critical angle if θ_t is 90 degrees, then sin θ_t is 1.

$$\theta_c = sin^{-1}\left(\frac{n_t}{n_i}\right) \qquad\qquad (2.2)$$

2.1.3   Experimental setup and procedures in section 3.1

a. DIRI using white LEDs

We used the VS120 WSI scanning system (Olympus America Inc., Center Valley, PA), which was configured for acquiring and storing widefield microscopic images (Fig. 2-4a). The WSI system setup included a microscope imaging system with a camera, objective lens, motorized focus system and motorized X-Y stage. The system was equipped with a standard substage darkfield condenser, a transmitted brightfield illuminator, a fluorescence illuminator and the DIRI system described herein (Fig. 2-4b). This configuration allowed the fully automated acquisition of multiple specimen images utilizing all four illuminators.

The operator used software to configure the acquisition parameters, selecting the magnification (objective lens) and observation method (e.g. transmitted brightfield, fluorescence or darkfield); the system used the input to set the stage and focus positions and acquire images automatically.
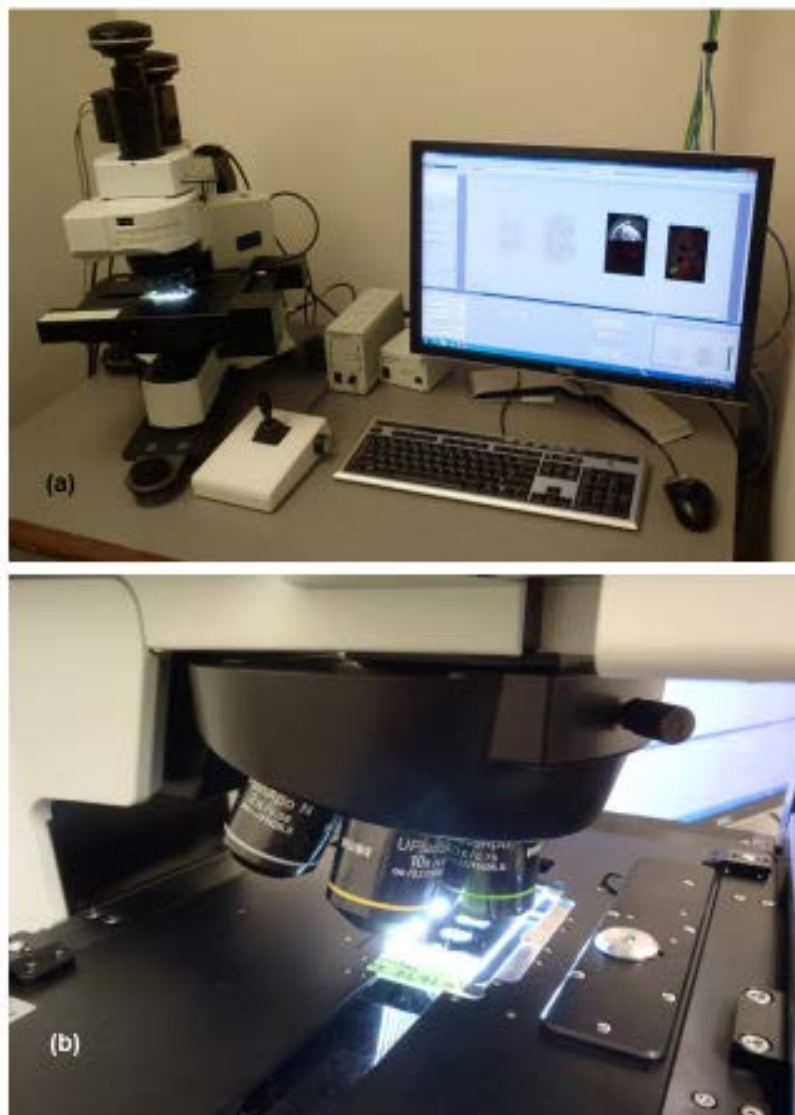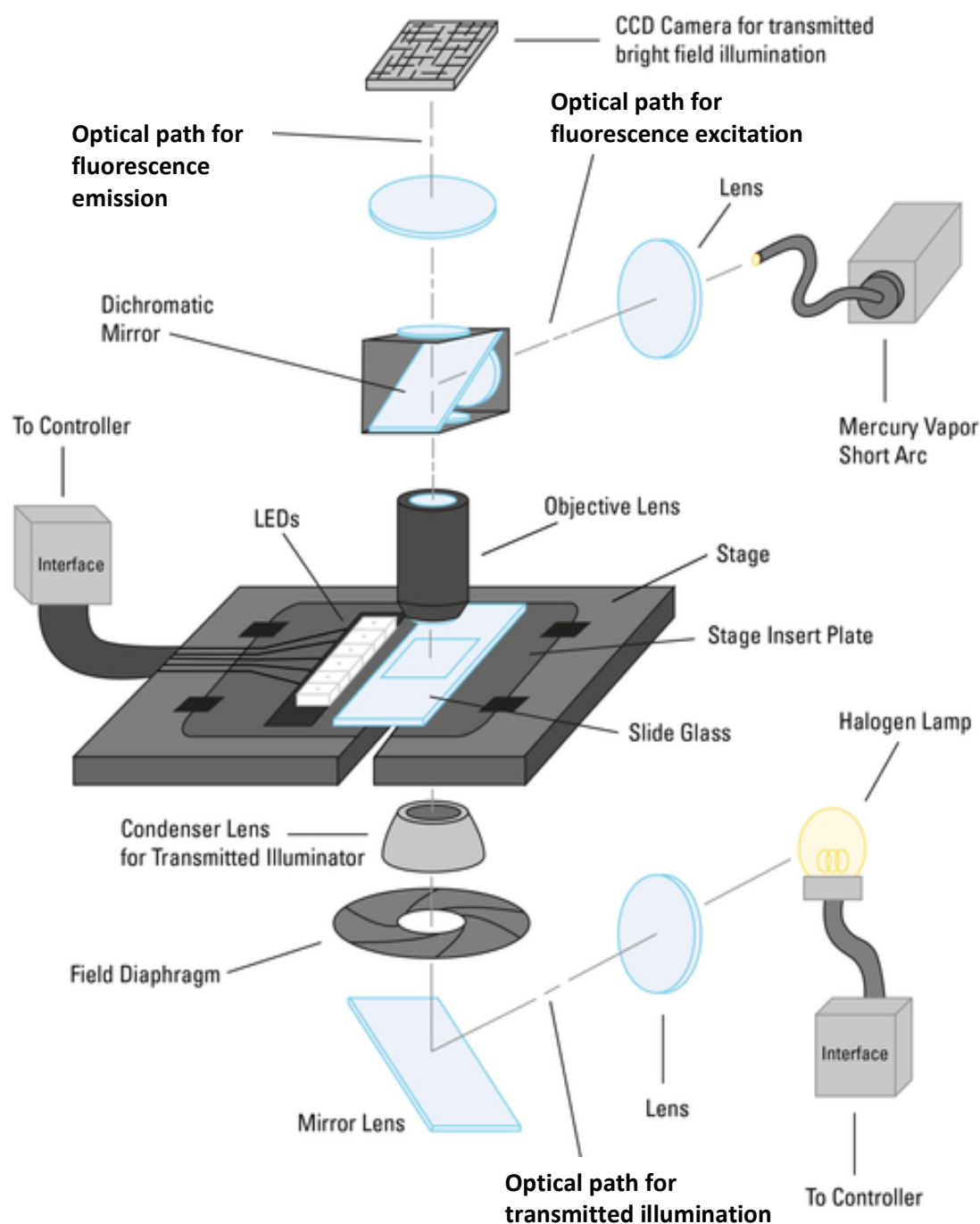
Fig. 2-4. WSI system setup. (Kawano et al. (2013)).

(2-4a) The whole-slide imaging (WSI) system is configured on a microscope with motorized Z-axis focus capability, a motorized X-Y stage, the darkfield illuminator with stage insert plate, a mercury light bulb for fluorescence illumination (not visible here), a transmitted illuminator for the halogen light bulb (not visible here), and an XC10 CCD color camera (front camera) and XM10 CCD camera (back camera) to acquire transmitted brightfield and darkfield images. The WSI system is controlled by VS-ASW v2.5 software.

(2-4b) Light scatter from a brain slice specimen. A brain slice is mounted on a 1×3-inch microscope glass slide and placed on the stage. A stage insert plate with multiple white LEDs is mounted on the stage. The white LEDs illuminate the entire microscope slide. The brain and mounting media have refractive index mismatches that cause the specimen to scatter light.

_____

Prior to collecting high-resolution WSI images, we captured macro images at 2×
magnification in transmitted brightfield or fluorescence mode. These low-resolution images
provided an overview of the specimen for later navigation and high-resolution image capture.
The macro image function enabled easier setup in particular regions of interest.

Our darkfield illuminator utilized an LED light source (Fig. 2-6a and b). This is the first
generation prototype DIRI LED illuminator. To provide enough light intensity we configured
multiple white LEDs into a stage insert plate in a horizontal array (Fig. 2-6c) that illuminated
the specimen from many different angles simultaneously. The LED selected was a
commercially available unit, the CL-435F (Citizen Electronics Co., Japan). This ultra-thin
LED, originally designed to be incorporated into a mobile phone's back panel illuminator, is
just 0.4 mm thick.

Fig. 2-5. Schematic drawing of an experimental WSI system with DIRI, using white LEDs. (Kawano et al. (2013)).

DIRI is incorporated into the WSI system's motorized stage. White LEDs illuminate the slide glass from the side, and the specimen scatters the illumination light. The scattered light is then collected by the objective lens above the stage. The dichromatic mirror on the motorized turret can be removed from the optical path when acquiring darkfield images. Above the dichromatic mirror is a tube lens that focuses the specimen image on the imaging device; a CCD camera captures the image.

_____
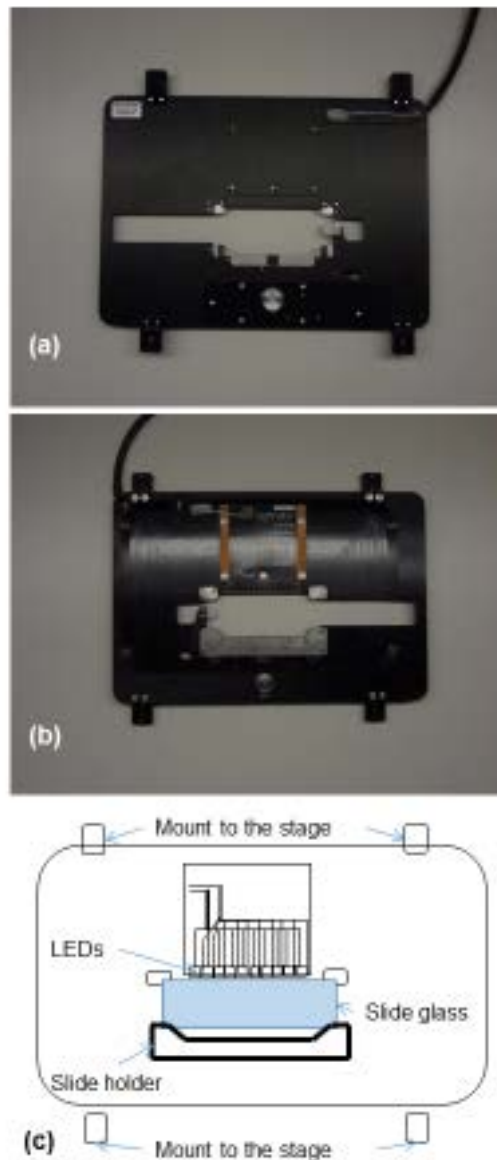
Fig. 2-6. WSI with darkfield illuminator. (Kawano et al. (2013)).

(2-6a) Top view of the stage insert plate used with the darkfield illuminator. The plate has four black extension tabs that mount to the stage using screws. The microscope slide glass can be placed at the center of the stage insert plate. The round silver part is used to fasten the 1×3-inch microscope slide to the plate.

(2-6b) Reverse view of the stage insert plate. The microscope slide glass is placed at the center. The LEDs are mounted on this side of the stage and illuminate this side of the slide glass.

_____

(2-6c) Schematic drawing of the WSI system with the darkfield illuminator.
The 1×3-inch microscope slide glass is placed at the center of the stage
insert plate. The four tabs are used to affix the plate to the stage.

The LEDs were equipped with clear plastic molded covers that provided a light guide function; the light sources illuminated specimen slides from edge to edge. The user could switch the illumination on and off via software during image acquisition.

According to the LED manufacturer, each LED's maximum luminous intensity is 1380 mcd. The LED light's angular distribution of 50% of the light intensity is plus/minus approximately 60-degree angulation. This means θ LED is about 60 degrees (see Fig. 2-3b).

A light intensity control was added to the system, allowing the operator to control the light intensity and to vary exposure times. We used an Illuminance Meter T-1 (Minolta Camera Co., Ltd., Japan) to measure light intensity with the light detector 3 mm from the LED array. The illuminator's measurement result of maximum intensity is 3740 lux.

The slide glass and cover glass refractive indices are each about 1.5. Using this number, we calculated that the critical angle θ_c at 41.8 degrees. Transferring the critical angle θ_c 41.8 degrees to the LED illumination angle, the required LED illumination angle θ LED is less than 48.2 degrees. Thus, the LED illumination beam angle θ LED required to produce DIRI illumination is less than 48.2 degrees (see Fig. 2-3b (1)).

Most of the LED illumination light beam θ_i is greater than the critical angle θ_c. These beams strike the surface where the glass meets air. This light beam reflects multiple times between the top glass surface and bottom glass surface, illuminating the entire specimen (Fig. 2-3A). For LED illumination at the angle around zero degrees, the light beam goes through the slide glass and illuminates the specimen directly (see Fig. 2-3b (2)). DIRI uses both of these mechanisms to illuminate the specimen. The LED illumination angle θ LED more than 48.2 degrees is not used for DIRI because the illumination light is transmitted to the surface between air and glass (see Fig. 2-3b (3)).

One unique feature of this experimental system was the ease with which we were able to acquire high-resolution images of the specimen using fluorescence, transmitted brightfield and darkfield at the same specimen location. To scan using brightfield, darkfield or fluorescence, the user selected a Scan button in the software, chose the type of scan, and then the system adjusted all settings automatically, including applying the appropriate dedicated background correction in real-time during acquisition. The user could press the Scan button again to collect additional scans using the other observation methods. The system also provided seamless stitching of whole slide images for the collection of data that extended beyond any single field of view.

Section 3.1 presents experimental results of the white-LED DIRI studies.

b. DIRI using color LEDs

DIRI was also explored using three-color LEDs. In all experiments, the base system comprised the Virtual Slide System VS120 (Olympus) and the VS-ASW WSI software (ver. 2.8) (Fig. 2-7). The WSI system setup includes a microscope imaging system with cameras, an objective lens, a motorized focus system, and a motorized X-Y stage. Two cameras were used: a black and white camera (Orca R2, Hamamatsu Photonics, Hamamatsu, Japan) and a color camera (XC10, CCD (Olympus Soft Imaging Solutions, Münster, Germany). The

_____

system contained a standard substage condenser, a transmitted brightfield illuminator, a fluorescence illuminator, and the DIRI system described herein (Fig. 2-8). This configuration allowed fully automated acquisition of multiple specimen images using all four illuminators. The acquisition parameters were configured using software to select the magnification (objective lens) and observation method (*e.g.* transmitted brightfield, fluorescence or DIRI); the software controlled the positioning of the stage and focus, such that images could be taken automatically.
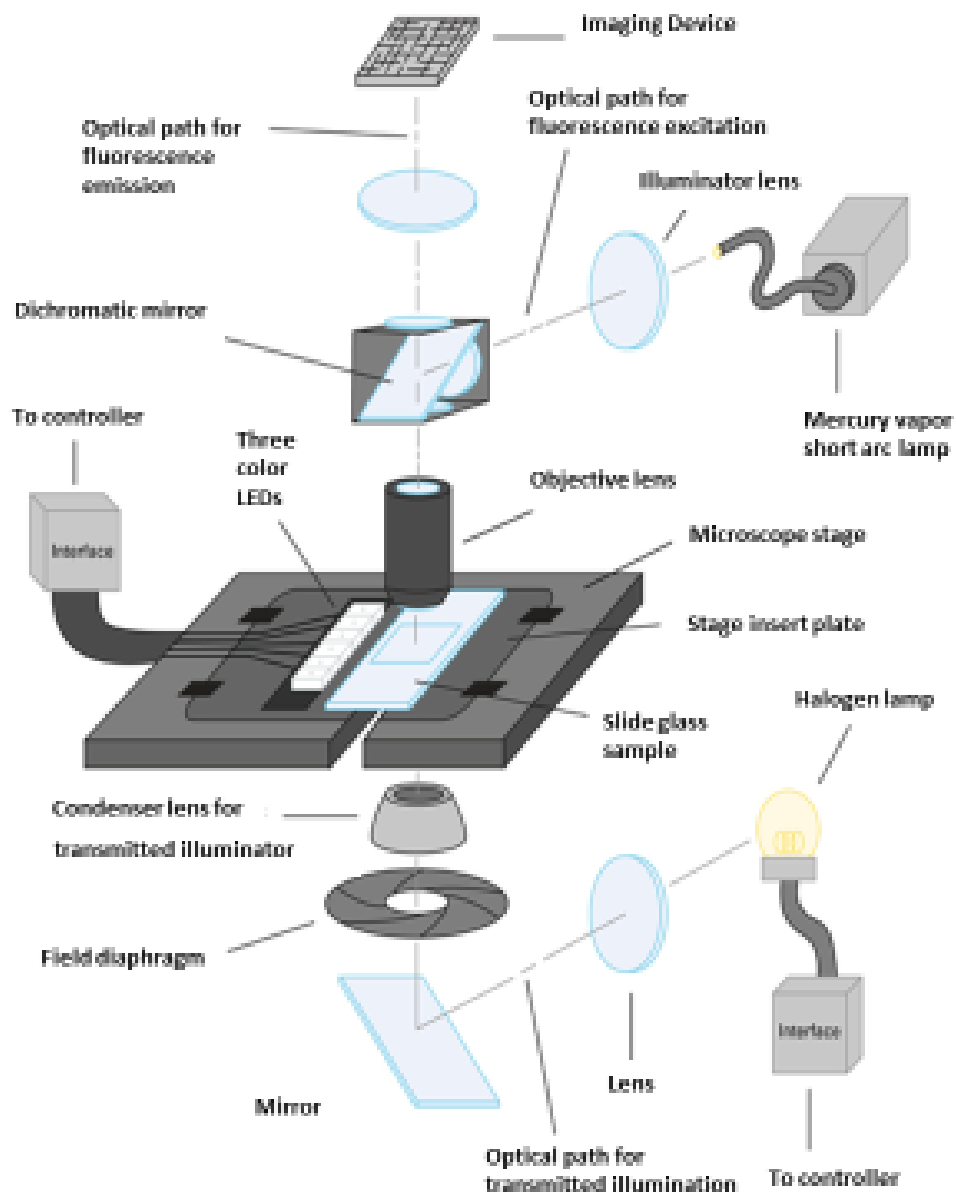
Fig. 2-7   Schematic drawing of the Three-Color LED WSI system with DIRI.

_____

DIRI is incorporated into the WSI system's motorized stage. Three-color
LEDs illuminate the slide glass from the side, and the specimen scatters the
illumination light. We removed white LEDs and attached three-color LEDs.

The previous version (third generation) of DIRI illumination (Fig. 2-5) used a thin array of
LEDs. These LEDs were preinstalled in the stage insert plate located on the microscope
stage (Fig. 2-6, and 2-8 (a1, a2)). The stage insert plate was configured with multiple LEDs
to ensure sufficient light intensity. The configuration used to be a horizontal array that
illuminated the specimen from many different angles simultaneously. The installed LED was
the commercially available CL-435F (Citizen Electronics Co., Yamanashi, Japan).

The present version of DIRI illumination uses a three-color LED array (Fig. 2-8 (b1, b2)). The
LED array is a commercially available unit (NeoPixel Stick – ID 14268, Adafruit, New York,
USA). This LED array uses eight sets of three-color (red, blue, and green) LEDs (World
Semi WS2812 5050 RGB). The WS2812 datasheet shows that the red, green, and blue
LEDs emit light over the wavelength range of 620–630 nm (550–700 mcd), 515–530 nm
(1100–1400 mcd), and 465–475 nm (200–400 mcd), respectively. Each LED is addressable
by the driver chip inside the LED. Each individual LED is controlled by an Arduino UNO
(Arduino, Turin, Italy) microcontroller.

We attached LEDs of three different colors to the DIRI illuminator for WSI. Before use, the
WSI system was calibrated using the VS-ASW software and the recommended calibration
slide from the manufacturer. The VS120 with the three-color DIRI system described here is a
prototype and is not commercially available.

(a1)

(a2)

(b1)

(b2)

8 sets of three LEDs

Cover glass

Microscope slide glass

(c)
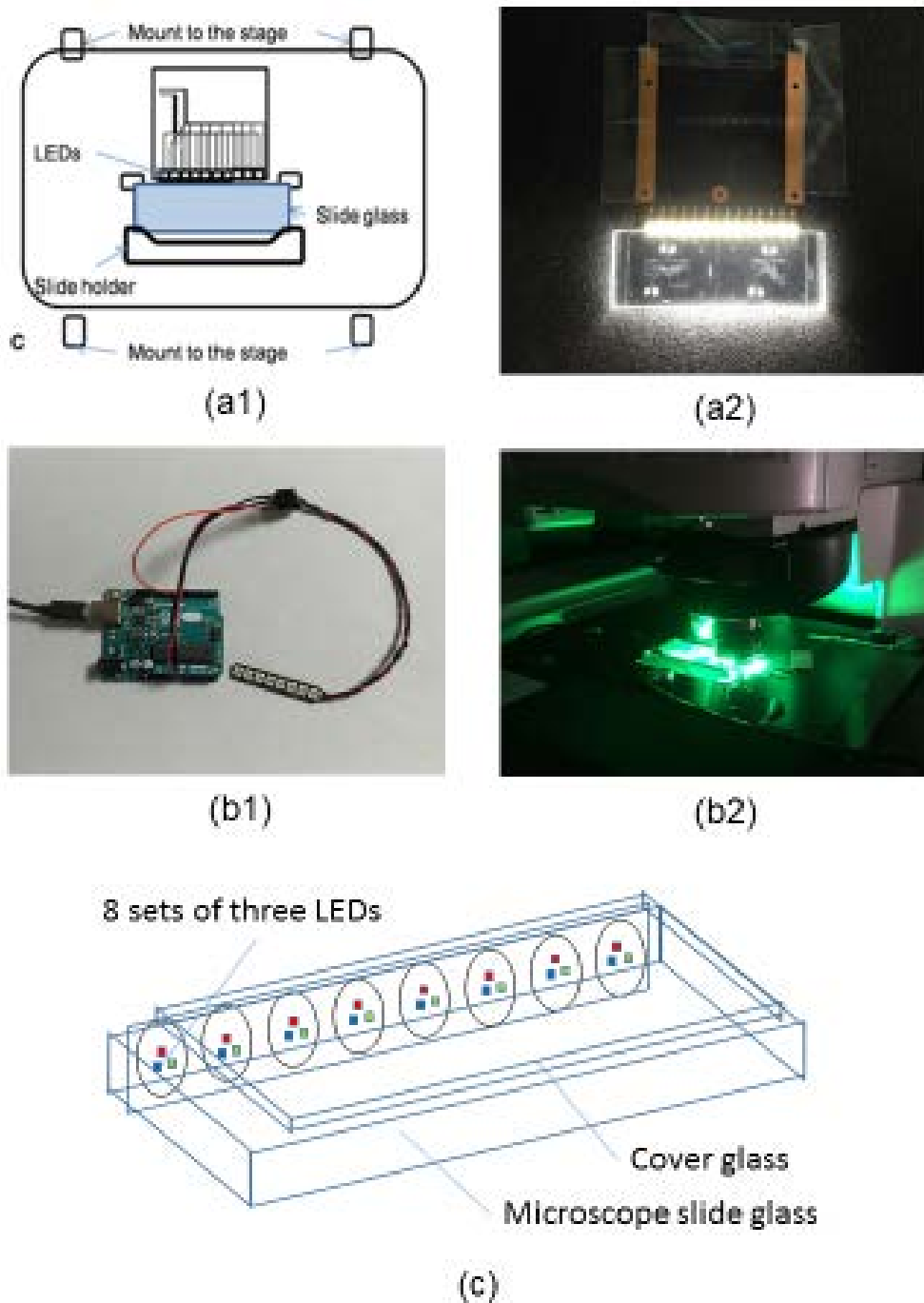
Fig. 2-8   DIRI for the thin white LED array and the three-LED array.
(a1) Schematic drawing of the thin white LED array from Fig. 2-6 (c).
(a2) the white LED array and a sample (microfluidics) from Fig. 2-10 (a).
(b1) the three-color LED array and controller.
(b2) the three-color LED array and a sample illuminated with green light
and (c) a schematic diagram of the three-color LEDs and a slide glass
sample.

A schematic diagram of the optical layout is shown in Fig. 2-8 (c). The DIRI system consists of LEDs attached to the microscope stage. The refractive light mismatch induced by this setup enables detailed imaging. The DIRI system can be used with widefield fluorescence. The halogen lamp is used for transmitting illumination. Mercury vapor short-arc lamps are used for epi-fluorescence illumination. The observed images are recorded with a CCD camera (Orca R2; Hamamatsu Photonics).
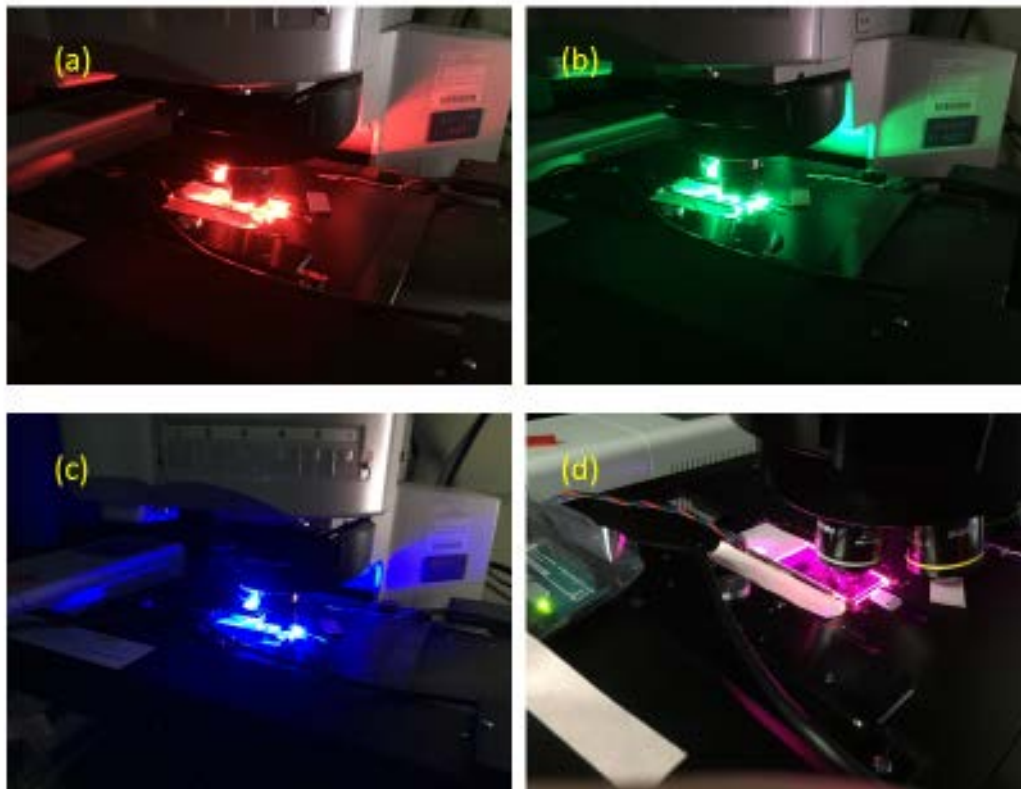
Fig. 2-9 DIRI color illumination.

A sample is illuminated by (a) red, (b) green, (c) blue, and (d) magenta light.

2.1.4   Sample preparation for section 3.1

For this study, the sample selected was an 11-core tissue microarray (TMA) (BSB0297, BioSB, Santa Barbara, CA). The TMA consisted of 2mm cores of formalin-fixed paraffin-embedded tissue. The array configuration allowed validation of reagents for immunohistochemistry applications. The 11-core TMA contained the following tissues: placenta, colon, prostate, skin, thyroid, liver, brain, kidney, tonsil, breast, and fallopian tube. We stained samples using p40 for a brown color (DAB) and TTF-1 for magenta via a Polydetector Detection System staining kit (BioSB, Goleta, CA, USA).

_____

Additionally, we used wild mice (C57BL/6J, 12 weeks old) and yellow fluorescence protein (YFP-H) mice (23 weeks old). The YFP-H mouse line was provided by Drs. J. R. Sanes and J. W. Lichtman. The YFP-H mouse lines were maintained by crossing with C57BL/6J mice for several generations.

All mouse experiments were conducted in accordance with Regulations for Animal Experiments of RIKEN. Our experimental protocols were approved by the Animal Experiments Committee of the RIKEN Wako Institute.

Mice were anesthetized with pentobarbital (Nembutal) and transcardially perfused with ice-cold PBS containing 10 U/ml heparin followed by 4% PFA/PBS. The dissected brains were subjected to post-fixation in 4%PFA/PBS at 4°C overnight and embedded in OCT compound.

A YFP-H mouse brain was cut into 50-µm-thick sagittal sections using a cryostat (Leica CM1860).

Prior to diaminobenzidine (DAB) staining, 30 µm-thick sections of WT mouse produced by the cryostat were treated with 3%H_2O_2 in MeOH for 30 min. The brain sections were permeabilized with 0.1%Triton X-100 in PBS for 5 min, and treated with 1% BSA in PBS for 30 min. The sections were incubated overnight at 4°C in PBS-T in primary antibody (anti-NeuN monoclonal antibody (Millipore #MAB377)), and then incubated in secondary antibody (HRP labeled anti-mouse IgG (MBL #PM009-7)) for 30 min at room temperature. Then, the sections were incubated in DAB substrate solution (Vector Laboratories, #SK-4100)) according to the protocol specified by the manufacturer.

Section 3.1 presents the experimental results of the three-color-LED DIRI studies.

_____

2.2 Development of DIRI for microfluidics applications

2.2.1 DIRI for observation of microfluidics using a microscope

I developed a second-generation prototype DIRI white-LED illuminator. The second generation DIRI white LED illuminator improved its brightness. We added it to a confocal system. Fig. 2-10a shows the developed DIRI unit. A multiple-LED light assembly was installed on the stage plate and used for side illumination of a microfluidics cell or a glass slide. The DIRI system was used alone, or with a fluorescence microscope. Acquired fluorescent images were used to show fluorescent markers of target objects. The DIRI system created a broad scattering of illumination from the edges of the PDMS channel walls. The refractive index mismatch between PDMS and the buffer (liquid) produced good image contrast, resulting in high-quality images of the microchannel walls. Superimposition of the two images (fluorescence and DIRI) allowed observation of both fluorescent markers and the edges of the channel walls. There were two ways to produce such superimposed images: (a) fluorescence and DIRI images acquired simultaneously, or (b) fluorescence and DIRI images acquired sequentially as two or more channels (depending on the number of fluorescent channels to be captured separately), with channels superimposed later. Method (a) can be applied to dynamic phenomena as well as static phenomena, whereas method (b) can be applied only to static phenomena.

_____
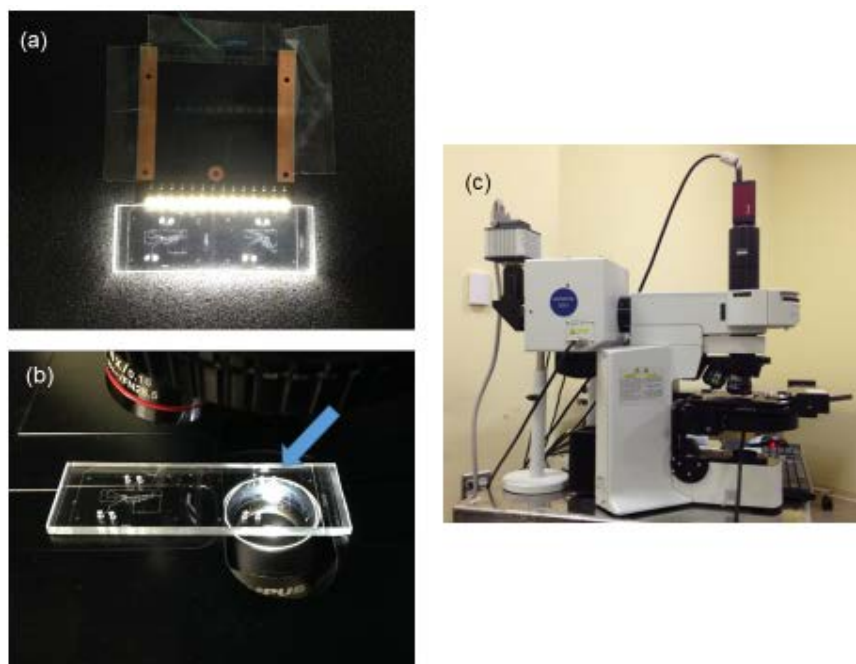
Fig 2-10. The darkfield illuminator and DIRI illumination areas.
(Kawano et al. (2015)).

(2-10a) The microfluidic device used with the DIRI illuminator. The illuminated area is almost the entire microfluidic device.

(2-10b) The microfluidic device used with a regular darkfield illuminator. The condenser lens is a DCD condenser, NA 0.8–0.92 (Olympus). The illuminated area is shown by the blue arrow. Note the small area properly covered by the illuminator.

(2-10c) The experimental setup. The left-side camera is an Orca R2. The microfluidic device consists of a special microfluidics module placed upon a plastic adapter plate. The size of the microfluidics module in the photograph is 25 × 75 mm.

With conventional darkfield microscopy, light enters the specimen at an oblique angle and is blocked at the periphery of the optical components. The background of the image is dark, and the specimen appears bright. If the image background is bright, detection sensitivity is considerably reduced, resulting in conditions similar to brightfield microscopy. Darkfield microscopy can often provide enhanced detection sensitivity and contrast for specimens that cannot be effectively imaged using brightfield illumination.

Conventional darkfield units are commercially available for standard microscopes. There are two types of darkfield condenser: dry and oil darkfield condensers. Some phase turret condensers include the required darkfield annulus within the condenser turret. In Fig. 2-10 (b), a dry darkfield DCD condenser (NA 0.8–0.92; Olympus, Tokyo, Japan) is shown below the blue arrow. The illuminated area is limited to a spot (shown by the arrow). Normally, most dry darkfield condensers are capable of illuminating fields of view of 10× to 20× objectives with NA < 0.5. A dry darkfield condenser cannot cover objective lenses with NA > 0.8, such as a 40×, NA 0.95 lens because the illumination cone of light passes directly through the objective lens and eliminates the dark background of the image. Use of the 40×, NA 0.95 objective lens requires optical coverage that can be provided by an oil darkfield condenser. A common practice during imaging sessions is to find the required field of view using a 10× or 20× lens, then to switch to a higher magnification and higher NA objective (such as the 40×, NA 0.95 lens) for image acquisition. However, if the user later needs to switch back to the 20×, NA 0.75 dry lens, the condenser also has to be switched back to the dry darkfield condenser. This necessitates the disruptive and somewhat laborious process of removing oil from the slide as the investigator must begin again with dry optics.

The procedure of switching back and forth between dry and oil systems poses a considerable inconvenience to investigators and may introduce an unacceptable delay into the experimental protocol, rendering some experiments impossible to perform. In fact, this is the case for many microchannel setups with multiple delicate attachments to pumps, drains, sensors, etc.

As described here, the newly developed white-LED DIRI system eliminates the inconvenience and delay inherent in the conventional approach. Thus, experiments can be performed that require frequent or rapid switching of magnification to locate fine details within larger fields of view before acquisition. In addition, the area that is illuminated for DIRI

_____

imaging is larger than a conventional darkfield condenser is capable of illuminating (compare Fig. 2-10a to Fig. 2-10b). Fig. 2-10a shows that the DIRI system can illuminate most of the area of a glass slide. The illumination intensity has also been enhanced in this version of the device. The latest design for DIRI is 1.5-fold brighter than the previous design (Kawano et al. (2013)). Moreover, DIRI can be used with 10× to 100× objective lenses, including both dry and oil objectives. Thus, the DIRI system has important advantages in usability compared to the conventional darkfield condenser.

The DIRI system also has an advantage in terms of the small space required for implementation. The DIRI illuminator is thin and built into the stage insert plate, as shown in Fig. 2-10a. Therefore, it does not interfere with tubes connected to the microfluidics equipment for liquid handling. Our DIRI system is optimized to work with a standard microscope slide measuring 25 × 75 mm. As the size of the microfluidic device used in this study is 25 × 50 mm, we implemented a plastic support plate to adapt the microfluidic device size to 25 × 75 mm. The simplicity of this adaptation is another indication of the robustness and flexibility of our DIRI system as applied to microfluidics.

Our DIRI system was easily installed by simply attaching the LED array to the side of the microfluidics observation location. When we constructed the first prototype, we started from this simple design. By adding automatic control of the confocal illumination, the widefield fluorescence excitation and emission, DIRI, transmitted (brightfield) illumination, stage movement, etc., a more sophisticated system can be constructed (cf. Fig. 2-10c).


2.2.2 Experimental setup and procedures for microfluidic observation

In Chapter 3, we will describe three types of experiment: Section 3.1 observation of microbubbles by a combination of brightfield and DIRI imaging; Section 3.2 observation of fluorescent tracer particles by a combination of fluorescence and DIRI imaging; and Section 3.3 observation of two types of stained cells by combination of multiple fluorescence imaging and DIRI imaging.

In all of these experiments, we used the Virtual Slide System VS120 (Olympus) including the VS-ASW WSI software (ver. 2.7) as a base system, with cellSens software (ver. 1.9; Olympus Soft Imaging Solutions, Münster, Germany) for video and 3D imaging. We attached a BX-DSU spinning disk confocal system (Olympus) to the VS120 system for confocal observations. We also attached the DIRI illuminator as in our previous study (Kawano et al. (2013)) for WSI. Before use, this integrated system was calibrated using the VS-ASW software and the recommended calibration slide from the manufacturer. The system described here is a prototype and is not commercially available.

A photograph of the system is shown in Fig. 2-10c, and the optical layout is shown schematically in Fig. 2-11. The DIRI system consists of LEDs attached to the microscope stage (Kawano et al. (2013)), which enables visualization of the sample by refractive index mismatch. The DIRI system can be used with widefield fluorescence or confocal imaging. A microfluidic device on an appropriate stage adapter is placed on the stage, and the condenser lens for the transmitted illumination is set up about 10 mm below the Köhler illumination position. The condenser lens is located between the stage and the mirror unit below the stage (not shown in Fig. 2-11). The halogen lamp is used for transmitted illumination. The spinning disk confocal system is set between two dichromatic mirrors (cf.

Fig. 2-11). Mercury vapor short-arc lamps are used for confocal and fluorescence illumination. The observed images are recorded with a CCD camera (Orca R2; Hamamatsu Photonics, Hamamatsu, Japan). We typically use the Orca R2 camera for all modes of image capture, including DIRI, fluorescence, confocal, and brightfield imaging.
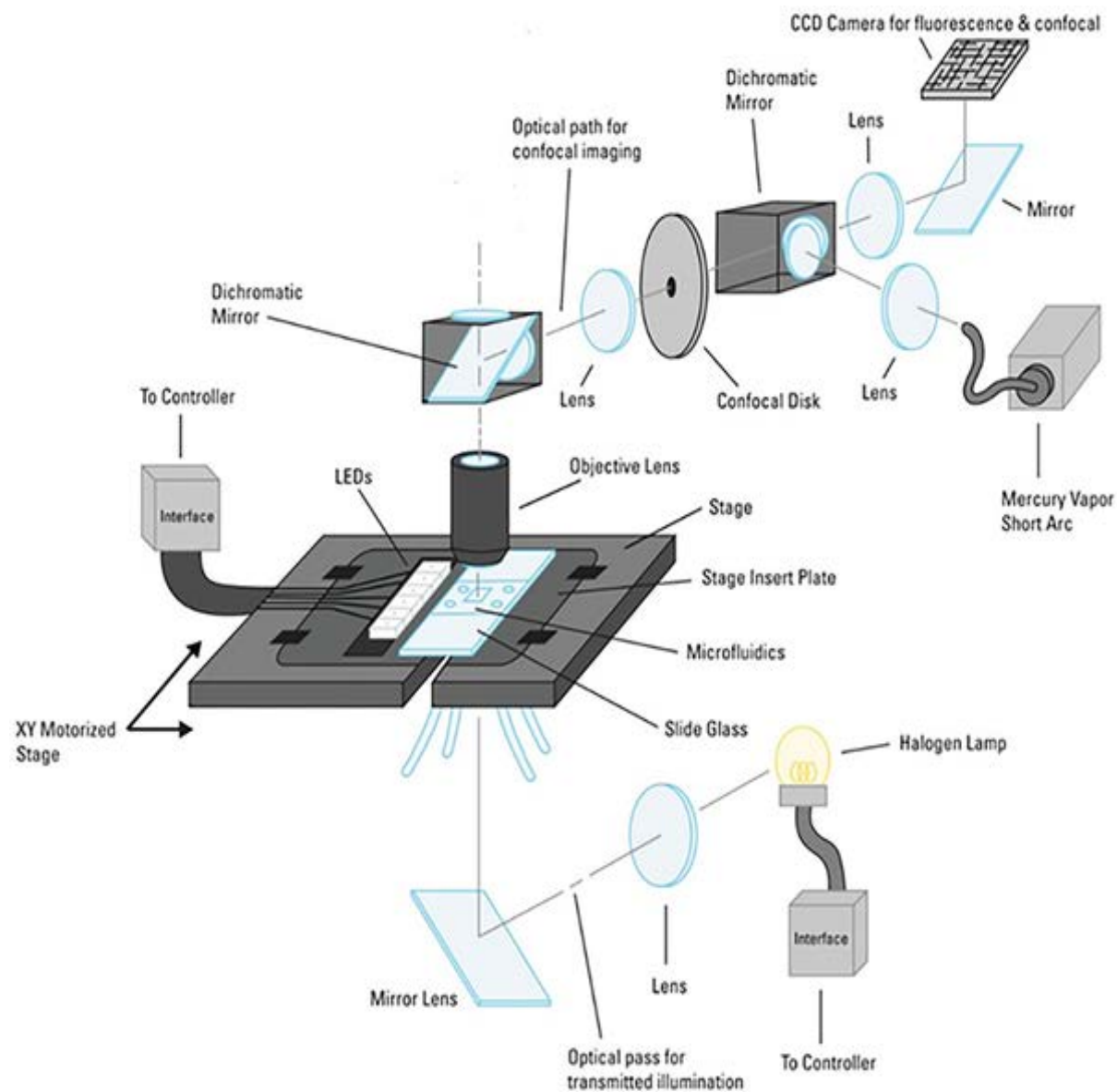
Fig. 2-11 Schematic drawing of a microfluidic observation system. (Kawano et al. (2015)).

This system is capable of brightfield, DIRI, conventional fluorescence, and confocal imaging. The DIRI image was obtained by illumination using the LEDs at the side of the slide. The system can also provide WSI.

Fig. 2-12 shows the microfluidic device used in this study (SynVivo Bio-chip Microvascular Network; CFD Research Corporation, Huntsville, AL). The original device measures 25 × 50 mm with a thickness of 2 mm (Fig. 2-12a), and the top surface is covered with a coverslip 0.17 mm thick. The microchannel network is molded into the polydimethylsiloxane (PDMS) block that composes the microchannel device. For this device, the channel width is about 100 μm. Ports A and D in Fig. 2-12b are the inlet and outlet for fluid flow, respectively. Ports B and C are closed but are used to remove bubbles in the channel before the experiments. The fluid flow is generated by manipulating a syringe (Norm-Ject, 1 mL; Henke Sass Wolff, Tuttlingen, Germany) with a programmable syringe pump (Model Fusion 200; Chemyx Inc., Stafford, TX). The refractive index of PDMS is approximately 1.41, the buffer has a refractive index similar to water (n = 1. 33), and that of cells is in the range 1.35–1.40. When we used DIRI to buffer-filled channels, scattered light was observed at the interface between the two materials (channel walls) due to their differing refractive indexes.
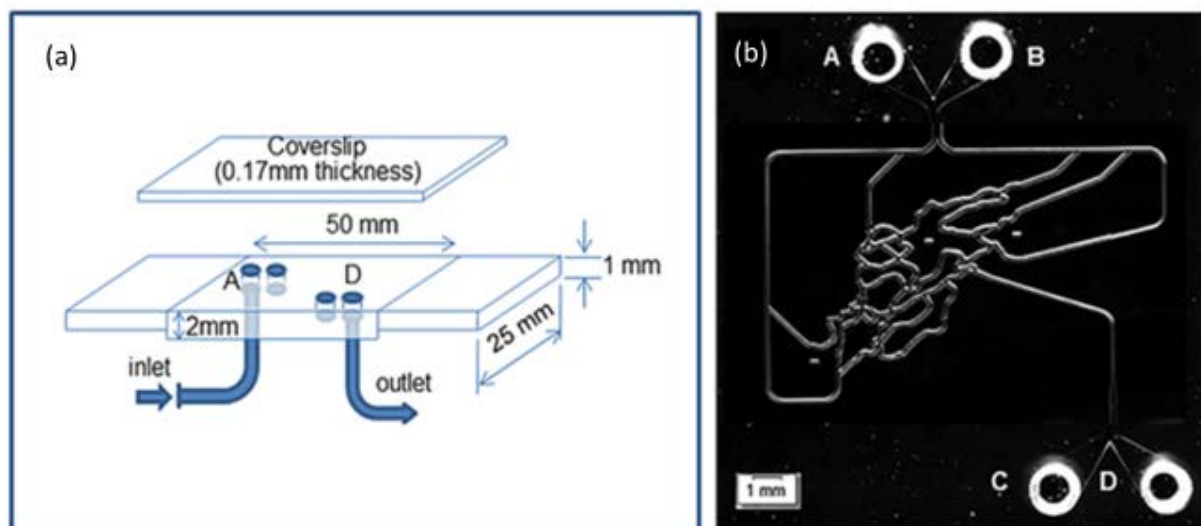
Fig 2-12   Microfluidic device. (Kawano et al. (2015)).

(2-12a) Schematic of the entire plate. The microfluidic module itself was 25 × 50 mm, which was extended to 25 × 75 mm by the addition of a plastic adapter plate.

(2-12b) Channel geometry within the microfluidic device. The image was taken using DIRI. Port A is the inflow port, and port D is the outflow port. Ports B and C are closed during the experiment.

In the microbubble experiment, we added a diluted surfactant (Triton X-100; Sigma-Aldrich, St. Louis, MO) to phosphate-buffered saline (PBS). The bubbles were generated manually by pushing the syringe plunger back and forth before the experiment. Then, the two-phase fluid was injected into the channel manually using the syringe.

For our fluorescent bead experiments, we added diluted surfactant (Triton X-100; Sigma-Aldrich) to phosphate-buffered saline (PBS) to avoid adhesion of the beads to the channel

_____

walls. We used fluorescent beads 1 μm in diameter (F8823 FluoSpheres fluorescent beads; Invitrogen, Carlsbad, CA) diluted with PBS.

In the cell experiments, we used two types of cell emitting two different colors under fluorescence illumination: human umbilical cord blood endothelial cells at the fourth passage (HUVECs, #KE-4109; Kurabo, Osaka, Japan) and fibrosarcoma cells (HT1080; American Type Culture Collection, Manassas, VA). All cells were incubated at 37°C in 5% CO_2. The endothelial cells were stained with 10 μg/mL Rhodamine 123 (Wako, Osaka, Japan) and emitted green fluorescence when illuminated with blue light. Fibrosarcoma cells were stained using Mito Tracker Red CMXRos (Life Technologies, Gaithersburg, MD) and emitted red fluorescence when illuminated with green light. The numbers of endothelial cells and fibrosarcoma cells were adjusted to 6×10^5/mL. Before the introduction of cells into the microchannel device, the channels were coated with fibronectin to promote adhesion to the channel walls.

In all of these experiments, we used DIRI from only one side of the microfluidic device. Therefore, the DIRI induced asymmetric illumination. More isotropic illumination could be created by the attachment of additional DIRI illuminators located around the periphery, creating concurrent illumination from multiple directions. For example, DIRI illuminators could be attached to both sides of the sample or surrounding the sample.

Section 3.2 explains the experimental results for DIRI when used for microfluidic observation.

_____

2.3 Development of DIRI combined with total internal reflection (TIRF) microscopy

In this chapter explains TIRF microscopy using with numerical aperture 1.45 objective, 1.65 objective and TIRF illuminator. Later, explains the combination of TIRF microscopy and DIRI.

2.3.1 Theory of total internal reflection (TIRF) microscopy

Total Internal Reflection is an optical phenomenon that can be employed to observe events occurring at two different refractive index boundaries. When a light strikes the interface between two optical media of different refractive indices, the light incident at an angle greater than the critical angle undergoes total reflection. Beyond the angle of total reflection, the electromagnetic field of the incoming/reflected light still extends into the Z direction vertical to the interface plane (see Fig. 2-13). The intensity of this field, called an evanescent wave, decreases exponentially from the surface, and its effects extend only a few hundred nanometers into the second medium. That portion of the specimen within the evanescent field can be excited to emit fluorescence and consequently can be seen or recorded. This is the essence of TIRF microscopy.

Fig. 2-13 is a schematic drawing of the wavefronts of a laser beam incident on the interface between two media. The arrow shows the direction of the laser. The light is reflected at the interface while the evanescent wave extends into the Z direction. The intensity of the evanescent wave decreases exponentially (see formula 2.4). A fluorophore near the interface is excited and emits fluorescence.

_____
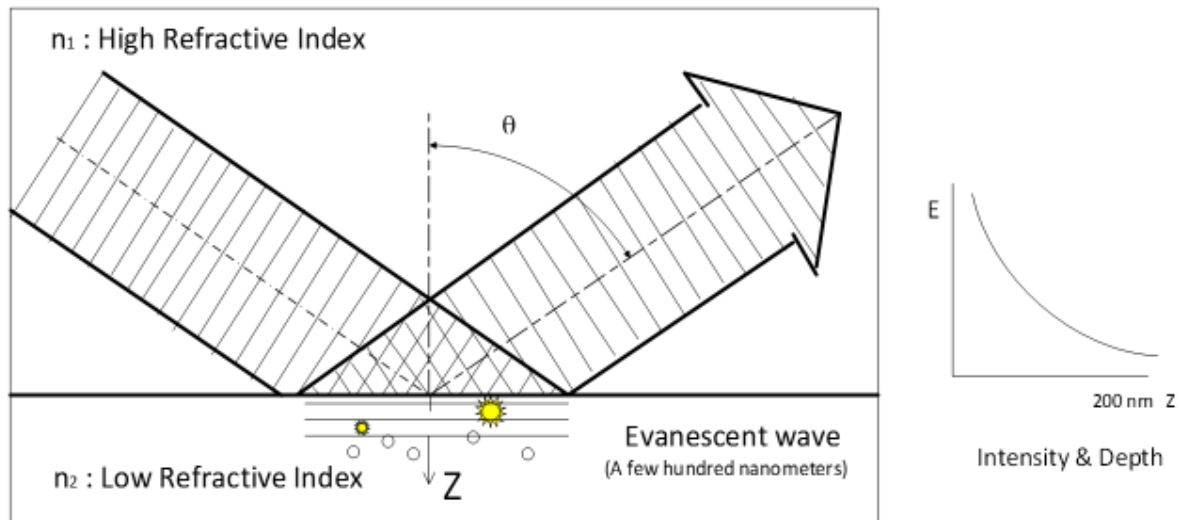
Fig. 2-13 Schematic for Total Internal Reflection (TIR) at the plane where two different refractive indices interface. (Kawano et al. (1999, 2000)).

The condition of total reflection is given by the following equation:

$$\theta\ (c)\ \geq sin^{-1}\ (n_2\ /n_1),\ where\quad n_1 > n_2 \tag{2.3}$$

where n_1 is the refractive index of the glass, n_2 is the refractive index of the specimen, and θ is the illumination angle. When the illumination angle θ is greater than the critical angle $\theta\ (c)$, then illumination light produces the evanescent wave. The intensity of the electric field (E) decreases exponentially according to the distance from the surface (Z). Therefore, the intensity of the evanescent wave decreases exponentially. β is a space constant.

$$E = E_0\ e^{-\beta z} \tag{2.4}$$

$$\beta = \frac{4\pi n_1}{\lambda}\ \sqrt{sin^2\ \theta - \left(n_2/n_1\right)^2} \tag{2.5}$$

The depth of the evanescent wave $(\cong 1/\beta)$ is illumination-angle (θ) dependent. As the illumination angle increases, the depth of the evanescent wave decreases. λ is the wavelength of light in a vacuum.

_____

The key advantage of TIRF microscopy is that the penetration of the illumination light, which is an evanescent wave, is shallow. Only fluorophore molecules very close to the surface of the glass are excited to emit, creating an extremely thin optical chapter. Outside the evanescent field, fluorescence is minimal. This effect leads to images of very high contrast.

Variations of TIRF microscopy

Many types of TIRF microscopy setups have been developed (Fig 2-14). The following two types are most widely used:

1) Prism TIRF microscopy. This setup requires a prism to create an evanescent wave. It is relatively easy to accomplish since it requires only a microscope, a prism, and a laser. All components are readily available. The drawback of this setup is that the specimen must be positioned between the prism and the cover glass, significantly limiting specimen manipulation.
2) Objective lens TIRF microscopy. Objective-type TIRF microscopy requires the illuminating laser beam to be passed through the microscope. This setup is based on using an objective lens of NA 1.40 or greater. This is because when the illumination NA is greater than 1.38, light is reflected from the surface of the cover glass, and the evanescent wave excites the surface of the specimen, while at NA 1.38 or lower, light travels through the specimen, producing "far field" illumination. When the NA is below 1.38, the entire specimen fluoresces and a TIRF image is not formed. For objective-type TIRF, the specimen must be located at the top surface of the cover glass. Open space above the specimen may permit the use of the other instruments such as micromanipulators, DIC optics, or even a scanning probe microscope.

1) Prism type TIRFM   2) Objective Lens type TIRFM

_____
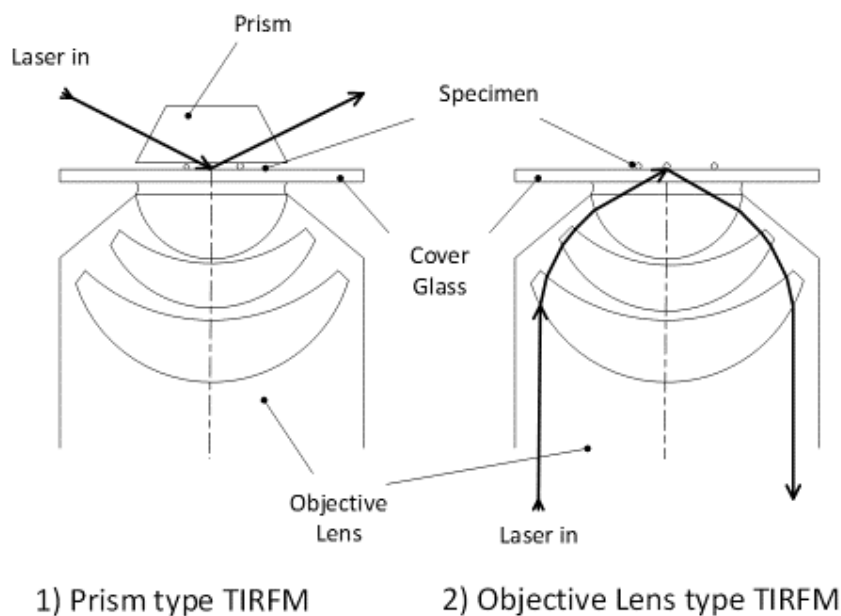
Fig. 2-14 Schematic comparison of common instrumental approaches of TIRFM. (Kawano et al. (1999, 2000)).

1) Prism type TIRFM requires a longer-working-distance objective to observe the top surface of the prism.

2) Objective lens type TIRFM accepts higher-numerical-aperture, shorter-working-distance objectives.

2.3.2 Experimental setup in section 3.3

Using a high-NA objective lens for total internal reflection

Using high-refractive-index glass, we developed an objective lens with an NA of 1.65 (Apo100×NA1. 65, Olympus Optical Co., Japan) (Terakawa et al. (1997)). Its performance greatly exceeded that of the Plan APO 100×, NA 1.40 (Olympus Optical Co.) that previously had been the highest-NA objective lens among biological objective lenses with the exception of a solid immersion objective lens (Terakawa et al. (1997)).

Living cells typically have a refractive index of 1.33-1.38. To achieve total internal reflection, they must be illuminated with a lens whose NA is greater than 1.38 (Table 2-1). The condition is expressed in Eqs. (2.3) and (2.6):

$$NA \ = \ n \, sin \, \theta \qquad\qquad (2.6)$$

where NA is the numerical aperture of the objective lens, n is the refractive index and θ is the angle. The excitation light must pass through the portion of the numerical aperture cone of the lens that is greater than 1.38. With a high-performance plan apochromatic NA 1.4 objective, a very small fraction of the NA (1.40-1.38 = 0.02) can be utilized for excitation. Although it is possible, it is very challenging to align the illuminating laser. Even with a perfect alignment, increasing the light intensity is difficult because the margin is minuscule. An APO 100x, NA 1.65 has much greater NA latitude (1.65-1.38 = 0.27; angle, 6.15 degrees), making it easier to introduce the excitation light through the exit pupil of the objective lens (Fig. 2-15a and Table 2-1). In order to maintain the NA and to achieve a high-quality image, a special immersion medium with a high refractive index (immersion liquid: Nd = 1.78, Cargille Laboratories, Cedar Grove, NJ, USA) must be used (NOTE: this liquid is volatile and should be handled using Good Laboratory Industrial Practice). Also, the cover glass must have a high refractive index (n_{ct} = 1.788; Olympus Optical Co.).

The APO 100×, NA 1.65 objective requires a custom cover glass and immersion liquid of a high refractive index, but some applications do not work with the custom cover glass and immersion liquid. Therefore, we created an option, modifying a 60×, NA 1.40 objective lens to create a 60×, NA 1.45 objective. The latter lens does not require the special cover glass or special immersion liquid, and thus can be used for those applications where the NA1.65 objective is not suitable. Optically, the total reflection angle of this lens is the same as that of

a Plan APO 60x/NAI.40 lens. The margin of TIRFM illumination is 0.07 (l. 45-1.38 = 0.07; angle, 7.52 degrees).

(a)   (b)
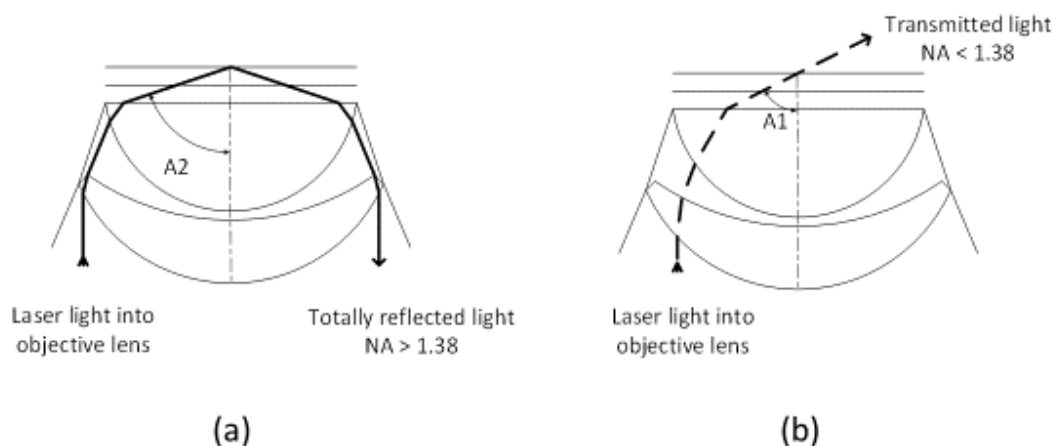
Fig. 2-15   Transmitted light and totally reflected light. (Kawano et al. (1999, 2000)).

(2-15a) Illumination at the edge of the objective lens, creating total internal reflection illumination.

(2-15b) Illumination far from the edge of the objective lens, showing the light path through the sample providing transmitted laser illumination.

When the illumination NA is greater than 1.38, light is reflected from the surface of the cover glass, and the evanescent wave excites the surface of the specimen. When the illumination NA is less than 1.38 the light travels through the specimen, producing "far field" illumination. Under this condition the entire specimen fluoresces; a TIRF image is not formed. To overcome the problem, Suzuki and Fujimoto designed APO 100×NA 1.65 and 1.45 objectives (Suzuki (1997); Fujimoto et al. (2004)).

Table 2-1   Total reflection angles and maximum angles of objective lenses. (Kawano et al. (1999, 2000)).

Objectives	n_1	n_2	Total reflection Angle A1 (NA)	Max. Angle A2 (NA)
NA	Immersion Oil	*Cells	65.63 Degrees	67.53 Degrees

_____

| 1.40	1.515	1.38	(1.38)	(1.40)
NA 1.45	Immersion Oil 1.515	*Cells 1.38	65.63 Degrees (1.38)	73.15 Degrees (1.45)
NA 1.65	Immersion Liquid 1.78	*Cells 1.38	50.83 Degrees (1.38)	67.97 Degrees (1.65)

* The refractive index of the cell is assumed.

This margin is ample enough for TIRFM illumination. The plan APO 60×/NA 1.45 objective lens is able to reduce experimental costs as well, because standard cover glasses are much less expensive than custom cover glasses.

These high NA lenses, particularly the NA 1.65 lens, can be used in other applications as well. High near-IR transmission is useful for laser trapping ($T_{1064\ nm}$ = 60% for APO 100x/NA 1.65). A DIC prism is available for a high-resolution DIC observation with these lenses. For fluorescence microscopy, the 100×, NA 1.65 lens gains an intensity more than 5 times the 100×, NA 1.40 objective lens when the specimen is placed very close to the cover glass. The techniques of TIRFM, DIC, and standard fluorescence microscopy can also be combined.


Design and setup for TIRF illuminator

An inverted microscope (model name IX70, Olympus, Japan) was used for the present setup. We improved the handling of the TIRFM illuminator. We used to use an optical bench to set up optical components including a laser, beam expander and mirrors. This setup required expertise to facilitate accurate adjustment of the illumination. The new illuminator aimed at a one-touch adjustment for TIRFM illumination. A laser source was placed at the side of the microscope. The laser and illuminator were connected with single-mode fiber to conduct laser light to the microscope (see Fig. 2-16, 2-17a and 2-17b, the details given in Tables 2-2). The laser was projected into the exit pupil of the objective lens (see Fig. 2-16). A camera was attached to the side port of the microscope. The illuminator was adaptable to accommodate a mercury, xenon, or laser source. The illumination could be switched from the TIRF mode to the epi-fluorescence mode. As a light source, a low-noise 25 mW, Nd-YAG laser, emitting at 532 nm, was usable. Argon, He-Ne, and krypton lasers also could be used, either by direct coupling or via optical fiber.

_____
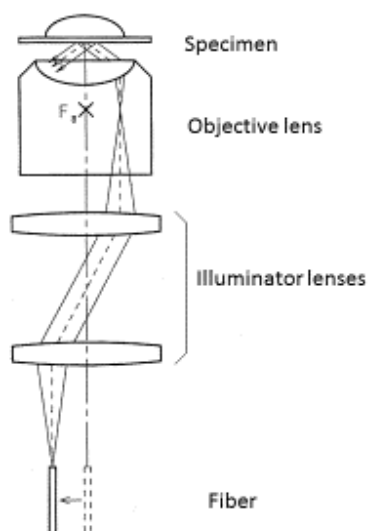
Fig. 2-16   Fiber illumination system for TIRFM. (Kawano et al. (1999, 2000)).
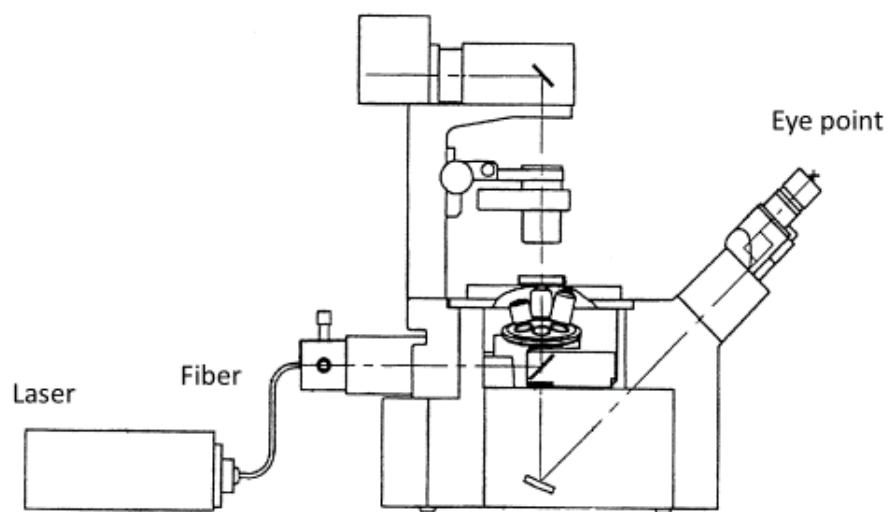
(a)
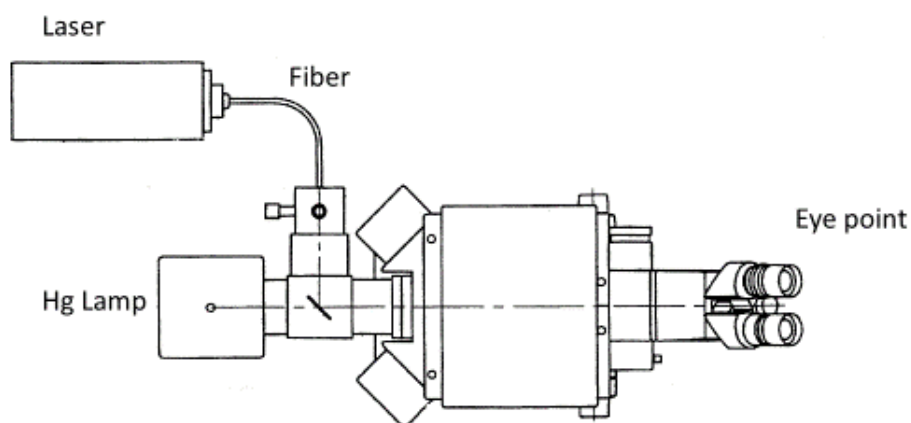
(b)

Fig. 2-17   Inverted microscope with TIRFM illuminator. (Kawano et al. (1999, 2000)).

(2-17a)   Inverted microscope with TIRFM illuminator (side view)

(2-17b)   Inverted microscope with fiber type TIRFM illuminator (top view)

Table 2-2   Setup for TIRFM. (Kawano et al. (1999, 2000).

DESCRIPTION	Quantity
IX701F: Inverted Scope	1
TIRFM Illuminator	1
Transmitted Illuminator	1
DIC Kit	1
Mercury Lamp House	1
Photo Lens 2.5x	1
C-Mount adapter	1
UPLAPO 10x/NA0.4	1
PLAPO 100x/NA1.40	1

PLAPO 60x/NA1.45	1
APO 100x/NA1.65	1
Cover Glass for APO 100x/NA1.65, 5-piece set	1
(Cargille Lab.) Cargille Lab. Immersion liquid: n_d = 1.78, ¼ oz.	1
(Uniphase) Nd-YAG Laser 532 nm 50 mW	1
(Crysta Laser) 532 nm 25 mW Laser	1

DIRI combined with TIRF microscopy

We recently combined a DIRI system with TIRF microscopy. Olshausen and Rohrbach originated Coherent total internal reflection dark-field (CTIRDF) microscopy; this technology uses objective-type TIRF illumination without the emission filter, and can be used to produce a darkfield image. The system presents a coherent image produced from the combination of evanescent illumination via TIR with darkfield microscopy. This system provides images of scattering samples near the coverslip with good lateral resolution. This technique is very useful for doing super-resolution imaging (von Olshausen et al. (2013)).

We considered both the CTIRDF and DIRI, and decided to use DIRI. One of the advantages of DIRI is illuminating the whole sample, which enables us to observe the sample using low to high magnification objectives. We set up DIRI on top of the inverted microscope stage. We put the microfluidics on top of the stage. Then we observed the beads in the microfluidics using fluorescence, TIRF, and DIRI.

Section 3.3, explains the setup for our inverted microscope (IX81, Olympus, Japan) with the IX2-TIRF illuminator. The system was equipped with argon (488 nm) and He-Ne (633 nm and 543 nm) lasers. We attached an ImagEM 1K EMCCD camera (Hamamatsu, Japan). Fig. 2-18 is shows this system set up for TIRF with DIRI. We also used HCImaging acquisition software from Hamamatsu, Japan.

DIRI uses commercially available rectangular white LEDs in an array we assembled by hand using a soldering machine. The LED Illumination intensity is 3-to-7.5 volts. The LED light voltage is fixed based on observation of the image on the computer monitor.

We used Microfluidics (SynVivo Bio-chip Microvascular Network; CFD Research Corporation, Huntsville, AL). This is the same device used in section 2.2 (Fig. 2-12). Because we used an inverted microscope, we did not have to attach 1 mm thickness support parts to the side of the microfluidic device. Ports A and C in Fig. 2-12b are the inlet and outlet for fluid flow. Ports B and D are closed. The fluid flow is generated by manipulating a syringe (Norm-Ject, a 1 mL Henke Sass Wolff, Tuttlingen, Germany) pump with a programmable syringe (Model Fusion 200; Chemyx Inc., Stafford, TX). The flow speed was

_____

0.005 ml/min. After image acquisition, the image was handled by using Fiji software with a Bioformats plug-in. When we used DIRI with buffer-filled channels, scattered light was observed at the interface between the two materials (channel walls) due to their differing refractive indexes.

For our fluorescent bead experiments, we used phosphate-buffered saline (PBS). We did not use any channel coating. I loaded the diluted fluorescent beads. We used 10 µl of fluorescent beads 0.22 µm in diameter (FC021; Surface COOH/1 coated Flash Red beads, Bangs Laboratories, Inc. Fishers, IN, USA) diluted with 3.5ml of PBS. The excitation wavelength used was 633 nm.
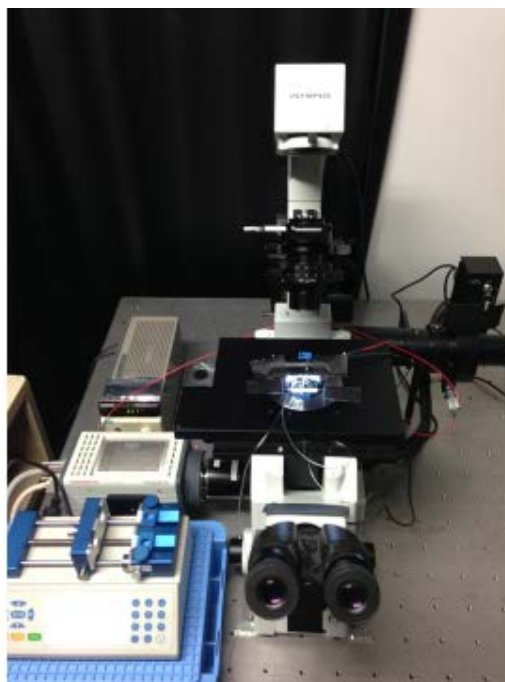
**Fig. 2-18   Attached Darkfield Internal Reflection Illumination (DIRI)
to Total Internal Reflection Fluorescence (TIRF) Microscopy.**

At left is the attached TIRF illuminator. The DIRI system is on the
microscope stage and is turned on.

The images below (Fig. 2-19) show directly observed images of microfluidics. Fig. 2-19a shows microfluidics with both DIRI and TIRF turned on. Fig. 2-19b is the microfluidics image using DIRI off and, with the laser illumination angle is setup for fluorescence mode (TIRF off).

_____

- 53 -
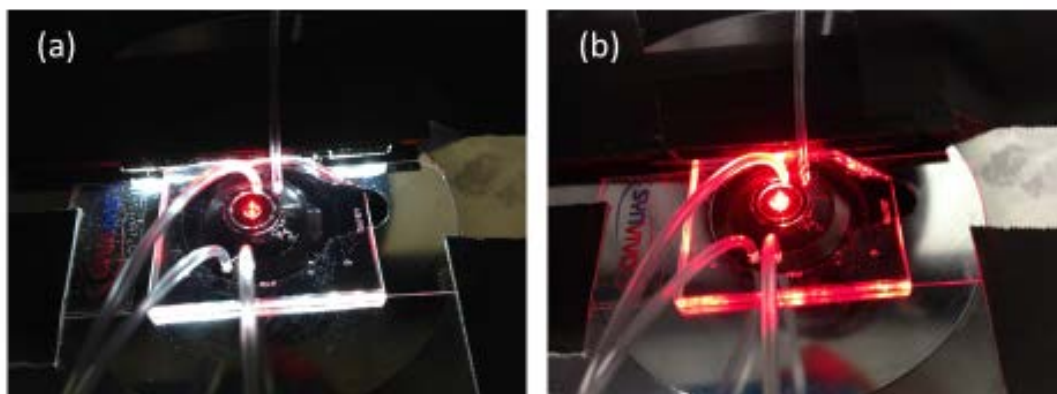
Fig. 2-19 Microfluidics stay on the stage of the inverted microscope.

(2-19a) Illuminated with DIRI and TIRF (excitation wavelength 660 nm).

(2-19b) Setup in widefield fluorescence mode for TIRF illuminator, DIRI off.

We evaluated the image using DIRI and TIRF microscopy. We changed the laser illumination angle to switch between widefield and TIRF illumination. Switching these two observation methods, we changed the laser illumination angle. Then the microscope can be used for both wide-field fluorescence and TIRF imaging. The illumination laser light illuminates the very edge of the objective lens, totally reflecting light to provide a TIRF image (see Fig. 2-19a). When the illumination laser is moved toward the center of the objective lens, then the illumination light does not provide total internal reflection, and we achieve a fluorescence image instead (see Fig. 2-19b). Using this effect, we observed both TIRF and wide-field fluorescence images.

_____

Chapter 3   Experimental results

Here, section 3.1 explains the experimental results for DIRI using brain slices and TMA. Section 3.2 explains the experimental results for DIRI using microfluidics. Section 3.3 explains the experimental results for DIRI using TIRF microscopy.

_____

3.1 Brain slice observation by DIRI

Section 3.1 explains the experimental result for (a) DIRI with white LEDs observing brain tissue, (b) DIRI with three-color LEDs observing brain tissue and TMA. It then offers conclusions for this section.

3.1.1 Results and discussions

a. DIRI using white LEDs

Imaging of DAB (3, 3'-Diaminobenzidine)-stained specimens using DIRI

DAB (3, 3'-Diaminobenzidine)-stained brain chapters were imaged with a 20× objective, using brightfield mode (Fig. 3-1a), darkfield mode using DIRI (Fig. 3-1b) and a traditional darkfield substage condenser (Fig. 3-1c). DIRI also was used with a 40× objective (Fig. 3-1d). We did not collect any images with the substage darkfield condenser when using the 40× objective, as the severe mismatch of the lens NA and the substage condenser resulted in grossly inadequate darkfield images, with excessive glare, loss of contrast and degradation of the darkfield image.
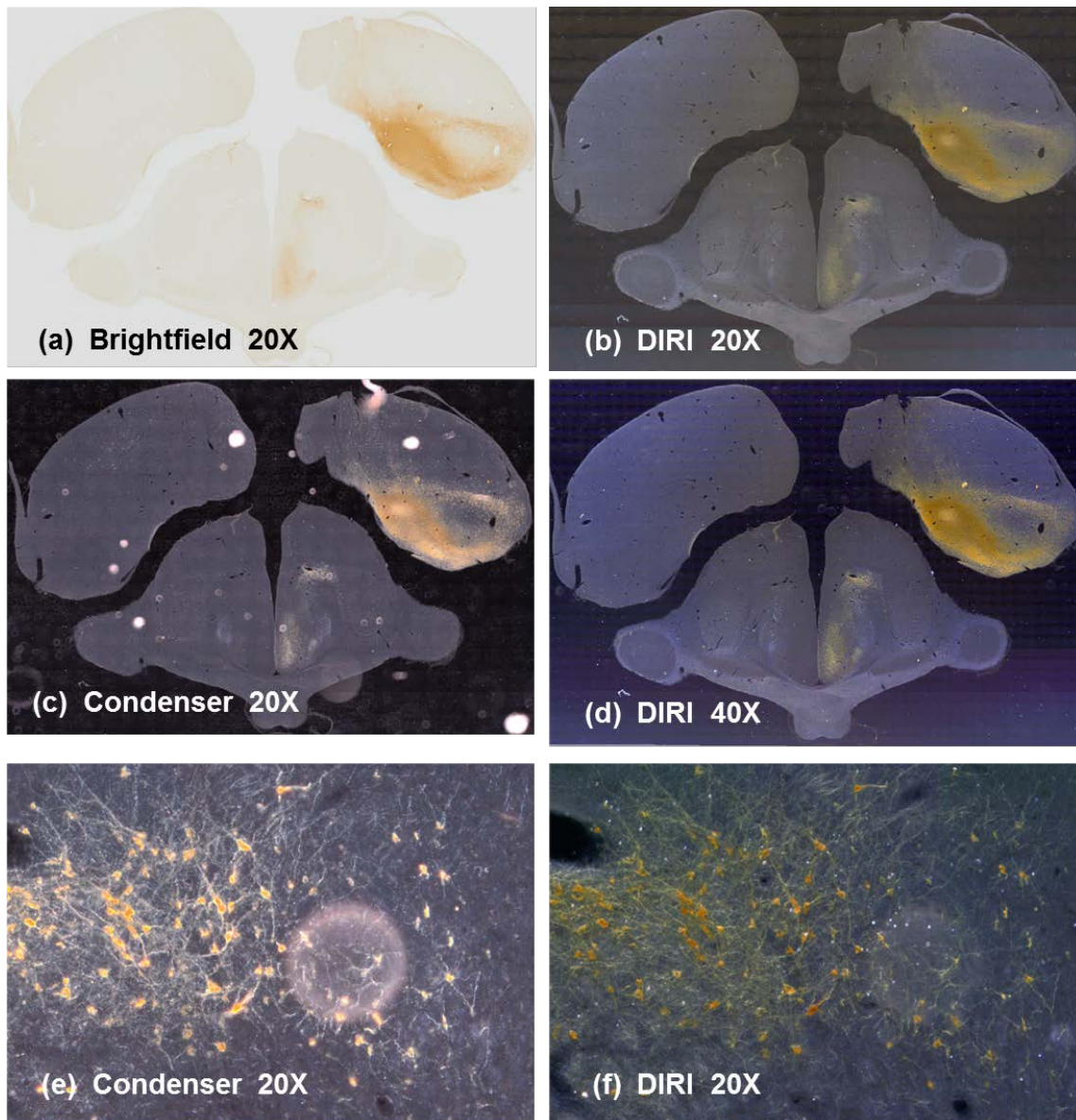
Fig. 3-1 Comparisons of a variety of imaging methods used to depict DAB specimen showing anterograde and retrograde transport of Cholera Toxin B tracers in a chick brain with an injection of tracer in the medial Arcopallium (amygdala). (Kawano et al. (2013)).

Darkfield illumination with either a traditional darkfield substage condenser or with the edge-illumination method described herein readily demonstrates the presence of fine unmyelinated axons and dense terminal fields in the hypothalamus.

(3-1a) DAB-stained brain chapter, 30 um thick, mounted on a 1×3-inch microscope slide glass and with a #1 coverslip. This WSI image was scanned in brightfield using a 20×, NA 0.75 objective lens.

(3-1b) The same specimen was scanned using WSI with DIRI system, using the same 20× objective lens.

_____

(3-1c) WSI image with a traditional darkfield substage condenser using 20× objective lens with motorized condenser lens (U-UCDB) with the darkfield annulus (U-DFA). The light source is a halogen lamp. Dirt on the surface of the slide produces a number of distracting bright objects in the resulting image.

(3-1d) WSI image with DIRI system using a 40×, NA 0.95 objective lens. Although a traditional motorized substage condenser and darkfield annulus are not compatible for use with an NA 0.95 objective lens, side-illuminated darkfield provides a clear, crisp darkfield image.

(3-1e) WSI with traditional darkfield substage condenser and illuminator. Despite careful efforts to clean the slide, the specimen has some dust on the surface of the coverslip. The out-of-focus dirt obscures part of the image.

(3-1f) WSI image of the same specimen shown in Fig. 5e, captured using with DIRI system. The out-of-focus dirt on the coverslip, though still evident, is less intrusive.

A major shortcoming in the application of traditional darkfield imaging using a substage darkfield condenser has been the deterioration of the image due to dust (or artifacts) on either the top or bottom surface of the slide. To compare the DIRI images with traditional darkfield, we examined the same specimens with dust on the top of the coverslip, using a darkfield substage condenser with a 20× objective lens (Fig. 3-1e). The same specimen was also viewed with the side illuminated darkfield. (Fig. 3-1f). The out-of-focus dirt was less intrusive in the final image when captured using side-illuminated darkfield imaging.

Image acquisition conditions were as follows: Acquisition of one brain chapter (14.5 mm×9. 7 mm) required 442 of the 20× images to build a single whole slide image (Fig. 3-1a, b and c). This required 5 minutes, 21 seconds total acquisition time. Using a 40× objective (14.4 mm×9. 6 mm) we needed 1734 images to produce a single whole slide image (Fig. 3-1d). Acquisition at 40× required 21 minutes, 30 seconds.
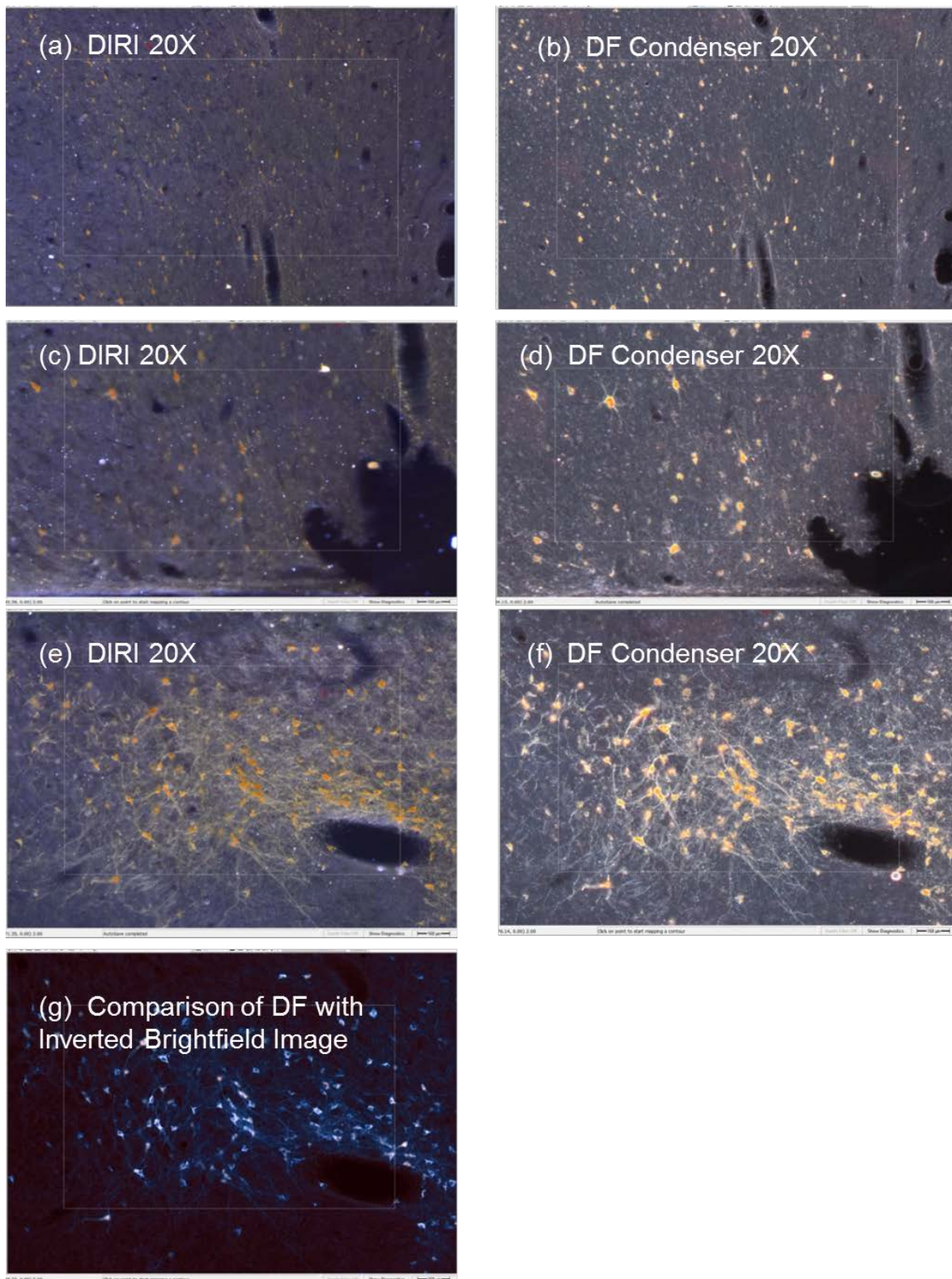
Fig. 3-2   Comparison of matched pairs of WSI images using DIRI side illuminator and traditional darkfield substage condenser. (Kawano et al. (2013)).

_____

Three WSI images using DIRI system (Fig. 3-2a, c) are compared with traditional darkfield substage condenser images (Fig. 3-2b, d). Each pair of photos (Fig. 3-2a–b and 3-2c–d) depict the same region of a slide. The images are used the DIRI system initially do not appear as robust as those taken with a darkfield substage condenser.

Further examination of the images reveals that the images obtained with the DIRI system are more accurate representations of the cells and their processes. The substage darkfield condenser typically results in excessive light scatter. Differences in brightness and color of the individual cells with the DIRI system versus the substage darkfield condenser is due in part to the difference in brightness of the illuminators and the spectral features of the illumination sources.

(3-2e) shows the same region depicted in Fig. 3-2c–d, but is based upon a brightfield image that was then inverted to provide a "pseudo-darkfield" effect. Either darkfield method provides much better detail of the microscopic field than the inverted image in Fig. 3-2e.

To test the possibility, we used image processing software to make a simple contrast inversion of the brightfield image (Fig. 3-2e). Then we compared the DIRI image (Fig. 3-2c), darkfield condenser image (Fig. 3-2d), and contrast inverted image (Fig. 3-1e). The DIRI system (Fig. 3-2d) provided a satisfactory image of the fine detail evident following darkfield acquisition. The image does not have halo, in contrast to the high-contrast darkfield condenser image, which has halo on the edges of neurons. A contrast inversion image allowed observation of the neuron but image quality was not as good as when using either DIRI or the darkfield condenser image. Although cells were now shown in higher contrast and with a higher signal-to-noise ratio (SNR) than in the brightfield image, the finer detail of neuronal processes was no longer evident in the inverted image.

Using the 20× objective, we then compared exposure times for capturing an image of the DAB-stained brain slice specimen using the transmitted-condenser-darkfield illuminator and then using DIRI. Transmitted darkfield required an exposure time of 5 msec. DIRI required an exposure time of 700 msec. The exposure time for DIRI was longer than that of the transmitted-condenser-darkfield illuminator. Transmitted darkfield also provided a higher-contrast image. The disparity in exposure times was largely attributable to the overall lower intensity of illumination provided by the edge-illuminating LEDs, compared to the high-intensity halogen light source used with the substage darkfield condenser.

In addition, substage condenser illumination exaggerated staining due to the recruitment of substantial quantities of out-of-focus information. The DIRI side-illumination system did not require precise alignment of a substage condenser, worked well with objectives at all magnifications, and was relatively immune to small particles on the surface of the slide or coverslip.

Using darkfield illumination with a traditional substage condenser (Fig. 3-2b, d, and f) we produced images with very high SNR, with prominent halos around the somata of neurons, dendrites, and axons. Though the resulting images provided high contrast for the cells and processes, they appeared to be much larger than their dimensions using traditional methods of imaging with transmitted light and differential interference contrast. However, DIRI (Fig. 3-2a, c, and e) produced much less halo using the side-scatted light illumination. In the

_____

resulting DIRI images, neuronal somata appear as more accurate representations of the true sizes of the cells and processes.

Superimposing images using fluorescence and DIRI

Fluorescence imaging is another modality used to observe proteins and gene distributions in tissue. Scientists often use immune-labeled fluorescence markers, genetically engineered fluorescent proteins and fluorescence in-situ hybridization (FISH) to observe specific proteins or genes using a fluorescence microscope. To ensure accurate analysis of the distribution of genes or proteins in the tissue, these techniques usually require counterstains to visualize the corresponding cytoarchitecture of the specimens. However, counterstaining may be problematic if multiple proteins or genes are involved. Most fluorescence microscopes have three-to-five fluorescence channels and scientists usually prefer not to lose one fluorescence channel to counterstaining to observe cytoarchitecture information because that reduces the number of fluorescence channels available for investigating proteins or genes. DIRI provides a potential solution by providing cytoarchitecture information based on refractive index mismatches without reducing the number of channels available for fluorescence visualization (DIRI is not for visualizing a fluorescent molecule image).

We imaged fluorescent molecules within the chapter of brain tissue using an incident light fluorescence illuminator. Fluorescent images were captured using a 10× objective lens (Fig. 3-3a) and DIRI images were collected using a 20× objective lens. The images were then superimposed (Fig. 3-3b). The composite image shows not only protein localization (green) but also details of myelinated tracts, and prominent cell groups, which facilitate identification of brain structures containing the fluorescent label. Observation of DIRI (Fig. 3-4a) and fluorescence (Fig. 3-4b) channels, along with composite images of both techniques (Fig. 3-4c) revealed the structure of the brain as well as protein distribution.

_____
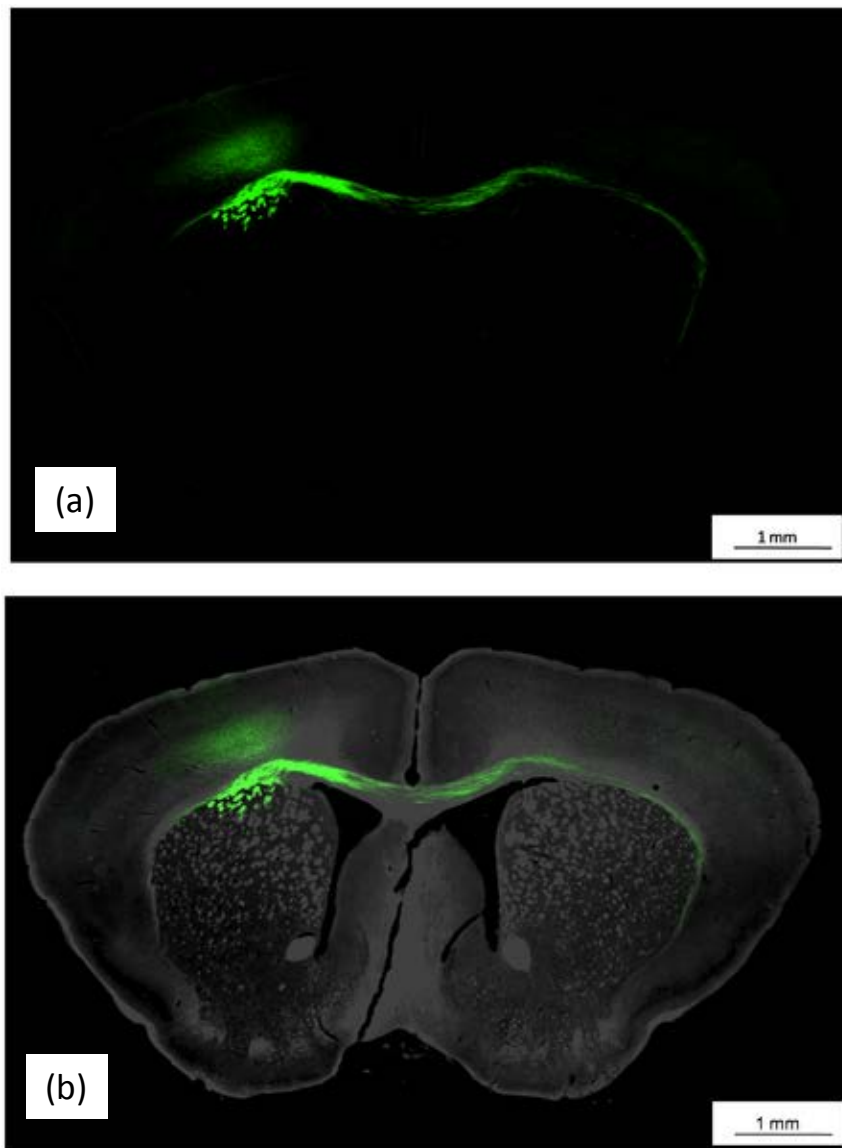
Fig. 3-3   Visualization of the anatomy of a coronal mouse brain slice with fluorescent cell tracer. (Kawano et al. (2013)).

(3-3a) Fluorescent image captured using a 10× objective lens.

(3-3b) The same fluorescent image superimposed on a darkfield DIRI image. The superimposed image provides substantially more detail and anatomical context; the darkfield image depicts neuronal cell bodies and fibers while the fluorescent label provides visualization of selected axonal projections. The acquisition time was 40 seconds for a 10× fluorescent image and 5 minutes for a 20× darkfield image.
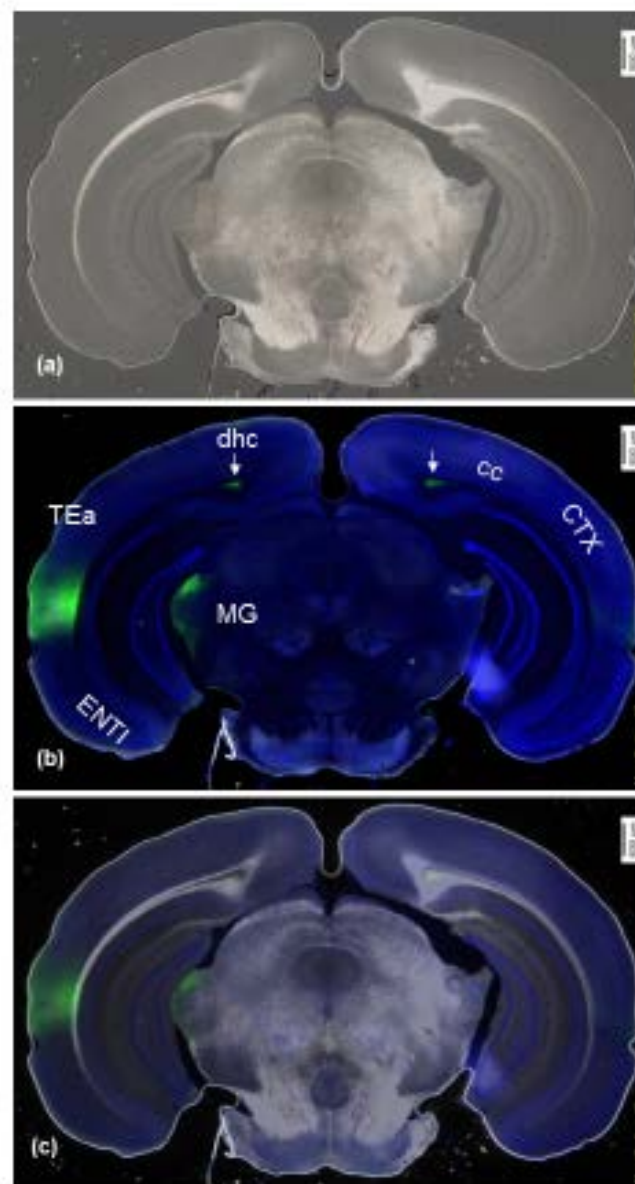
Fig. 3-4   Images of Phaseolus vulgaris leucoagglutinin (PHAL)-labeled neuronal pathways (green areas). Figure courtesy of Kawano et al. (2013).

(3-4a) Darkfield DIRI image collected using a 20× objective lens.

(3-4b) Fluorescence of PHAL-labeled neuronal pathways in green with DAPI stained features in blue (shown in Fig. 3-4b) collected using a 10× objective lens.

(3-4c) Composite image of Fig. 3-4a and 3-4b providing improved clarity of localization of PHAL-labeled neuronal pathways. (i.e., medial geniculate complex, MG) and white matter (i.e., dorsal hippocampal commissure, dhc). DIRI also enhances the appearance of white matter

_____

through which PHAL-labeled axons travel (indicated by arrows).
Abbrevations include cc: corpus callosum; CTX: cerebral cortex; dhc:
dorsal hippocampal commissure; ENTl: lateral part of entorhinal cortex;
MG: medial geniculate complex; TEa: temporal association areas.

b. DIRI using color LEDs

Observation of TMA IHC sample using color illumination

We expected that the color LEDs could be used for selected specific wavelength illumination
and to correct the illumination color. Fig. 3-5 shows the TMA sample illuminated by (a) red,
(b) green, (c) blue, and (d) magenta (obtained by illuminating simultaneously with red and
blue) light. We also illuminated the TMA sample using the maximum possible illumination
intensity (e), *i.e.*, red intensity 225, green 225, and blue 225, which appears close to blue in
color. Fig. 3-5 (f) shows the resulting image from illumination with red intensity 150, green
225, and blue 100. The color in the image looked more natural as we reduced the intensity
of red and blue light (Fig. 3-5 (f)). The three-color LEDs clearly correct the color balance of
DIRI illumination. DIRI uses white LEDs cannot provide the capability for color balance
change.

_____
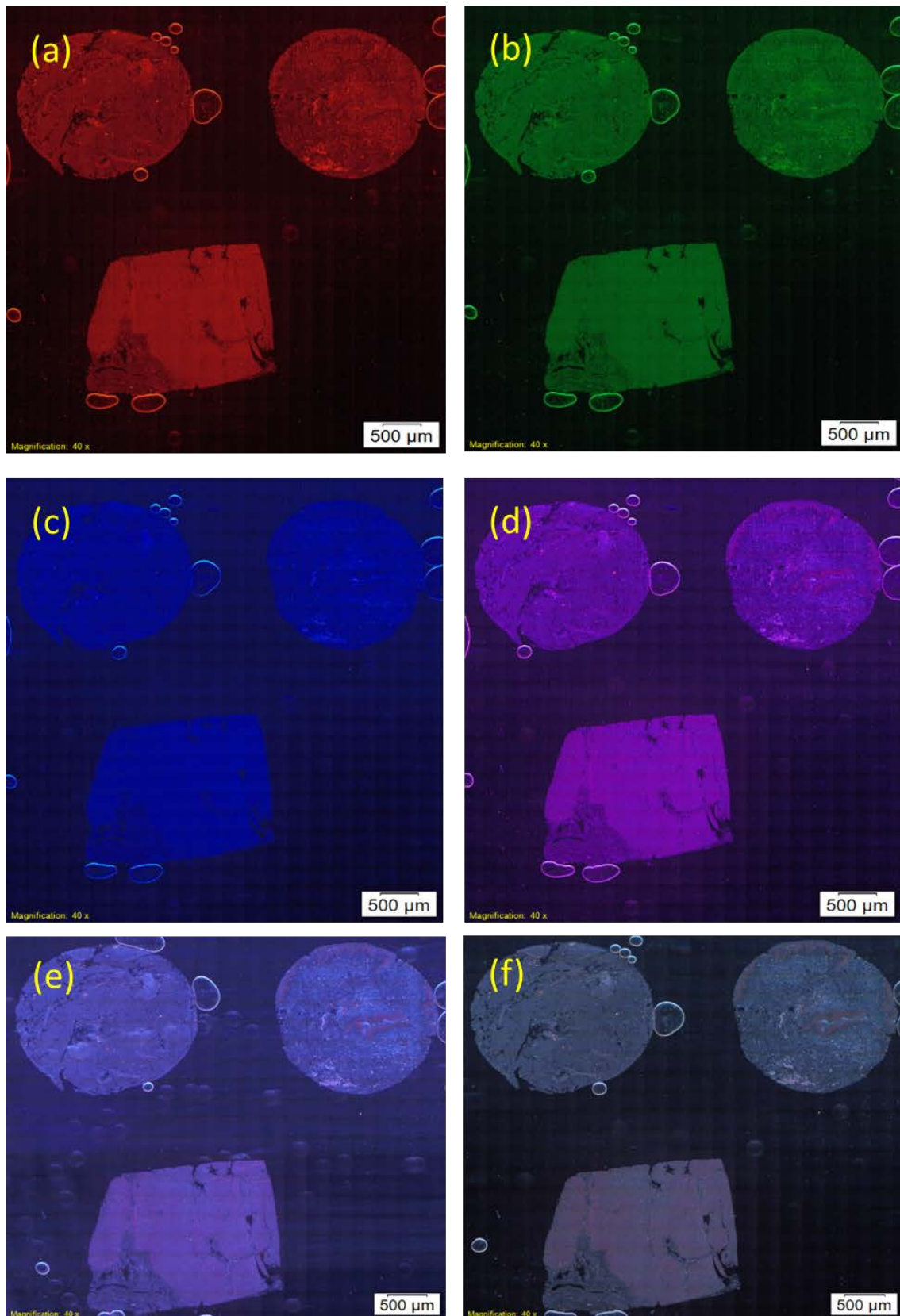
Fig. 3-5   Color images of tissue microarray (TMA) sample. (a)
Illuminated by red, (b) green, (c) blue, (d) magenta, and (e) red 225,

_____

green 225, blue 225, and (f) red 150, green 225, blue 100. All images were captured using a color camera.

Three-color-LED DIRI provides DIRI illumination color adjustment capability.

Observation of DAB-stained brain slice

We expected that color DIRI would be helpful for observing specimen structure. Fig. 3-6 (b) shows a DAB-stained brain slice sample using three-color LEDs. Light intensity was set at red 150, green 225, and blue 100. We also observed a sample using brightfield illumination, as shown in Fig. 3-6 (a). The DIRI image shows the structure of the corpus callosum, whereas the brightfield image does not.

_____
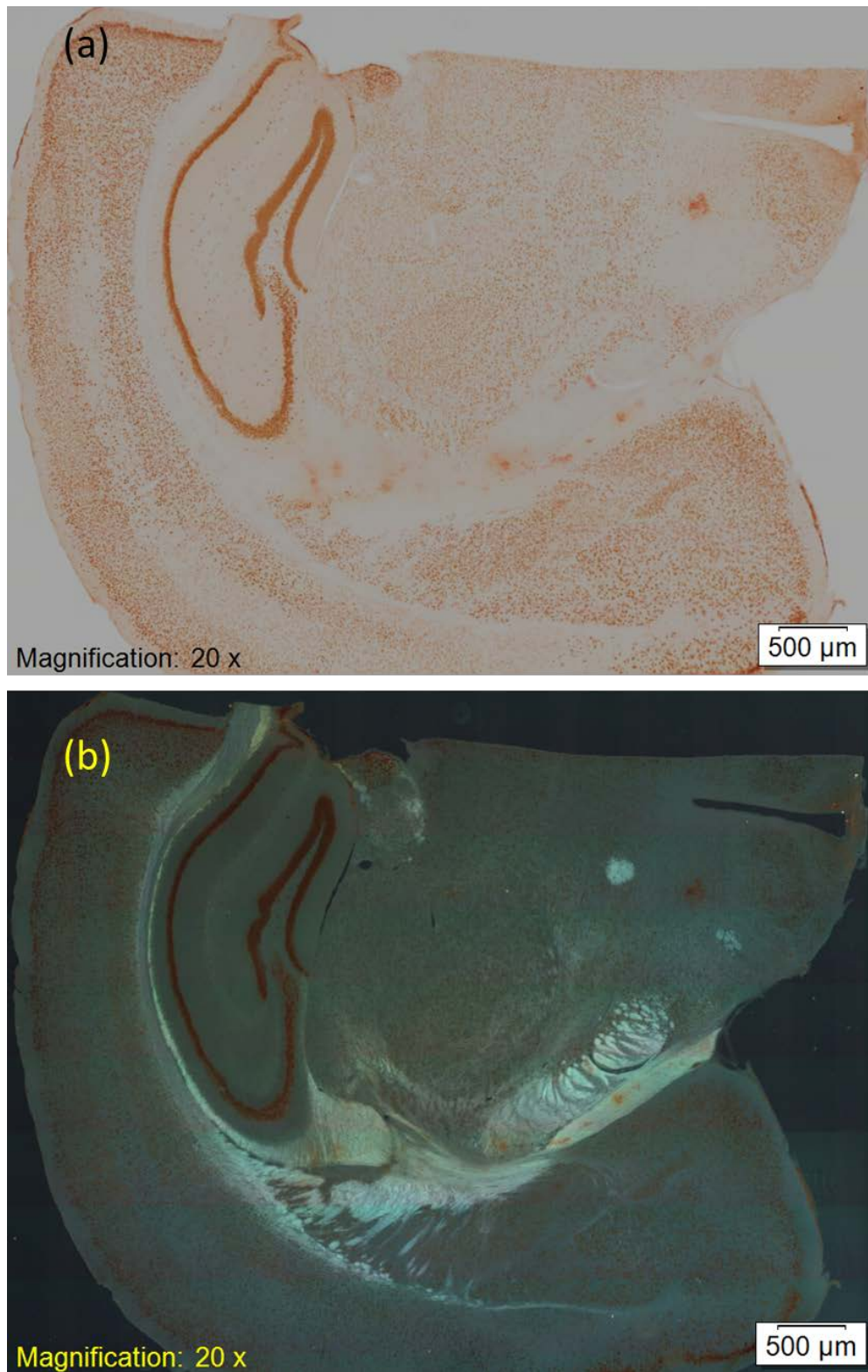
Fig. 3-6   Diaminobenzidine (DAB)-stained brain slices. (a) Brightfield image. (b) Color DIRI image with red 150, green 225, and blue 100. Both images were taken using a color camera.

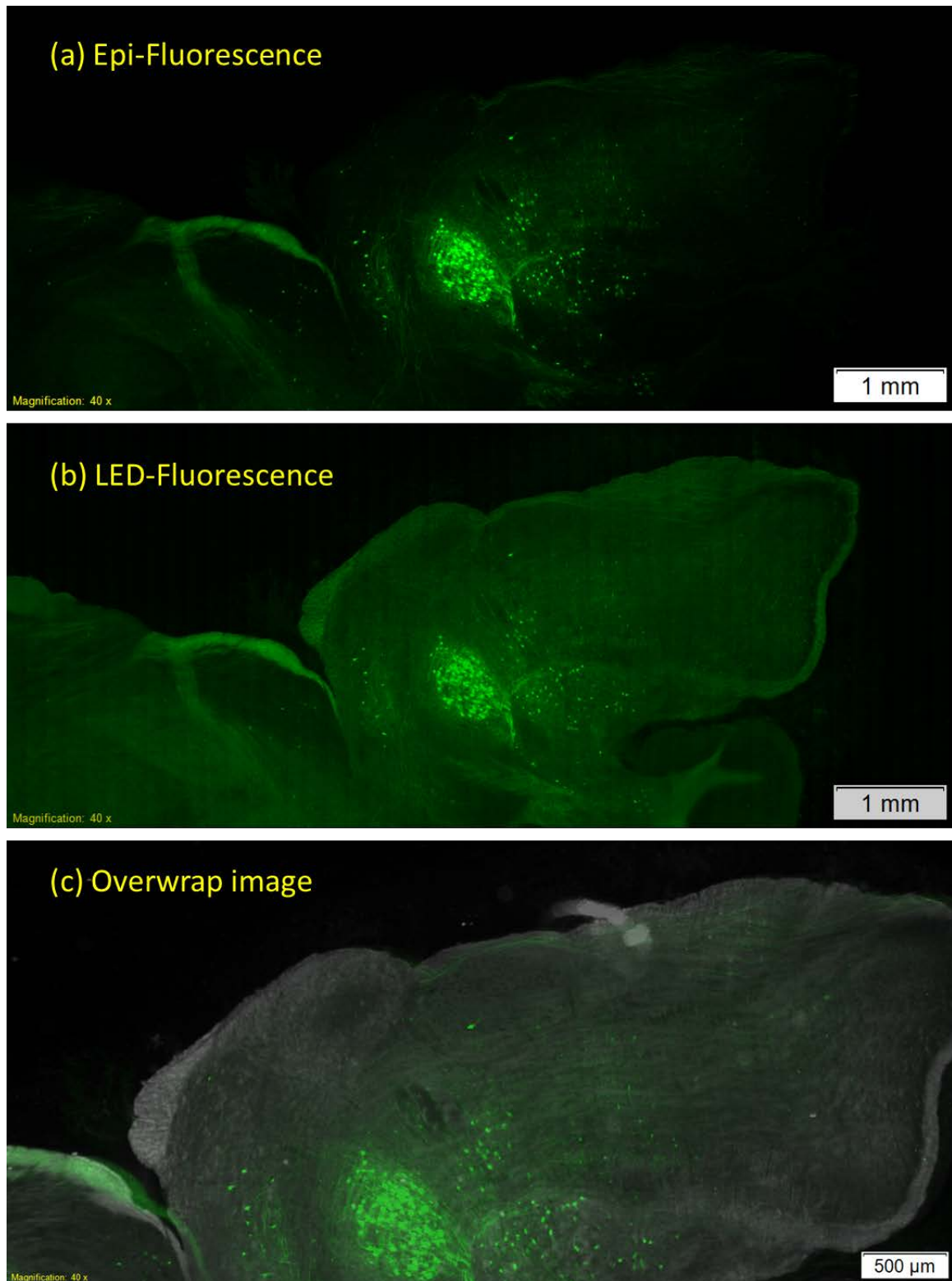Three-color-LED DIRI provides DIRI imaging capability with the color camera.

_____

Brain slice observed by macro DIRI and 40× dry fluorescence image

Next we examined the effectiveness of DIRI for imaging samples without color staining. Fig. 3-7 shows an unstained brain section imaged using DIRI. We obtained a large image of the brain slice using a 2× objective lens with brightfield illumination (Fig. 3-7 (a)). The image contrast is very low, and it is difficult to see the structures in the sample. Then, we switched to three-color DIRI to observe the same brain slice, as shown in Fig. 3-7 (b, c). The DIRI image has high contrast. Switching to epi-fluorescence mode using a 40× dry objective lens also produced a clear image, as shown in Fig. 3-7 (d).
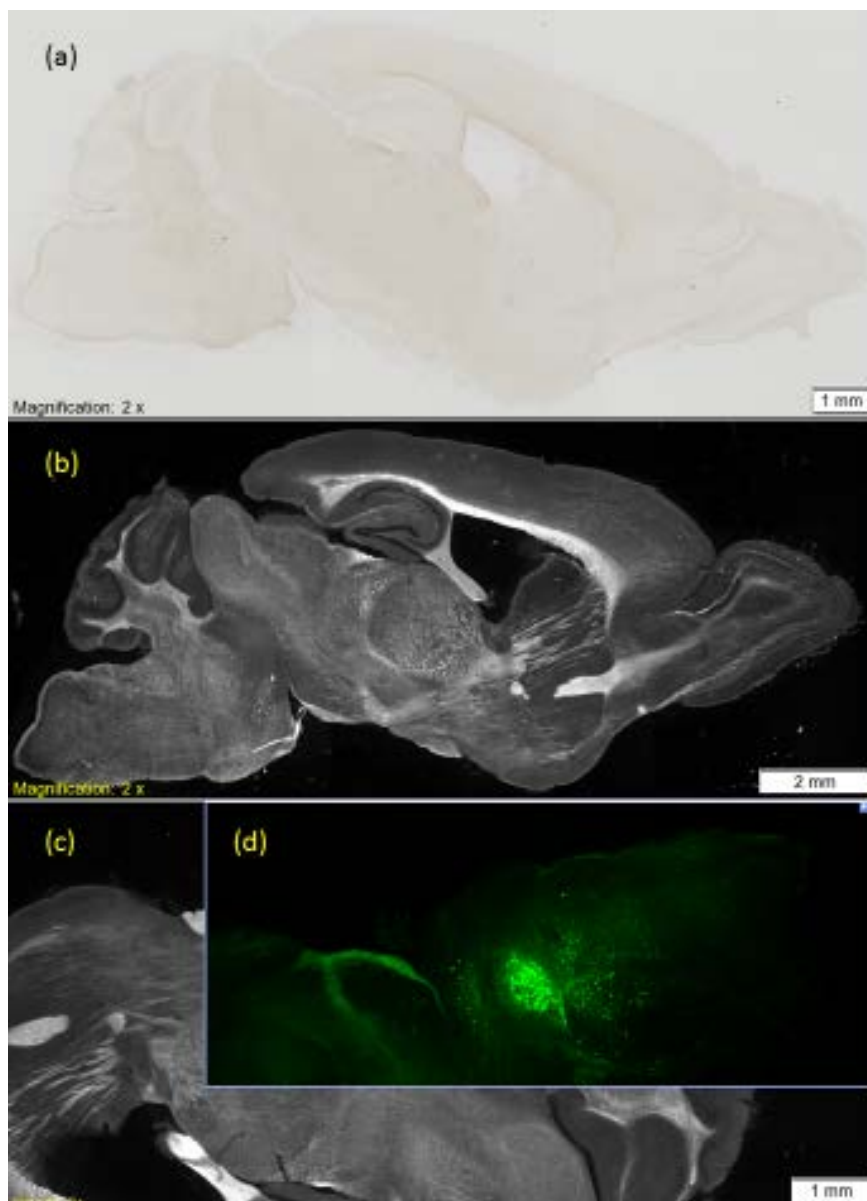
Fig. 3-7 Macro images of a brain slice. (a) Brightfield image using Keller illumination. (b, c, d) DIRI images using color LEDs illumination. Images captured using a black-and-white camera.

Next, we examined multi-mode darkfield and fluorescence imaging using the DIRI system with blue-LED excitation illumination (Fig. 3-8). We compared 3-8 (a) an epi-fluorescence image and 3-8 (b) a DIRI-aided blue-LED-excitation-illuminated fluorescence image. The blue LED light of wavelength 530 nm produced a bright background, as this wavelength of light can pass through the emission filter. A tighter notch filter may further improve performance. Since the fluorescence is green, the sample fluorescence images will appear green in the image. Fig. 3-8 (c) is an overwrap image with DIRI and epi-fluorescence (a).

_____

Fig. 3-8 Macro images with epi-fluorescence. (a) Epi-fluorescence image, (b) LED-illuminated fluorescence, and (c) overwrap image of both DIRI and (a).

Three-color-LED DIRI provides DIRI imaging capability as well as fluorescence illumination capability.

_____

(4) Brain slice observed using fluorescence imaging and a 40x silicon immersion lens

Finally, we examined DIRI together with a 40× silicone oil immersion objective lens (UPLSAPO, NA 1.25). As red light is less photobleaching than blue light, the DIRI image taken using the red light (Fig. 3-9 (a)) was clearer. Fig. 3-9 (b) shows an image taken with blue-LED-illuminated fluorescence. The photobleaching reduces the intensity of fluorescence. Ideally, using longer wavelengths of light may help protect the sample from light damage. We also took an epi-fluorescence image 3-9 (c) and a macro DIRI image 3-9 (d). Without changing the setup of the DIRI illumination system, we just switched to fluorescence illumination. Even using the oil immersion objective lens, we could easily observe fluorescence. This is helpful for the automating the microscope.

_____
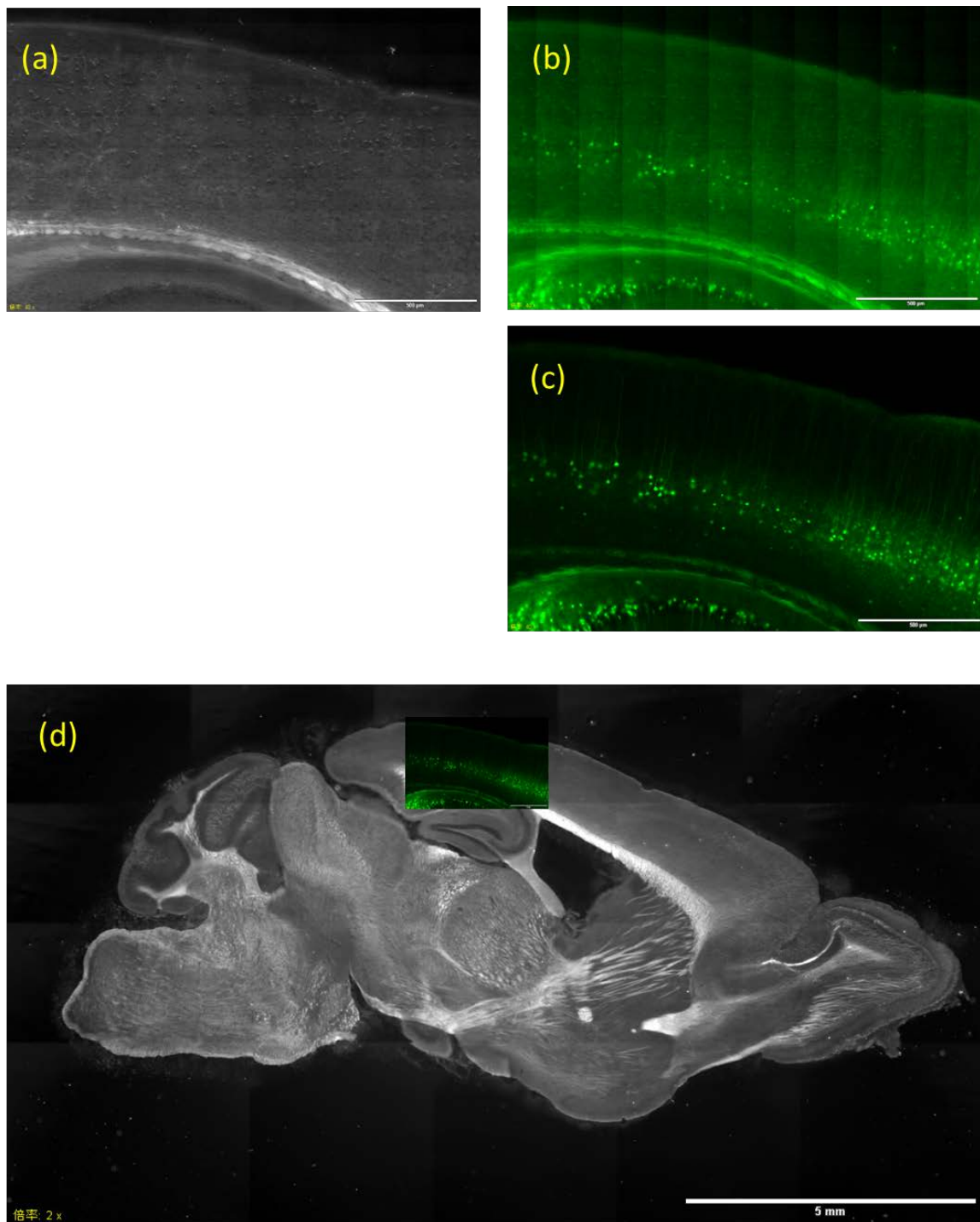
Fig. 3-9   Fluorescence images of a brain slice

 (a) DIRI image with red illumination, (b) blue-illuminated fluorescence DIRI image, (c) epi-illumination, and (d) DIRI image with epi-fluorescence. The objective lens used to take these images was the UPLSAPO 40× silicon immersion lens, with NA = 1.25.

_____

3.1.2 Conclusions for section 3.1

Our experiments indicate that the DIRI system has four main advantages over traditional darkfield:

1) No oil condenser is required for high-resolution imaging,
2) There is less scatter from dust and dirt on the slide specimen,
3) There is less halo, providing a more natural darkfield contrast image, and
4) A motorized system such as WSI systems can produce darkfield, brightfield and fluorescence images.

In addition, we investigated the applicability of three-color LEDs for DIRI illumination. This type of DIRI system offers the following advantages:

1) Color balance adjustment is simple. The color balance of the resulting images can be adjusted by pre-adjusting DIRI color.
2) Major anatomical details can be resolved with DIRI. Illuminating the DAB-stained mid-sagittal brain slice with DIRI enabled a clear image of the corpus callosum structure.
3) Blue DIRI provides fluorescence excitation. We clearly observed YFP in the associated images.
4) Darkfield imaging using high-magnification objective lenses, such as 20× dry and 40× oil, are facilitated by DIRI.
5) Potentially less sample damage occurs with red DIRI illumination.

Therefore, imaging for biological purposes can be facilitated by the use of WSI combined with LED DIRI.

Observing DAB stain samples

The extension of WSI to include darkfield imaging has great potential to expand the prospects for observation of minimally stained brain tissue using light microscopes. Future development of side illumination with brighter LEDs, combined with more sensitive detectors, should provide greatly reduced exposure times and improved signal-to-noise ratios.

Expansion to other applications

Our testing was limited to brain samples, but the WSI system may have utility beyond neuroscience research. We believe a WSI system may be helpful for observing a wide variety of cell and organ types, and indeed for observing almost any microscope slide sample that must be observed at high resolution. Additional applications include cancer research, urology, and translational research, among numerous other fields.

Limitations

There are both advantages and disadvantages in using transmitted darkfield versus side-illumination darkfield. The transmitted darkfield illuminator provides high contrast and very

_____

bright darkfield images. But, the image produces a halo with a very bright edge surrounding the cell image. Furthermore, the substage condenser is limited in its NA and must be changed every time the objective is changed. Darkfield condensers used with objectives that have NAs higher than 0.9 require oil immersion condenser. In comparison, side-illumination darkfield works well with a wide range of objectives with markedly varying NAs.

Furthermore, dirt on the top or bottom of the slide may cause substantial light scattering and disrupt the quality of the image when using a traditional darkfield condenser; side-illumination darkfield is less sensitive to small particles that may settle on the slide or coverglass.

Exposure time is always an issue for WSI. The brightness of the illumination depends on the intensity of the LED, and the availability of brighter LEDs will further reduce total acquisition time for DIRI systems.

Illumination field

Using the described setup, side-illuminated darkfield works well at 10×, 20× and 40× magnifications and may work with other higher-magnification objective lenses. However, with lower-magnification lenses such as the 2× and 4x objective lens, not always but, some case LED illumination light reflects the edge of the slide glass and scatters light. This scattered light gets into the objective lens and may produce so-called image ghosting. This edge reflection also can reduce image contrast in cases where the specimen is close to the edge of the slide.

Brightness of scattering light

Darkfield uses scattered light from both tissues/cells and the mounting medium to help visualize the structure. The light-scatter intensity is dependent on the refractive index of the mounting medium and cell-tissue fixation protocol. If the refractive index difference is small, then the intensity of scattered light will be decreased, thus increasing exposure times.

Color image acquisition

a. DIRI using White LEDs

Collecting color images requires careful calibration of white balance. Traditional substage condensers typically use halogen light with a broad spectral output. Side-illuminated darkfield using the white LED device that is described herein provides a more limited spectral output. The spectral output of white LEDs should be selected with attention to the spectral properties of the DAB-reaction product, which is largely in the yellow-to-red color range. However, three-color-LED DIRI can control individual LED output. So, color balance is no longer an issue for DIRI.

_____

b. DIRI using color LEDs

Three-color-LED illumination allows the researcher to change illumination color balance so that color correction is no longer an issue.

_____

3.2 Microfluidics observation by DIRI

Section 3.2 explains experimental results when using DIRI for microfluidics observation. These include the combination of brightfield and DIRI imaging, the combination of fluorescence and DIRI imaging, and the combination of multiple-fluorescence imaging and DIRI imaging.

3.2.1 Results and discussion

Combination of brightfield and DIRI imaging

When using a microfluidic device, air bubbles may adhere to the inside of the microchannel, and thus make flow control difficult. Microbubbles are small in size and difficult to find across the entire microfluidic device, so developing a methodology to detect microbubbles throughout the device is important. In addition, microbubbles are difficult to detect using standard brightfield illumination because both the bubble signal and the background signal produce images of similar brightness with minimal contrast. In most cases, both liquid and air bubbles are transparent, only differing in refractive index. Darkfield illumination, however, allows the microbubbles to be detected because of the image contrast created by the refractive index difference. Under darkfield illumination, microbubbles appear as bright objects against a dark background. Here, we investigated the utility of our DIRI system for detecting microbubbles.

Clogging is a frequent cause of problems during microfluidics experimentation. Fig. 3-10 shows a DIRI image of an entire microfluidic device, in which air bubbles were observed as bright spots, as indicated by the yellow arrow. The four large bright circles indicated by the blue arrows are the inlets and outlets. VS-ASW software was used to construct a whole-slide image by stitching 1088 individually acquired images. Our system facilitated detection of bubbles in the entire microfluidic device with high contrast. This function helps to check for clogging in the microfluidics system.

_____
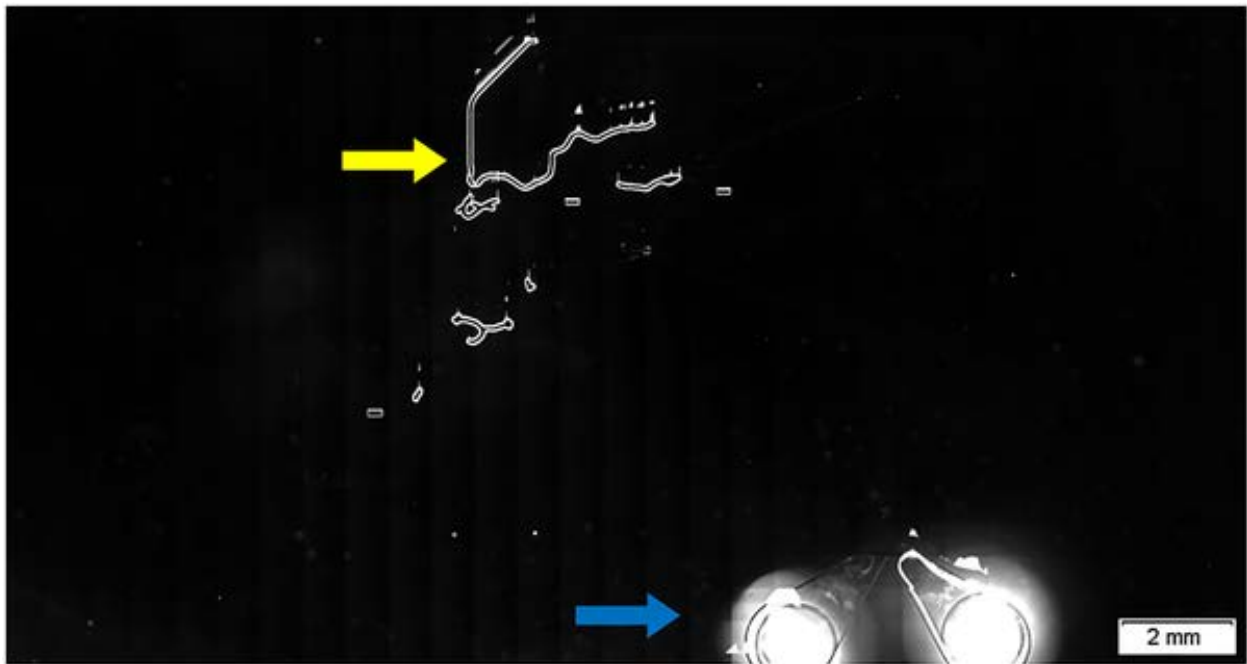
Fig. 3-10   DIRI image of bubbles trapped in the microfluidic channels.

An entire microfluidic device, showing bubbles trapped in the microfluidic
channels. Bubbles are indicated by the yellow arrows. Blue arrows indicate inlet
and outlet ports. The photograph was taken using DIRI with WSI. (Kawano et al.
(2015)).

Sometimes observing the edge of a micro channel is not easy. To clarify the advantages of
the system, we compared microbubble images using brightfield illumination alone (Fig. 3-
11a), simultaneous DIRI and brightfield illumination (Fig. 3-11b), and DIRI alone (Fig. 3-11c).
The images were obtained with a 2× objective lens (NA 0.08), and no flow was induced (i.e.,
the bubbles were stationary). The brightfield image (Fig. 3-11a) shows the darker edge of
the channel and bubbles on top of a brighter background. However, the DIRI image (Fig. 3-
11c) shows the bright edge of the bubbles on a darker background, although the edge of the
channel is unclear. This bright edge of the bubble image is produced by total reflected light
from the LEDs of the DIRI. When DIRI and brightfield illumination were used simultaneously
(Fig. 3-11b), the edges of both the channel and bubbles themselves could be observed
clearly.

(d) **Line Intensity Profile**
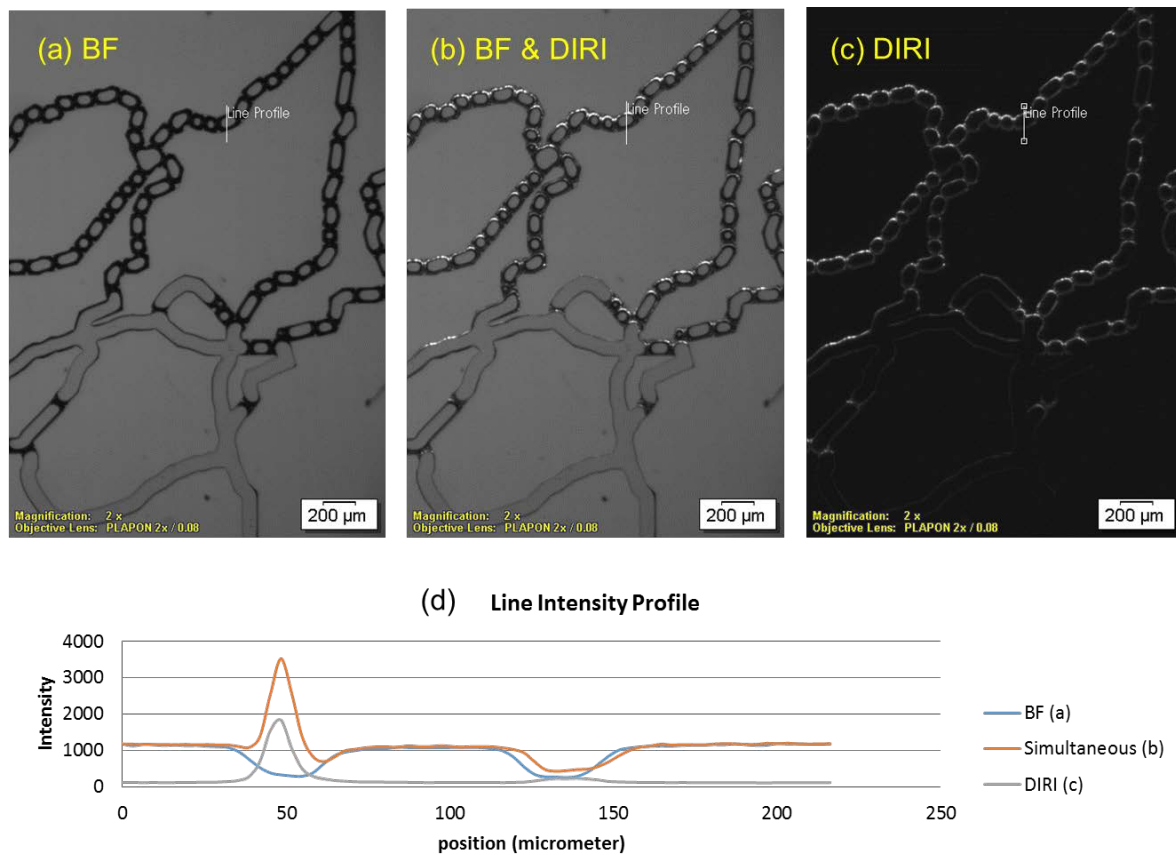
Fig. 3-11   Photographs of bubbles in a microfluidics system captured using brightfield and DIRI. (Kawano et al. (2015)).

This image was acquired using a 2× objective lens (NA 0.08) and an exposure time of 10 ms.

(3-11a) Image captured using brightfield illumination.

(3-11b) Image captured using simultaneous brightfield illumination and DIRI.

(3-11c) Image captured using DIRI alone.

(2-11d) Line intensity profile for 2-11a, b, c.

To quantify the changes in edge detection sensitivity when using different types of illumination, we measured the intensity profile along a line crossing a bubble and the channel walls, as shown in Fig. 3-11d. The measured line is indicated as a white line in Fig. 3-11a-c, which has a length of about 220 µm. In this figure, the intensity varies from 0 to 65535, given that the camera acquired a 16-bit image. As can be seen in the figure, the curve of the line (labeled "Simultaneous") from the simultaneous illuminated image (Fig. 3-11b) shows the greatest variation in brightness at the channel wall and the bubble surface, indicating that the dual-illumination technique of brightfield with DIRI is advantageous for simultaneous detection of bubbles and channel edges.

Next, we induced fluid flow, to put the bubbles in motion. Although the local velocity fluctuated due to breakup and coalescing of bubbles, the velocity of bubbles in the observed

_____

region was on the order of about 10 mm/s. Fig. 3-12 shows a comparison of microbubble images using three kinds of illumination. Images were acquired with a 10× objective lens (NA 0.4). Fig. 3-12a and 3-12c were acquired at different exposures, although the velocity of fluid flow remained constant, so the bubble sizes appear different in each image. The brightfield image (Fig. 3-12a) clearly shows the edges of the channel walls and the edges of the bubbles. The DIRI image (Fig. 3-12c) shows total reflected light from the top side at the edges of the bubbles. Note that the edges of the channel walls are difficult to observe. Fig. 3-12b was taken using brightfield illumination and DIRI simultaneously.
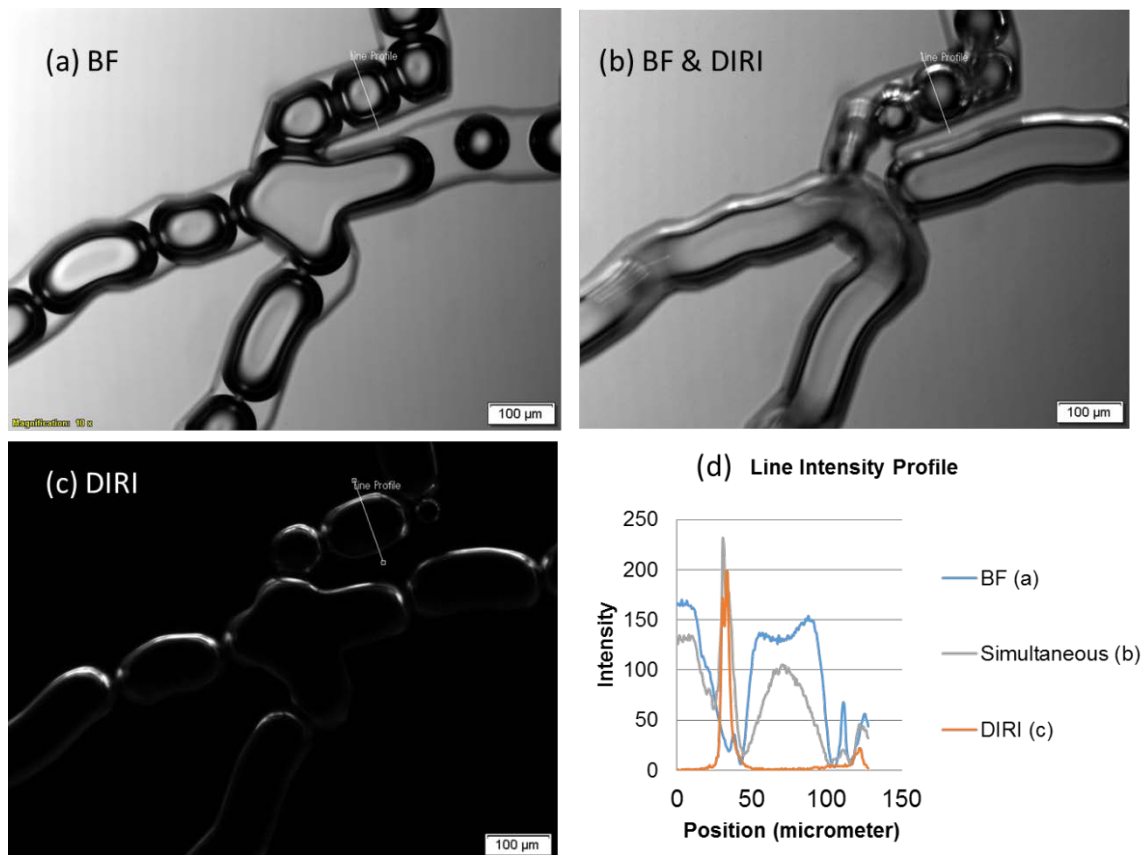
Fig. 3-12   Magnified photographs of bubbles in the microfluidics system using brightfield and DIRI. (Kawano et al. (2015)).

This image was acquired using a 10× objective lens and an exposure time of 60 ms.

(3-12a) Photograph obtained using brightfield illumination alone.

(3-12b) Photograph obtained using simultaneous brightfield illumination and DIRI.

(3-12c) Photograph obtained using DIRI alone.

(3-12d) Line intensity profile for 4-3a-c.

_____

Dynamic observation is very important for micro flow analysis. To quantitatively discuss edge detection sensitivity with different illumination types, we again measured the intensity profile along a line crossing the bubbles and the channel walls. The measured line is indicated as a white line with a length of about 130 µm in Fig. 3-12a-c. In this figure, the intensity ranges from 0 to 255, given that the video-mode camera setup stores 8 bits of intensity depth. Using simultaneous brightfield and DIRI illumination (Fig. 3-12b) provides high contrast at the bubble surfaces as well as the channel wall. This system has the benefit of providing a high-contrast image by simultaneously using two kinds of illumination, rather than requiring the superimposition of two images taken sequentially using the two different kinds of illumination. Therefore, this method can be applied to dynamic phenomena, such as gas-liquid two-phase flow.

Combined fluorescence and DIRI imaging

To assess the applicability of the system to fluorescent illumination, we observed fluorescent beads using DIRI and fluorescent illumination. We first observed the channel wall using DIRI with WSI mode (Fig. 3-13a) using a 10×, NA 0.4 objective lens. The software was programmed to construct a whole-slide image by acquiring and stitching together 108 individually acquired images. Next, we observed the trajectories of fluorescent beads using confocal microscopy in WSI mode. Fig. 3-13b shows the trajectories of fluorescent beads over 0.81 s with a flow rate of 1.2 µL/min. The image was obtained with fluorescent illumination (confocal) alone. Note that the channel walls are difficult to identify. Fig. 3-13c shows superimposed DIRI and fluorescence images that were acquired sequentially. By superimposing the two images, tracer trajectories and channel geometry can be observed clearly. The long trajectories (visible as long green streaks) indicate beads are moving at high velocity, whereas short trajectories (shorter green streaks) indicate low bead velocity. Locations that appear to have many lines indicate those with many moving beads.

There are several advantages to this imaging technique: 1) the superimposed image provides information on the flow field throughout the microfluidic device, making measurements possible using channel architecture as fiduciary points; 2) this imaging modality does not require an expensive camera, such as those used frequently in high-speed imaging; and 3) high quality images can be obtained with a regular cooled-CCD or sCMOS camera designed for fluorescence imaging.
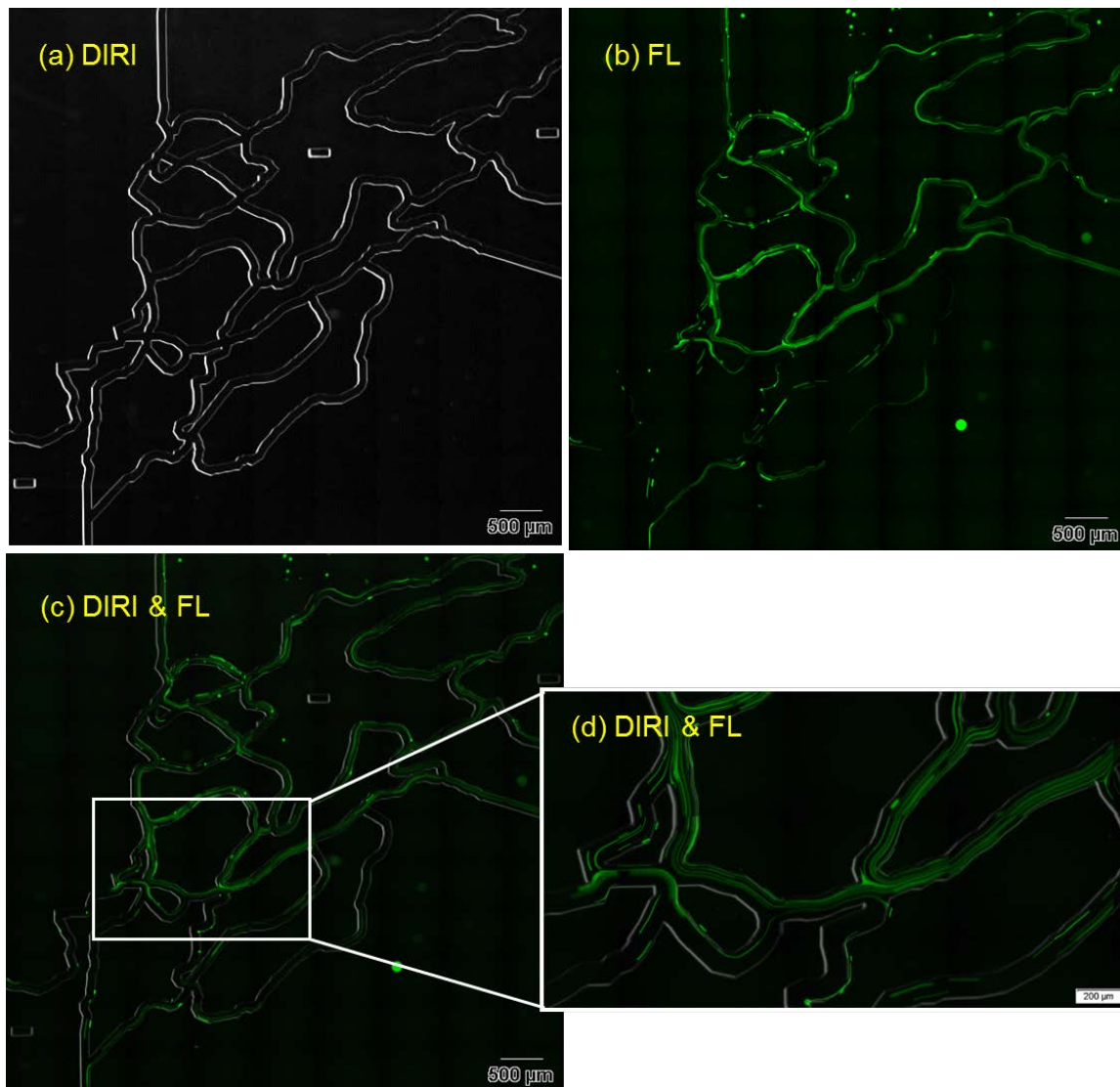
Fig. 3-13 Photographs of fluorescent particles in the entire microfluidic channel. (Kawano et al. (2015)).

The exposure time for darkfield was 100 ms, and that for confocal fluorescence was 810 ms. In total, 108 images were captured using a 10× objective lens and were used to construct the WSI.

(3-13a) DIRI image.

(3-13b) Confocal fluorescence image.

(3-13c) Superimposed fluorescence and DIRI images.

(3-13d) Magnified image of 3-13c.

The velocity field in the microfluidic device can be roughly estimated by capturing images with various exposure times, as shown in Fig. 3-14. The exposure times used in these images were 10 ms (Fig. 3-14a), 30 ms (3-14b), 90 ms (3-14c), 269.9 ms (3-14d), 810 ms

_____

(3-14e), and 2.4 s (3-14f). The velocity at each location can be roughly estimated by measuring the length of each bead trajectory and dividing it by the exposure time. This methodology is useful for determining whether the flow field of a microfluidic device is induced as designed.
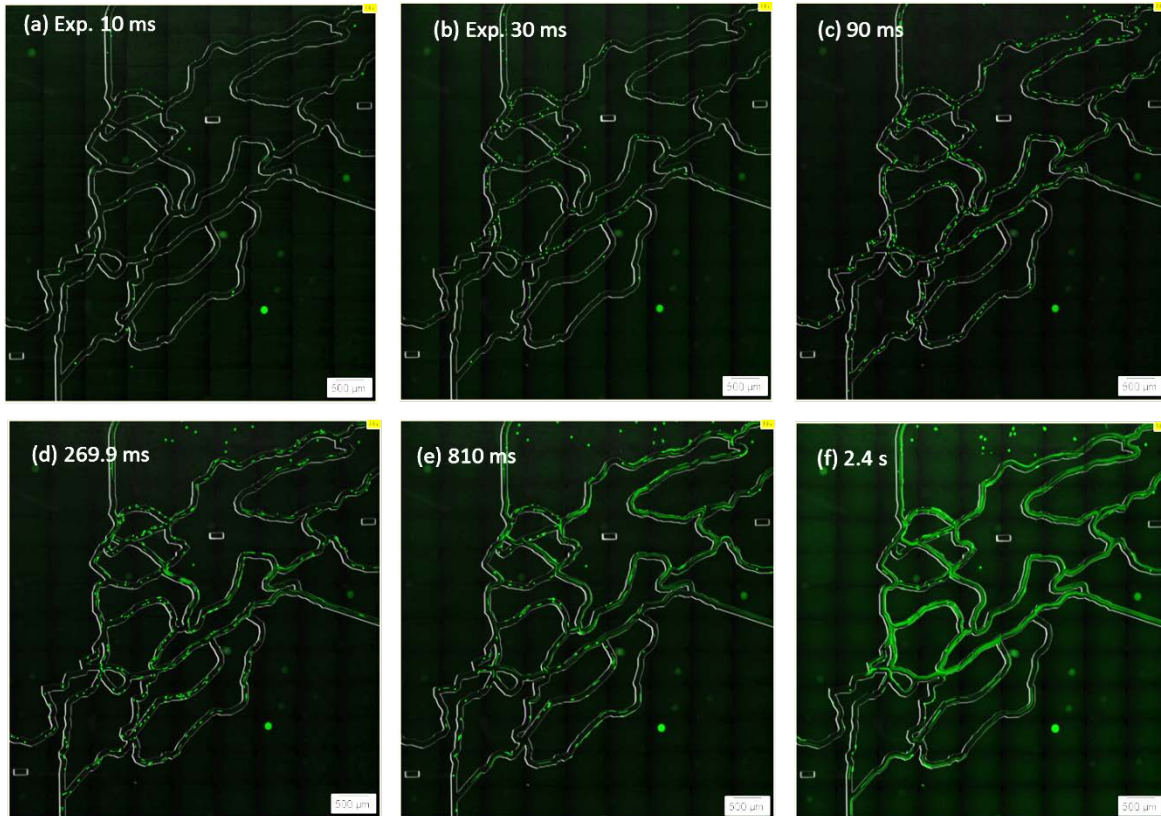
Fig. 3-14   Photographs of exposure time changes for fluorescent particles in the whole microfluidic channel. (Kawano et al. (2015)).

Flow rate 1.2 μL/min. In total, 108 images were captured using a 10× objective lens and were used to construct the WSI (whole-slide image). Images are superimposed the fluorescence and DIRI images.

(3-14a) Exposure time 10 ms.

(3-14b) Exposure time 30 ms.

(3-14c) Exposure time 90 ms.

(3-14d) Exposure time 269.9 ms.

(3-14e) Exposure time 810 ms.

(3-14f) Exposure time 2.4 s.

_____

The images shown in Fig. 3-15 were obtained by simultaneously using DIRI and fluorescent illumination. No flow was induced and the three-dimensional confocal image was obtained using a 30× silicone oil immersion objective lens (NA 1.05). In the case of fluorescent illumination alone (Fig. 3-15a), fluorescent beads could be observed clearly, but the edges of the channel were difficult to identify. When fluorescent and brightfield illumination were used simultaneously (Fig. 3-15c), the shape of the channel became clear, but the contrast of the fluorescent beads was lost because the background image was brighter. The bright background considerably reduced the contrast of the image. When DIRI and fluorescent illumination were used simultaneously (Fig. 3-15b), the shape of the channel could be observed clearly, and the contrast of the fluorescent beads was maintained. This technique can also be applied to dynamic phenomena, such as fluorescent beads flowing through the microchannel.
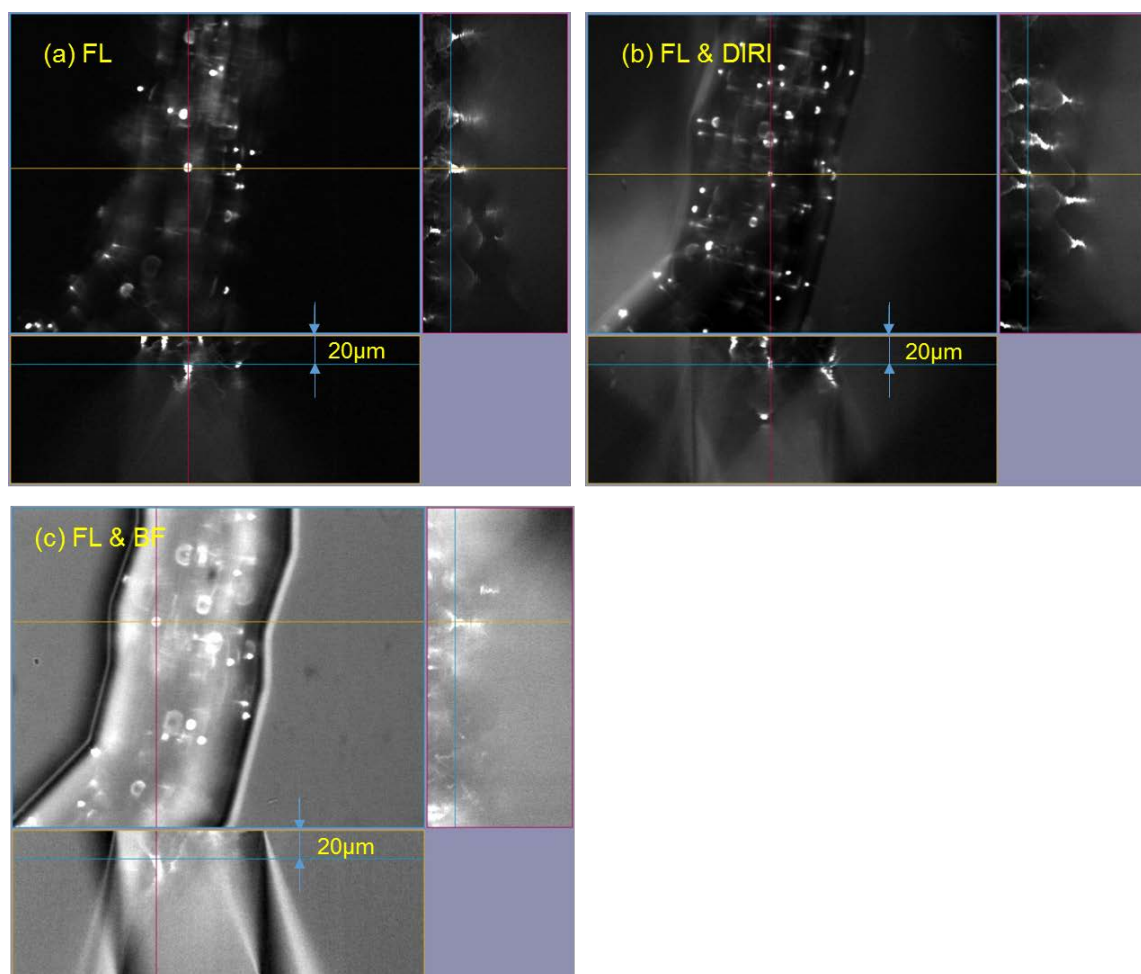
Fig. 3-15   Three-dimensional images of fluorescent particles in microfluidic channels taken using confocal and DIRI. (Kawano et al. (2015)).

The image was taken with a 30× objective lens (NA 1.05, silicone oil immersion).

(3-15a) Confocal fluorescence image.

_____

(3-15b) Image obtained using simultaneous confocal fluorescence excitation and DIRI.

(3-15c) Image obtained using simultaneous confocal fluorescence excitation, and brightfield illumination.

## Combining multiple-fluorescence imaging and DIRI

Finally, we investigated the applicability of the system for imaging cells within microfluidic devices. Endothelial cells (0.5 mL, 6×10^5 cells/mL) were injected into the microfluidic device, followed by incubation for 5 h at 37°C in a 5% CO_2 atmosphere to allow the cells to attach to the walls of the microfluidic channel. Immediately before the experiment, fibrosarcoma cells (HT1080; 0.5 mL, 6×10^5 cells/mL) were injected into the microfluidic device. The endothelial cells were labeled with rhodamine 123, which was visualized in the green fluorescence emission channel, whereas the fibrosarcoma cells were labeled with MitoTracker Red CMXRos for visualization in the red fluorescence emission channel. A superimposed whole-slide image of green fluorescence and red fluorescence images is shown in Fig. 3-16 (20× objective lens, NA 0.75). The system is capable of providing a high-contrast whole-slide image of two fluorescent colors.
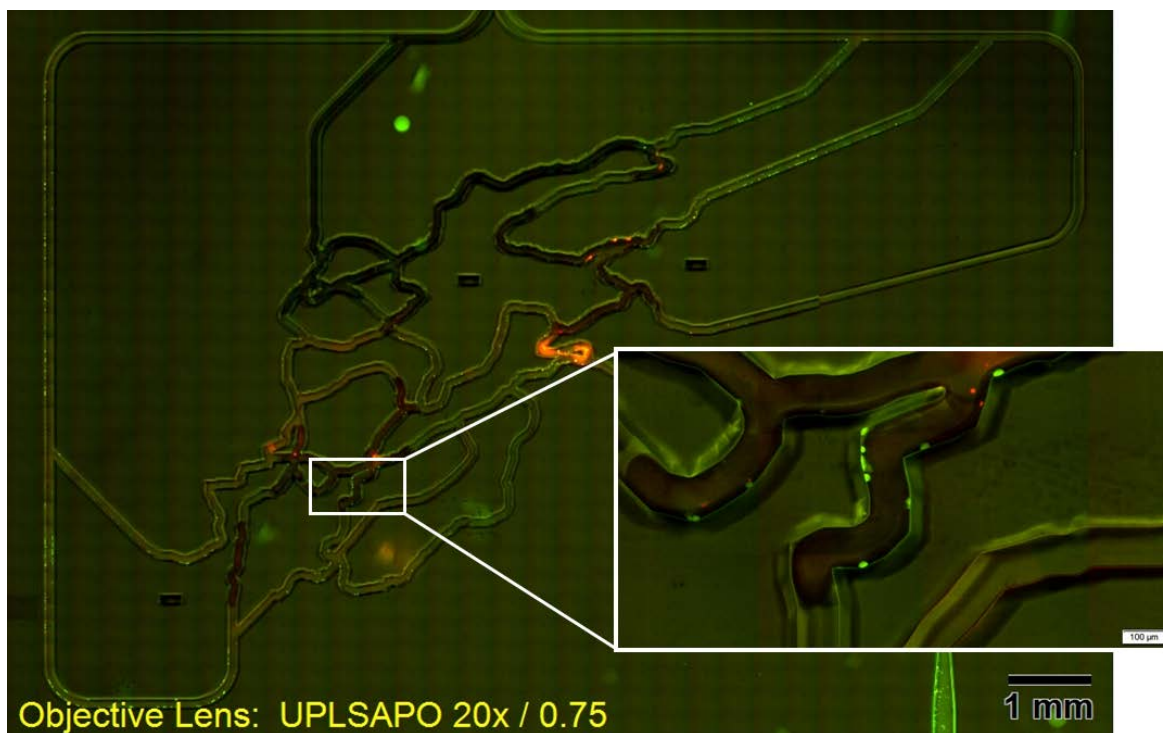
Fig. 3-16 Endothelial and fibrosarcoma cells in the whole microfluidic channel. (Kawano et al. (2015)).

_____

Endothelial cells (emitting green fluorescence) and fibrosarcoma cells (emitting red fluorescence) in the whole microfluidic device. The image was generated by superimposing two fluorescence images captured using a 20× objective lens (NA 0.75).

Fig. 3-17 shows the advantages of multiple-channel fluorescence imaging plus DIRI imaging in certain experiments. These images show a magnified image of two types of stained cells acquired using a 30× silicone oil immersion objective lens (NA 1.05). In the brightfield image (Fig. 3-17a), high contrast can be seen at the edges of the channel walls, and the cells stand out well from the background. However, the difference between endothelial cells (green arrow) and fibrosarcoma cells (red arrow) is not obvious. Use of appropriate fluorescent illumination (Fig. 3-17b) enabled observation of one or the other population of cells, but rendered the walls of the microchannel difficult to see. In this image, the endothelial cells are fluorescing under blue excitation (green arrow) and can be seen clearly, but the edges of the walls and the fibrosarcoma cells were unclear or not visible. Simultaneous observation of the green fluorescence emission and DIRI (Fig. 3-17c) facilitated observation of the endothelial cells (green arrow) and the edge of the channel walls. The high-contrast images were obtained using two types of illumination simultaneously (not by superimposing two independent images in post-processing). Thus, the system is ideal for observing cell adhesion and invasion, in which dynamic interactions between multiple cell types and blood vessel walls can be visualized in a simplified *in vitro* model of a complicated *in vivo* situation.
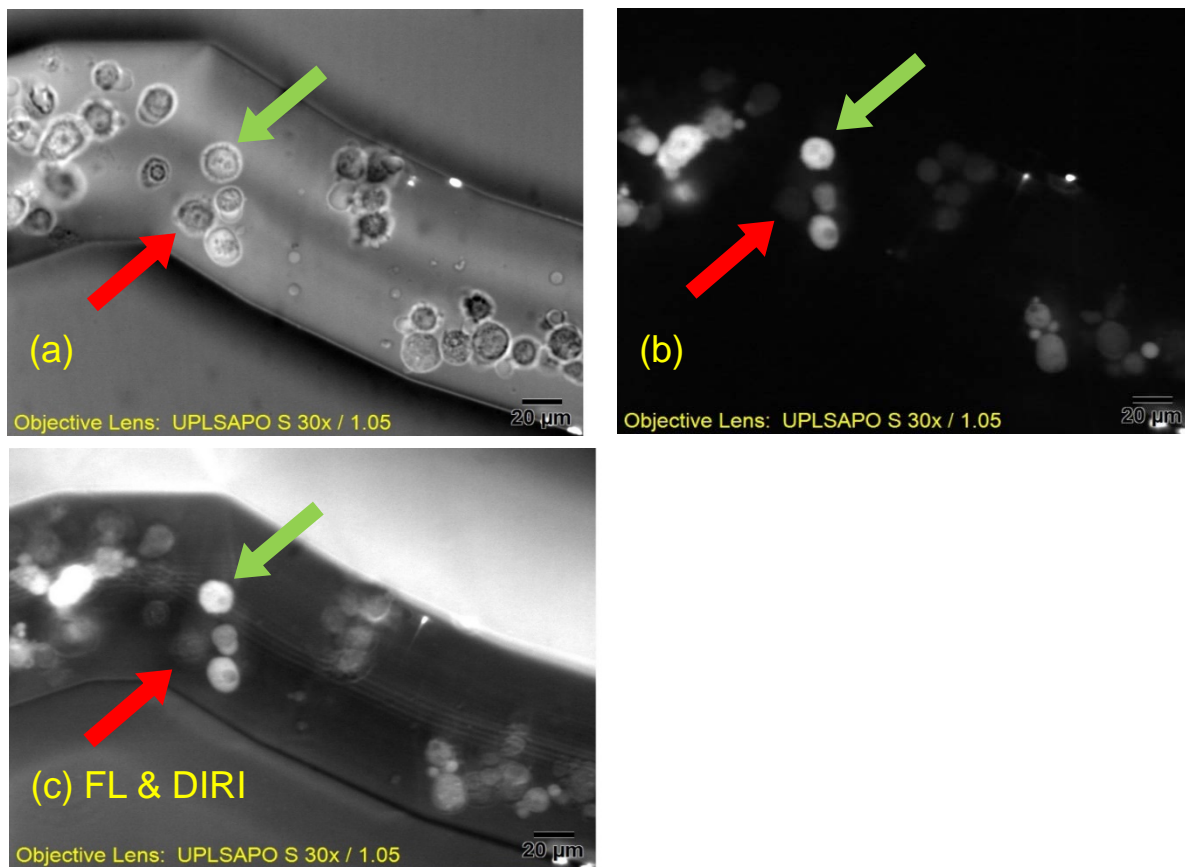
Fig 3-17. Images of cells obtained using three types of illumination.
(Kawano et al. (2015)).

The images were captured using a 30× silicone oil immersion objective lens
(NA 1.05). The green arrow indicates an endothelial cell, and the red arrow a
fibrosarcoma cell. (3-17a) Brightfield image with an exposure time of 250 ms.
(3-17b) Confocal fluorescence image with an exposure time of 200 ms. (3-
17c) Simultaneous confocal fluorescence excitation and DIRI. The exposure
time for fluorescence was 250 ms.

3.2.2 Conclusions for section 3.2

In this study, we investigated the applicability of using DIRI for observing a microfluidic
device containing microbubbles, fluorescent particles, or fluorescently labeled cells. WSI was
combined with these modalities to extend system capabilities and allow multi-modal imaging
of an entire microchannel device. Multi-modal imaging allowed clear visualization of both
microbubbles and channel walls by utilizing DIRI and brightfield illumination simultaneously.
The imaging methodology is useful not only for examination of static phenomena, such as
clogging, but also for observation of dynamic phenomena, such as the detection of bubbles,
fluorescent tracer particles, or labeled cells flowing through a channel.

Observation of these dynamics makes possible a whole range of physical and physiological
measurements of systems used for modeling more complex *in vivo* situations. This new
multi-modal observation technique can facilitate many previously difficult analyses, including
observation of phenomena such as vessel wall adhesion of circulating cells under the
moderation of pharmacological or physical agents, clot formation and inhibition, blood vessel
obstruction, certain chemotaxis studies, the influence of turbulence on vessel walls, the
influence of pharmacological moderators on circulating cell behavior, etc. The system
developed here and the model validated in this study may be useful for a wide variety of
engineering and biomedical applications using microfluidic devices.

_____

3.3 DIRI combined with TIRF microscopy

Section 3.3, explains the experimental results of total internal reflection fluorescence (TIRF) microscopy and DIRI microscopy. We evaluated both 100×NA 1.65 and 60xNA 1.45 objective lenses, along with the fiber-type TIRFM illuminator. We also studied the use of DIRI combined with TIRF.

3.3.1 Results and discussion

Evaluation of 100×/NA 1.65 and 60x/NA 1.45 objective lens

The setup consisted of an inverted microscope equipped with an APO 100x/NA 1.65 objective lens with a projection lens of 2.5x. The light source was a 532 nm 25 mW semiconductor laser (Crysta Laser, USA). The TIRF setup was placed on an optical bench. The laser beam was expanded and then focused on the back focal plane of the objective lens. No fiber illuminator was used. The camera used was a 512 ×512 pixel digital camera (Olympix, USA). On a cover glass, a specimen consisting of 0.2 μm fluorescent beads and cheek cells stained with tetra methyl rhodamine ISO-30 thiocyanate (TRITC) were prepared as the sample (Fig. 3-18).

Image contrast is a key performance factor in microscopic observation. We compared fluorescence and TIRF images (Fig. 3-19). In the fluorescence mode, with the focus on the beads, the bead fluorescence was very difficult to identify due to obscuring background fluorescence from the cheek cells (Fig. 3-19b, FLM). In TIRF imaging mode, image contrast was dramatically increased, and beads could be observed very easily. Only the near field (a few hundred nanometers below the specimen slide cover glass) was excited. The cheek cells were out of reach of the evanescent wave and did not contribute to the fluorescence image Fig. 3-18a).
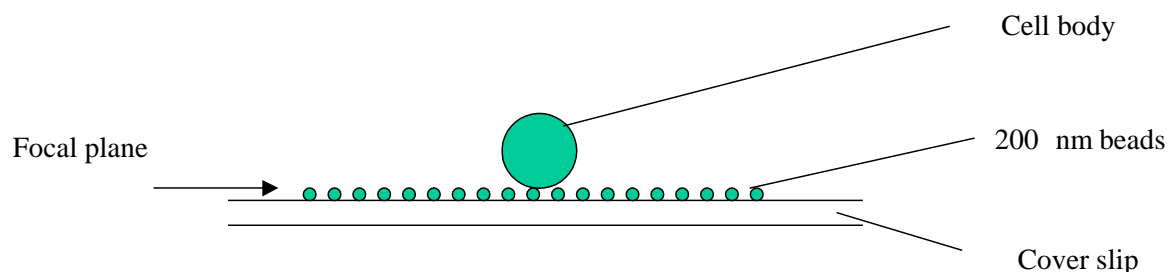
Fig. 3-18   Fluorescent beads (200 nm) with a cheek cell. (Kawano et al. (1999, 2000)).

Cheek cells were stained using TRITC and placed on a coverslip. Then phosphate-buffered saline (PBS) with fluorescent beads (diameter 0.2 μ) was dropped.
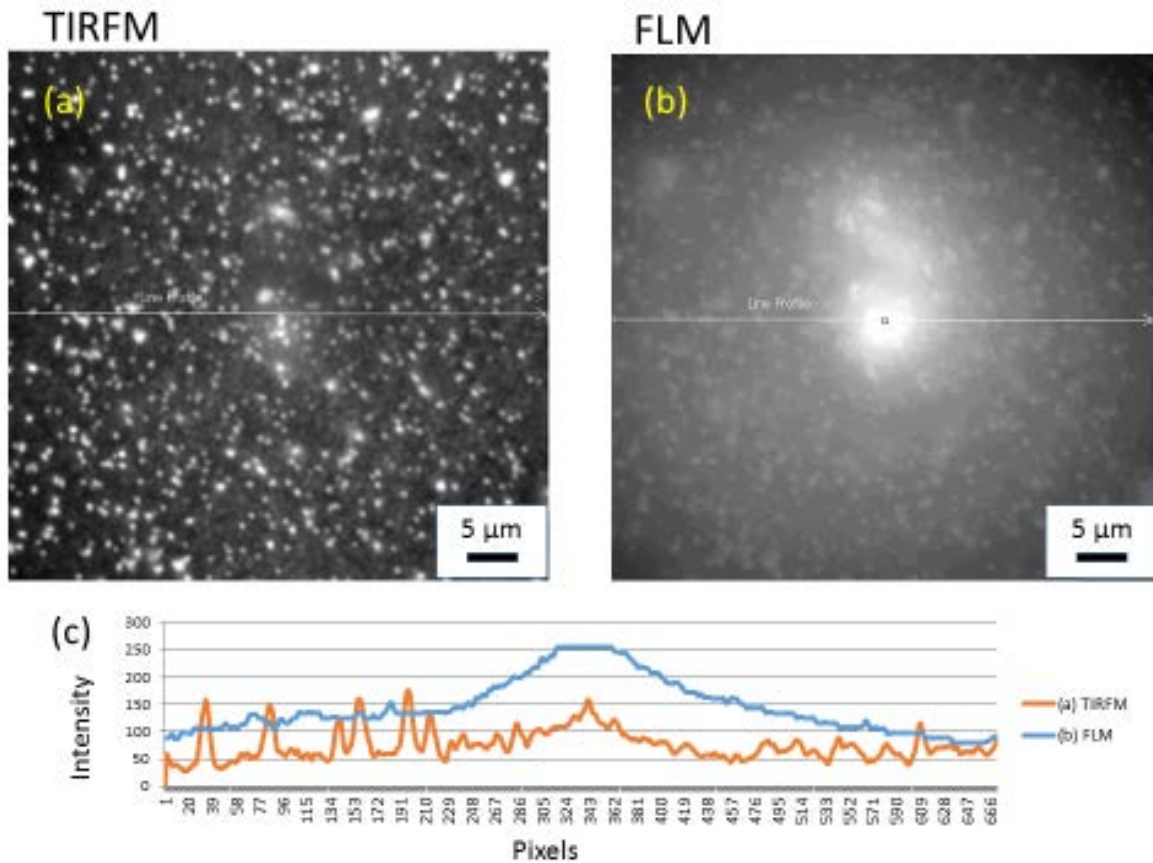
Fig. 3-19 Fluorescent beads (200nm) with a cheek cell observed by evanescent illumination and epi-fluorescence illumination. (Kawano et al. (1999, 2000)).

(3-19a) TIRF microscopy only allows observation of fluorescent beads; it is hard to observe the cell.

(3-19b) In the widefield fluorescence image, not only the surface of the coverslip is illuminated, but the whole sample is illuminated in both the XY (horizontal) and Z (focus) directions. Both fluorescent beads and TRITC-stained cheek cells are illuminated, but the image is foggy. It is difficult see the beads because the background is so bright.

(3-19c) Line intensity profiles for (a) and (b).

A very dilute solution of tetramethyl rhodamine was also observed in the TIRF microscopy mode with the APO 100×/NA 1.65 objective lens and the APO 100x/NA 1.40 objective lens

(Fig. 3-20). An ICCD camera enhanced with an image intensifier (VS4-1845 VideoScope, USA) was used.

Both image intensity and ease of use are very important in microscope-based experimentation. Brighter images help scientists observe weakly stained cells or particles. In this experiment, images of single molecules on the cover glass were captured easily with the higher-NA lens (NA 1.65), but were difficult to capture with the lower-NA lens (NA 1.40), but both lenses allowed clear observation and imaging. In order to obtain the same level of image brightness, it was necessary to increase the laser intensity 5 fold for observation with the NA 1.40 lens. This was achieved by removing a neutral density (ND) filter inserted in the laser beam (532 nm, 100mW, Coherent, USA).
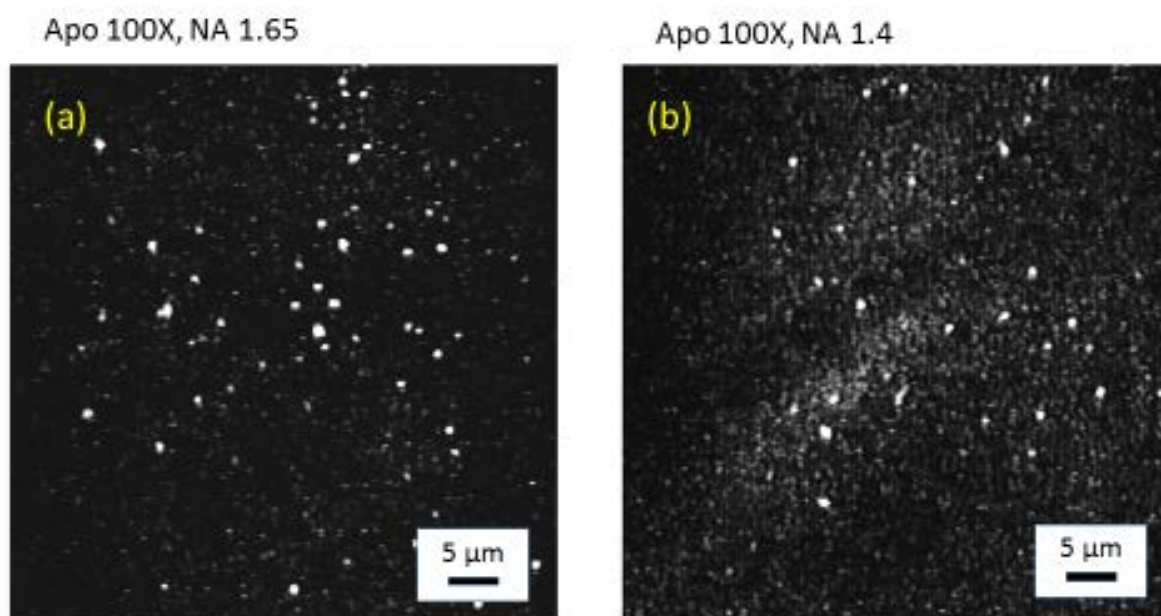
Fig. 3-20   Single-molecule imaging of tetramethyl rhodamine observed with APO 100× NA 1.65 objective lens (a) and APO 100× NA 1.40 objective lens (b). (Kawano et al. (2000)).

All imaging conditions were the same for (a) and (b) except that an ND filter was inserted in the illuminating laser beam for the NA 1.65 observation (a) to reduce the intensity of the evanescent field by a factor of 5.

The setup consisted of an inverted microscope equipped with a Plan APO 60× NA 1.45 objective lens with a projection lens of 2.5× (Fig. 3-21). Otherwise, the laser, illuminator, illumination lenses, and the camera were the same as those described in the previous experiment.
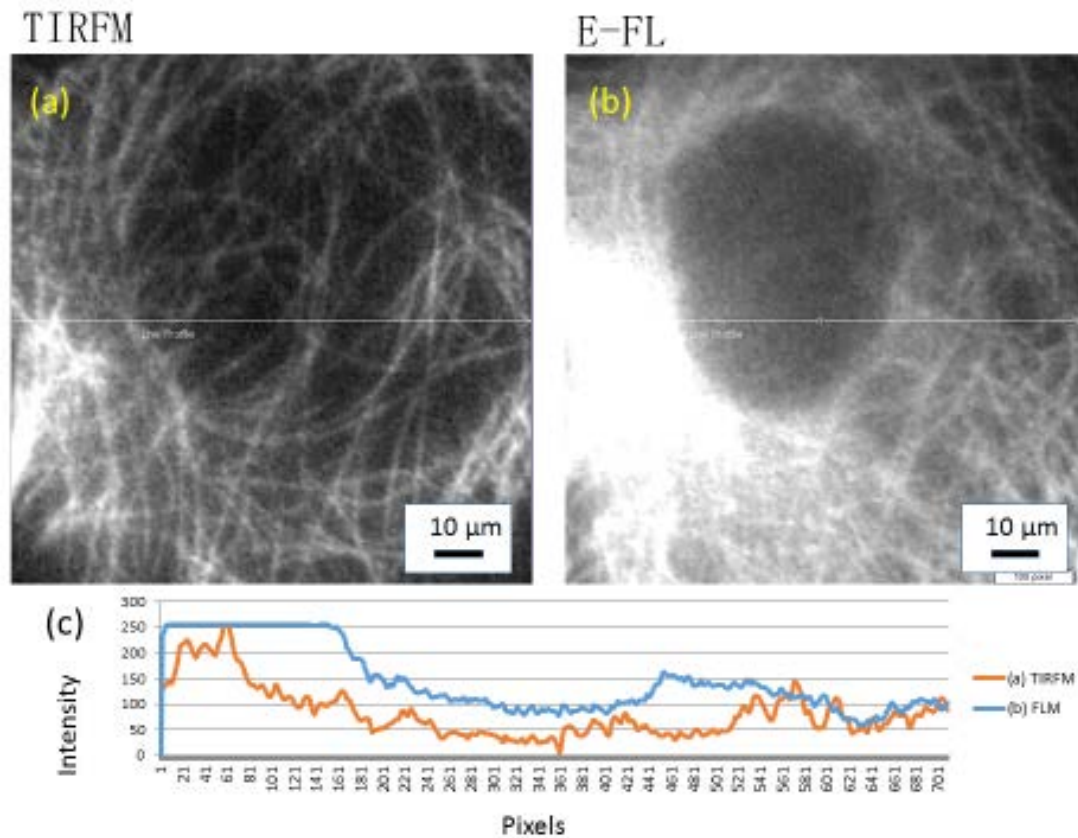
Fig. 3-21 Fluorescent-labeled microtubules of a PtK2 cell observed by TIRF microscopy (a) and by epi-fluorescence microscopy (b). (Kawano et al. (2000)).

Fluorescence illumination was used to illuminate the entire sample, providing the brighter background. TIRFM illumination only reaches the surface of the sample, providing lower background and a higher-contrast image. The line intensity profile is shown at (c).

In cultured PtK2 cells, microtubules were stained with Alexa Fluor 546 and were observed in epi-fluorescence and TIRFM modes.

The epi-fluorescence image displayed very low contrast because all of the microtubules were excited to fluoresce (Fig. 3-21b, FLM). Epi-fluorescence illuminates the entire sample, so microtubules across the entire depth of the sample provided fluorescence.

A high-contrast image of the microtubules near the cell surface can be observed using TIRFM (Fig. 3-21a). Because TIRF illumination reaches just the area nearest the surface, microtubules located further below the surface are not observed when using TIRFM.

_____

Evaluation of a fiber-type TIRFM illuminator

The setup consists of an inverted microscope equipped with an APO 100x, NA 1.65 objective lens and a projection lens of 2.5x. The illuminator was equipped with an optical fiber to introduce the laser light to the microscope (Chapter 2, Fig. 2-17a-b). A laser (532 nm, 50 mW. Uniphase, USA) was used as a light source. A pair of illumination lenses expanded the laser beam and then focused it on the back focal plane of the objective lens (Chapter 2, Fig. 2-16). A SIT-type camera (C2741. Hamamatsu Photonics. Japan) was used.

Actin filaments of cultured NG108-15 cells were stained with Alexa Fluor 568 and the nuclei with propidum iodide (PI). Their fluorescence images were observed compared with the epi-fluorescence mode and the TIRF mode. The epi-fluorescence image had very low contrast because the excitation light illuminates the nucleus to emit fluorescence (Fig. 3-22b). A high-contrast image of the actin filaments was observed using TIRF microscopy (Fig. 3-22a).

We compared setup times using fiber-type and non-fiber-type TIRF microscopes. The setup time was about 15 min for fiber-type TIRF systems. This is shorter setup time than using the non-fiber-type TIRF illuminator.
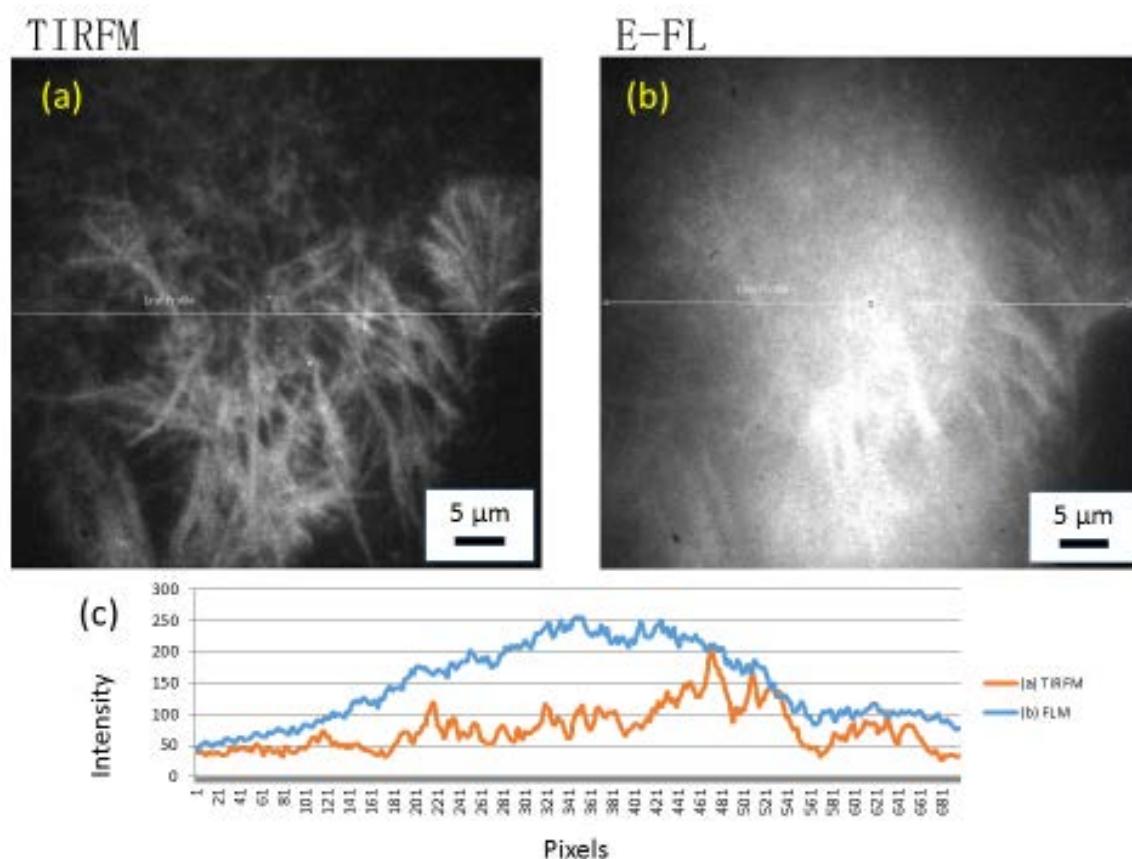
Fig. 3-22   Fluorescently stained actin fibers and a nucleus of an NG108-15 cell observed by TIRFM and by epi-fluorescence microscopy. (Kawano et al. (2000)).

(3-22a) TIRFM image for NG108-15

(3-22b) Epi-fluorescence image for NG108-15

_____

(3-22c) Line intensity profiles for (a) and (b).

DIRI combined with TIRF microscopy

The microscope was set up in widefield fluorescence microscopy mode. Laser illumination was used, with the laser in non-TIRF mode. Samples were illuminated throughout the entire field. It was possible to observe the beads on the surface of the coverslip clearly (Fig. 3-23a). Then the microscope focus position was set up for the middle portion of the channel. The floating beads were still easy to discern (Fig. 3-23b); however, the position of the microfluidics channel side wall was not clearly observed. The arrows at Fig. 3-23c are on the line intensity profile of Figs. 3-22a and b. The arrows denote the edge of the channel side wall.
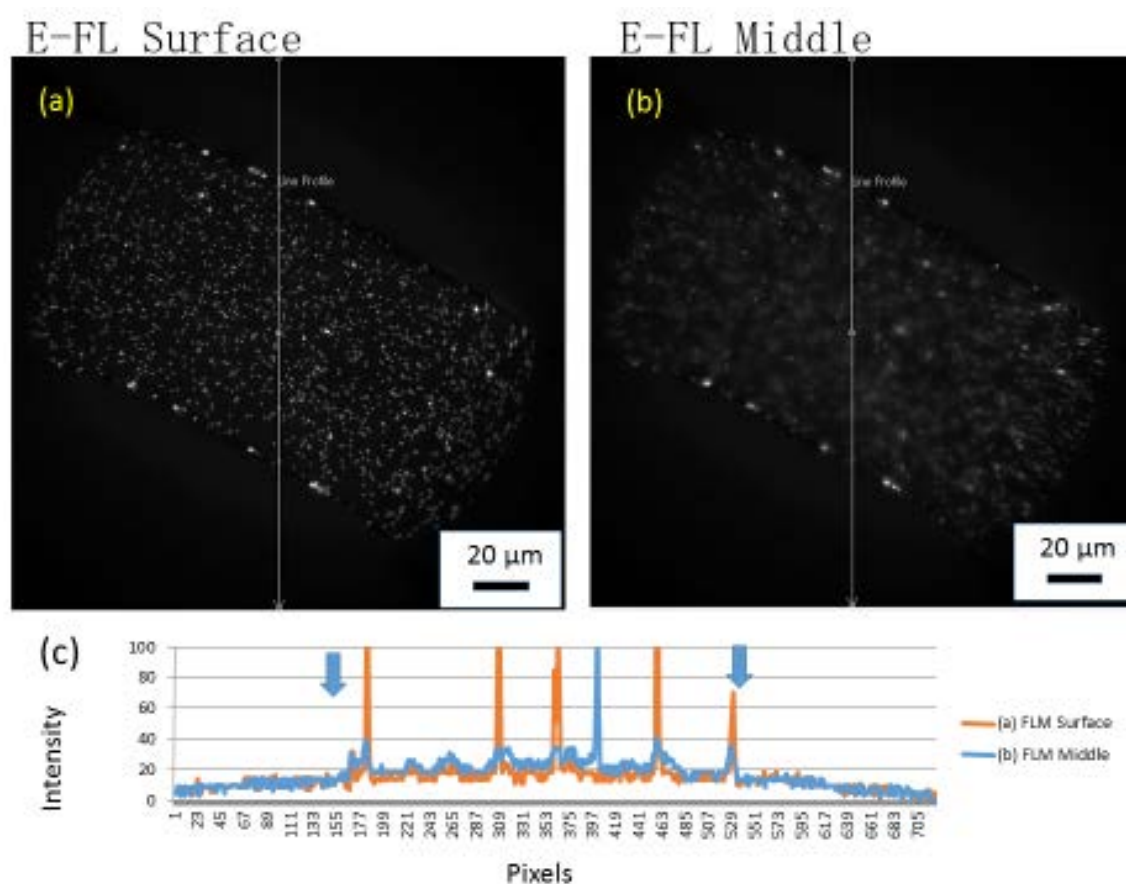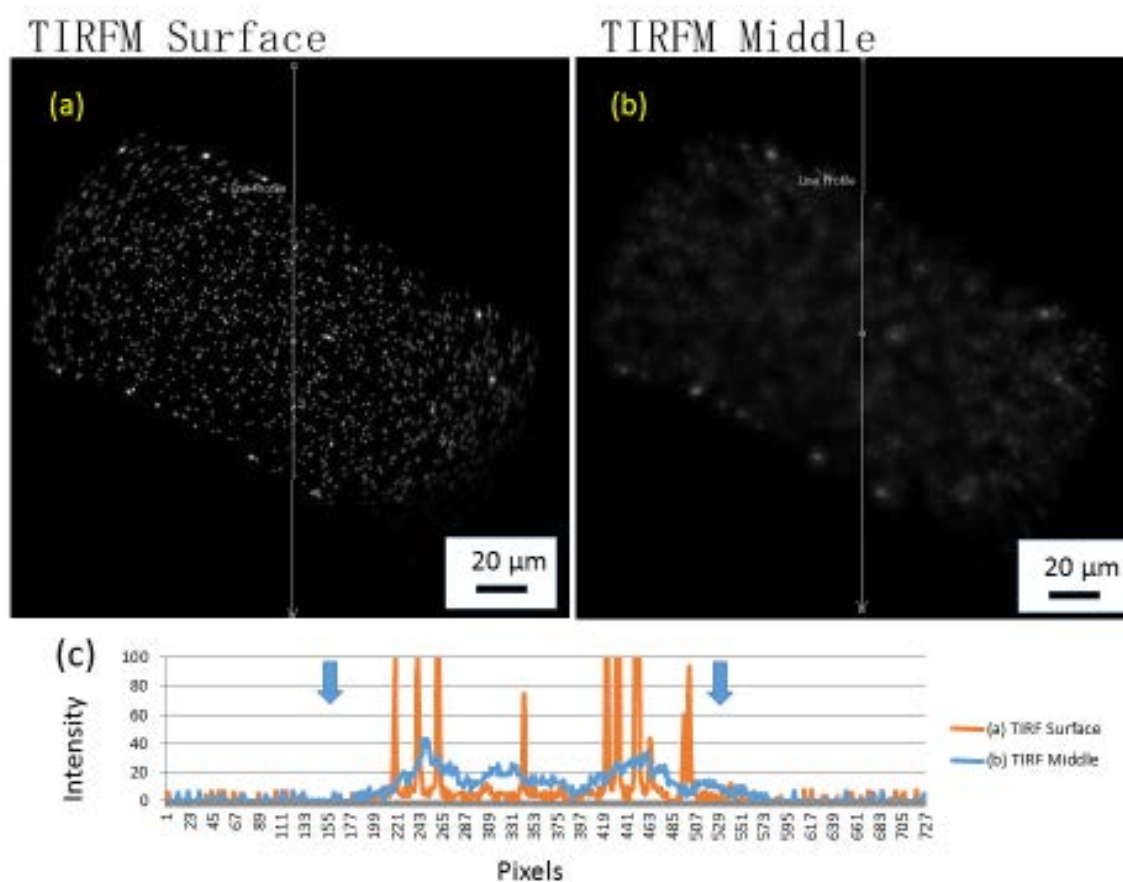

Fig. 3-23   Fluorescence beads in microfluidics image using widefield fluorescence microscopy.

(3-23a) The surface image using TIRF illuminator in widefield fluorescence mode with DIRI off.

(3-23b) The near-surface image using a TIRF illuminator in widefield fluorescence mode, with DIRI off.

_____

(3-23c) Line intensity profiles for (a) and (b).

Then, the microscope was set up in TIRF mode. Laser illumination was used, with the laser in TIRF mode. Samples were illuminated only at the surface of the cover slip. The beads at the surface of the coverslip could be observed clearly, in sharp focus (Fig. 3-24a). Then the microscope focus position was set up for the middle portion of the channel. The floating beads then were not observed well because TIRF illumination could not reach the beads (Fig. 3-24b). This is normal TIRF performance. The position of the microfluidics channel side wall was not clearly observed because TIRF illumination light did not reach to the middle of the channel wall. The arrows shown on the line intensity profile (Fig. 3-24c) refer to Fig. 3-24a and b. The edge of the channel side wall is shown by blue arrows.
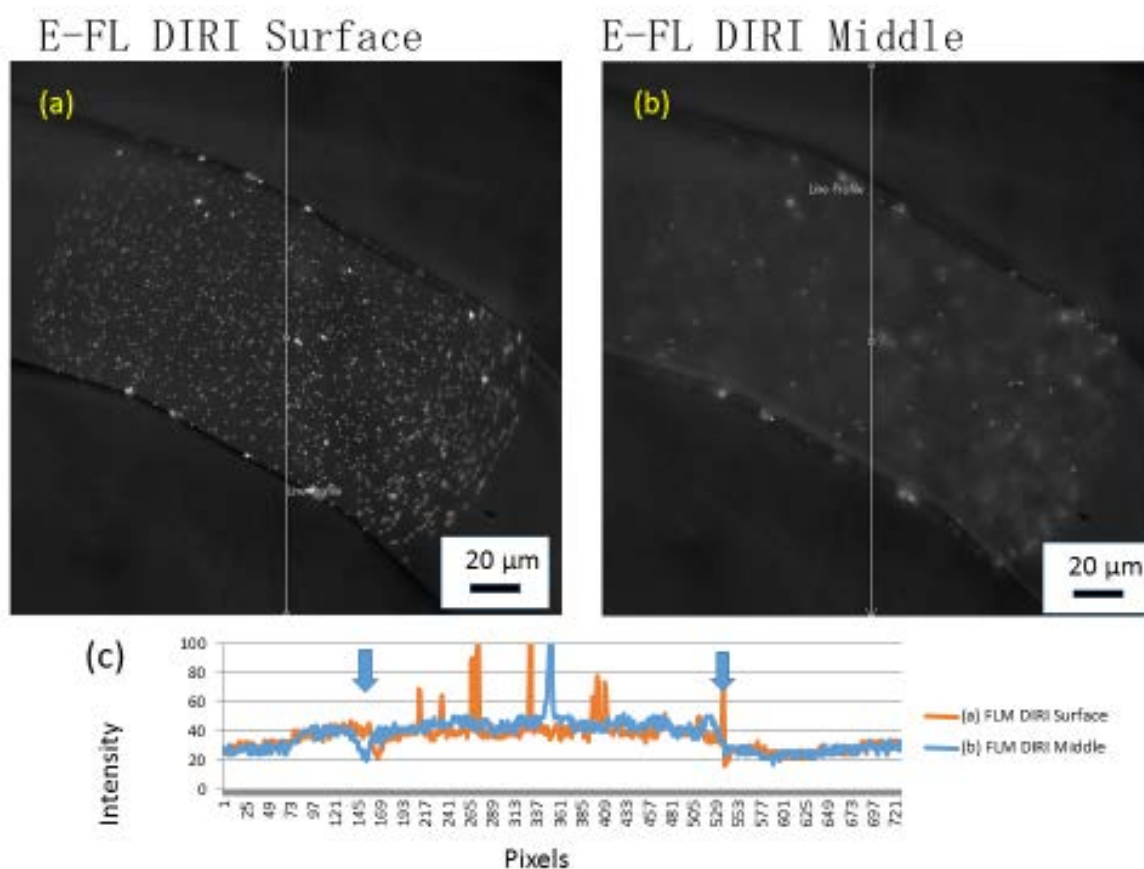
Fig. 3-24   **Fluorescence beads in microfluidics image using TIRF microscopy**

(3-24a) The surface image using the TIRF illuminator in TIRF mode with DIRI off.

(3-24b) The above-the-surface (further from the surface) image using TIRF illuminator in TIRF mode with DIRI off.

(3-24c) Line intensity profiles for (a) and (b).

In the third experiment, the microscope was set up both for use of widefield fluorescence illumination and DIRI. Laser illumination was used and the laser position was set up in widefield mode. White-LED DIRI mode was on. Samples were illuminated using both the widefield fluorescence illumination and DIRI modes. The beads on the surface of the coverslip were observed clearly (Fig. 3-25a). Then the microscope focus position was set up the middle portion of the channel. The floating beads were easily observed (Fig. 3-25b), as was the position of the microfluidics channel side wall. However, the image background noise increased, and image contrast was not high. There are arrows at Fig. 3-25c on the line intensity profile for Fig. 3-25a and b. Blue arrows corresponded to the edge of the channel side wall.

Fig. 3-25   Fluorescence beads in microfluidics image using widefield fluorescence microscopy and DIRI simultaneously**.**

(3-25a) Surface image using TIRF illuminator in widefield fluorescence mode with DIRI on.

(3-25b) Above-the-surface image using TIRF illuminator in widefield fluorescence mode with DIRI on.

(3-25c) Line intensity profiles for (a) and (b).

In the fourth experiment, the microscope was set up for both TIRF illumination mode and DIRI. Laser illumination was used and the laser was set up in TIRF mode. White-LED DIRI

_____

was on. Samples were illuminated for both TIRF and DIRI modes. The beads on the surface of the coverslip were observed clearly (Fig. 3-26a). Then the microscope focus position was set up at the middle position of the channel. The floating beads were observed well, (Fig. 3-26b), as was the position of the microfluidics channel side wall. The image background was increased but not to the same extent as it was when using widefield illumination (Fig. 3-25). The blue arrows on the line intensity profile (Fig. 3-26c) indicate the edge of the channel side wall. The image contrast for Fig. 3-26c is about 2 times higher than it is for Fig. 3-25c.

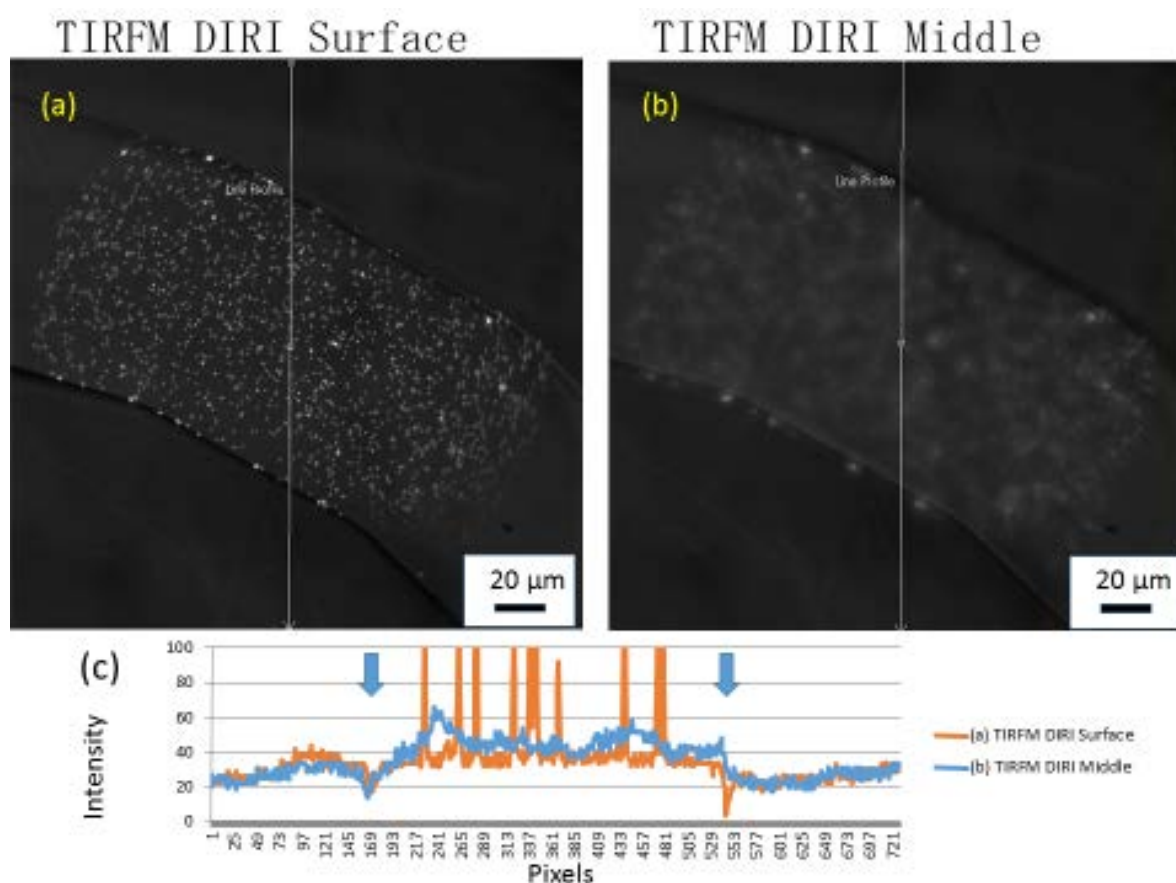**Fig. 3-26   Fluorescence beads in microfluidics image using TIRF microscopy and DIRI simultaneously**

(3-26a) Surface image using TIRF illumination mode with DIRI on.

(3-26b) Above-the-surface image using TIRF illumination mode with DIRI on.

(3-26c) Line intensity profiles for (a) and (b).

_____

3.3.2 Conclusions for section 3.3

TIRF images were successfully observed when using 100x, NA1.65 and 60×NA 1.45 objective lenses. These objectives were easy to use for TIRF imaging.

The image using 100x, NA1.65 objective was brighter than 60xNA1.45 objective. Therefore, 100x, NA1.65 objective expands the scientist's capability to observe dimmer samples. Very-high-NA objectives can provide increased resolution for multiple applications.

The fiber-type TIRF illuminator was easy to set up. The setup time is shorter than just building from optical bench.

The combination of DIRI and TIRF microscopy can help observation of microfluidics. In particular, the surface of the channel can be observed TIRF capability and other parts of the channel can be observed using DIRI. The combination of DIRI with TIRF microscopy was very useful for imaging static and dynamic flow. DIRI illumination proved to be a helpful tool for observing microfluidics channel walls. These results illustrate that combining TIRF and DIRI imaging methods can be effective for microfluidics-related applications.

Chapter 4 Conclusions

1. Development of a DIRI System and its applications with WSI and TIRF microscopy

The combination of DIRI with a WSI system has numerous advantages over traditional darkfield microscopy:

(1) No oil condenser is required for high-resolution imaging.

(2) There is less scatter from dust and dirt on the specimen slide.

(3) There is less halo, providing a more natural darkfield contrast image.

(4) The WSI motorized system produces darkfield, brightfield and fluorescence images.

(5) DIRI well suited for observation and imaging using automated microscopes such as WSI systems.

We also investigated the applicability of three-color LEDs for DIRI illumination. The three-color-LED DIRI system offers the following advantages:

(1) Color balance adjustment is simple. The color balance of the resulting images can be adjusted by pre-adjusting the DIRI color.

(2) Major anatomical details can be resolved with DIRI. Illuminating DAB-stained mid-sagittal brain slices with DIRI enabled a clear image of the corpus callosum structure.

(3) Blue DIRI provides fluorescence excitation. We clearly observed YFP in the associated images.

(4) Darkfield imaging using high-magnification objective lenses such as 20× dry and 40× oil objectives is facilitated by DIRI.

(5) Potentially less sample damage occurs when using red DIRI illumination.

The combination of DIRI and TIRF microscopy has the following advantages:

(1) The surface of the channel can be observed using TIRF capability, while the channel can be observed using DIRI.

(2) The combination of DIRI and TIRF microscopy worked well to elucidate details of both static and dynamic flow imaging.

Finally, these results illustrate that imaging for biological purposes can be facilitated by the use of DIRI combined with WSI or TIRF microscopy.

_____

2.   *Applications for brain research*

WSI produces brain slice images that simultaneously provide high resolution and a wide field of observation that can encompass the entire section, extending far beyond any single field of view. The brain slice can be imaged so that both overall morphology and individual neuronal detail can be seen.

DAB and fluorescent staining are helpful tools for observing protein localization and volume in tissues. However, these methods usually require counter-staining in order to visualize tissue structure, limiting the accuracy of localization of labeled cells within the complex multiple regions of typical neurohistological preparations. DIRI imaging works on the basis of light scattering from refractive index mismatches in the sample. It is a label-free method of producing contrast in a sample. DIRI imaging can be observed small particles in cells or tissue. It is thus very useful for brain research applications, particularly when researchers require additional structural information without the use of further staining.

A novel illumination technique called color DIRI was developed. Instead of using only white LEDs, we used three-color LEDs. As with the white LEDs in the original DIRI, color LEDs are placed at the side of the sample. In addition to its other benefits, DIRI using three-color LEDs provides a solution for color correction. This function helps to provide useful color valance-corrected brain slice images using DIRI.

Brain-expressed fluorescence proteins were observed using color DIRI. DIRI illumination provided the illumination function for fluorescence imaging. DIRI thus provided both the DIRI image and the excitation light for the fluorescence image.

The extension of the motorized WSI system to DIRI has great potential to expand the prospects for observation of brain tissue using light microscopes with a minimum of staining. We tested DIRI for observation of brain slices, used in combination with brightfield, fluorescence, confocal, and TIRF. The system worked well and has application in all these modalities.

3.   *Applications for microfluidics research*

WSI was combined with various modalities to extend the capability of the system and allow multi-modal imaging of an entire microchannel device. Multi-modal imaging allowed clear visualization of both microbubbles and channel walls by utilizing DIRI and brightfield illumination simultaneously.

This imaging methodology is useful not only for examination of static phenomena such as clogging, but also for observation of dynamic phenomena such as the detection of bubbles, fluorescent tracer particles, or labeled cells flowing through a channel. Observation of these dynamics makes possible a whole range of physical and physiological measurements of systems used for modeling more complex *in vivo* situations.

This new multi-modal observation technique will make possible many previously difficult analyses, including observation of phenomena such as vessel wall adhesion of circulating cells under the moderation of pharmacological or physical agents, clot formation and

_____

inhibition, blood vessel obstruction, certain chemotaxis studies, the influence of turbulence on vessel walls, the influence of pharmacological moderators on circulating cell behavior, etc. The system developed here and the model validated in this study will be useful for a wide variety of engineering and biomedical applications using microfluidic devices.

Our experiments only involved brain and microfluidics samples. However, this research indicated that the WSI system may have utility even beyond biological research. It could even one day be appropriate for clinical applications. Our newly developed system helps to elucidate more about life processes, and often provides more information from the sample. We believe this WSI system may be helpful for observing a wide variety of cell and organ types, and indeed for observing almost any microscope slide or microfluidics sample that must be observed at high resolution. Additional applications include cancer research, urology, and translational research, among numerous other fields.

Thus, the experimental results indicate that DIRI has application for the observation of microfluidic devices containing microbubbles, fluorescent particles, or fluorescently labeled cells. The results also indicated that the system was practical to use and fairly simple to implement.

Finally, we did experiments using DIRI with a TIRF microscope. Our results indicate that extension of the motorized TIRF system to include DIRI has potential to expand the prospects for observation of biological samples such as microfluidics. DIRI was particularly helpful when used to observe the channel wall.

References

Adrian, Ronald J. "Particle-imaging techniques for experimental fluid mechanics." Annual review of fluid mechanics 23, no. 1, 261-304 (1991).

Ambrose, E. J. "A surface contact microscope for the study of cell movements." Nature 178, 1194 (1956).

Anna, Shelley L., Nathalie Bontoux, and Howard A. Stone. "Formation of dispersions using "flow focusing" in microchannels." Applied physics letters 82, no. 3, 364-366 (2003).

Axelrod, Daniel. "Cell-substrate contacts illuminated by total internal reflection fluorescence." The Journal of cell biology 89, no. 1, 141-145 (1981).

Axelrod, Daniel. "Total internal reflection fluorescence at biological surfaces." Modern cell biology 9, 93-127 (1990).

Bersini, Simone, Jessie S. Jeon, Gabriele Dubini, Chiara Arrigoni, Seok Chung, Joseph L. Charest, Matteo Moretti, and Roger D. Kamm. "A microfluidic 3D in vitro model for specificity of breast cancer metastasis to bone." Biomaterials 35, no. 8, 2454-2461 (2014).

Blake, Charles A., Holly A. Lavoie, and Clarke F. Millette. "Teaching medical histology at the University of South Carolina School of Medicine: transition to virtual slides and virtual microscopes." The Anatomical Record Part B: The New Anatomist 275, no. 1, 196-206 (2013).

Bohland, Jason W., Caizhi Wu, Helen Barbas, Hemant Bokil, Mihail Bota, Hans C. Breiter, Hollis T. Cline et al. "A proposal for a coordinated effort for the determination of brainwide neuroanatomical connectivity in model organisms at a mesoscopic scale." PLoS Comput Biol 5, no. 3 (2009): e1000334.

Bourdon, Christopher J., Michael G. Olsen, and Allen D. Gorby. "The depth of correlation in micro-PIV for high numerical aperture and immersion objectives." Journal of fluids engineering 128, no. 4, 883-886 (2006).

Chakraborty, Suman. "Preface to Special Topic: Microfluidics in Cancer Research." Biomicrofluidics 7, no. 1 (2013).

Chen, Yuchao, Peng Li, Po-Hsun Huang, Yuliang Xie, John D. Mai, Lin Wang, Nam-Trung Nguyen, and Tony Jun Huang. "Rare cell isolation and analysis in microfluidics." Lab on a Chip 14, no. 4, 626-645 (2014).

Choi, Wonjae, Michinao Hashimoto, Audrey K. Ellerbee, Xin Chen, Kyle JM Bishop, Piotr Garstecki, Howard A. Stone, and George M. Whitesides. "Bubbles navigating through networks of microchannels." Lab on a chip 11, no. 23, 3970-3978 (2011).

Costello, Sean SP, Daniel J. Johnston, Peter A. Dervan, and Daniel G. O'Shea. "Development and evaluation of the virtual pathology slide: a new tool in telepathology." Journal of Medical Internet Research 5, no. 2 (2003).

Das, Tamal, and Suman Chakraborty. "Perspective: Flicking with flow: Can microfluidics revolutionize the cancer research?." Biomicrofluidics 7, no. 1 (2013): 011811.

References
_____

Das, Tamal, Liliane Meunier, Laurent Barbe, Diane Provencher, Olivier Guenat, Thomas Gervais, and Anne-Marie Mes-Masson. "Empirical chemosensitivity testing in a spheroid model of ovarian cancer using a microfluidics-based multiplex platform." Biomicrofluidics 7, no. 1 (2013): 011805.

DICOM Standards Committee, Working Groups 26, Pathology. Supplement 145, Draft 9, (2009)

Dong, Hong-Wei, and Larry W. Swanson. "Projections from the rhomboid nucleus of the bed nuclei of the stria terminalis: implications for cerebral hemisphere regulation of ingestive behaviors." Journal of Comparative Neurology 463, no. 4, 434-472 (2003).

Dong, Hong-Wei, Gorica D. Petrovich, Alan G. Watts, and Larry W. Swanson. "Basic organization of projections from the oval and fusiform nuclei of the bed nuclei of the stria terminalis in adult rat brain." Journal of Comparative Neurology 436, no. 4, 430-455 (2001).

Dong, Hong-Wei, Gorica D. Petrovich, and Larry W. Swanson. "Topography of projections from amygdala to bed nuclei of the stria terminalis." Brain Research Reviews 38, no. 1, 192-246 (2001).

Du, Zhiqiang, N. Colls, Kwan H. Cheng, Mark W. Vaughn, and L. Gollahon. "Microfluidic-based diagnostics for cervical cancer cells." Biosensors and Bioelectronics 21, no. 10, 1991-1995 (2006).

Epstein, Irving R. "Can droplets and bubbles think?." SCIENCE-NEW YORK THEN WASHINGTON- 315, no. 5813, 775 (2007).

Fish, Kenneth N. "Total internal reflection fluorescence (TIRF) microscopy." Current protocols in cytometry, 12-18 (2009).

Fujimoto, Yasushi, and Daisuke Nishiwaki. "Objective lens system for microscope." U.S. Patent 6,747,804, issued June 8 (2004).

Funatsu, Takashi, Yoshie Harada, Makio Tokunaga, Kiwamu Saito, and Toshio Yanagida. "Imaging of single fluorescent molecules and individual ATP turnovers by single myosin molecules in aqueous solution." Nature 374, no. 6522, 555-559 (1995).

Gage, Simon Henry. "Modern dark-field microscopy and the history of its development." Transactions of the American Microscopical Society 39, no. 2, 95-141 (1920).

Garstecki, Piotr, Irina Gitlin, Willow DiLuzio, George M. Whitesides, Eugenia Kumacheva, and Howard A. Stone. "Formation of monodisperse bubbles in a microfluidic flow-focusing device." Applied Physics Letters 85, no. 13, 2649-2651 (2004).

Garstecki, Piotr, Michael J. Fuerstman, Howard A. Stone, and George M. Whitesides. "Formation of droplets and bubbles in a microfluidic T-junction—scaling and mechanism of break-up." Lab on a Chip 6, no. 3, 437-446 (2006).

Gilbert, Charles D., and TORSTEN N. Wiesel. "Clustered intrinsic connections in cat visual cortex." The Journal of Neuroscience 3, no. 5, 1116-1133 (1983).

Gravesen, Peter, Jens Branebjerg, and O. Søndergård Jensen. "Microfluidics-a review." Journal of Micromechanics and Microengineering 3, no. 4, 168 (1993).

Haugland RP, ed., Handbook of fluorescent probes and research chemicals, 6th ed. Molecular Probes Inc., Eugene, OR (1996).

Heath, James R., and Mark E. Davis. "Nanotechnology and cancer." Annual review of medicine 59, 251 (2008).

References

_____

Hecht E. Optics, Fourth Edition, Addison Wesley Longman, Inc. 86–141 (2002).

Hotani, Hirokazu, and Tetsuya Horio. "Dynamics of microtubules visualized by darkfield microscopy: treadmilling and dynamic instability." Cell motility and the cytoskeleton 10.1-2, 229-236 (1988).

Hou, Han Wei, Q. S. Li, G. Y. H. Lee, A. P. Kumar, C. N. Ong, and Chwee Teck Lim. "Deformability study of breast cancer cells using microfluidics." Biomedical microdevices 11, no. 3, 557-564 (2009).

Hu, Min, Carolina Novo, Alison Funston, Haining Wang, Hristina Staleva, Shengli Zou, Paul Mulvaney, Younan Xia, and Gregory V. Hartland. "Dark-field microscopy studies of single metal nanoparticles: understanding the factors that influence the linewidth of the localized surface plasmon resonance." Journal of materials chemistry 18, no. 17, 1949-1960 (2008).

Huang, Yu, Basheal Agrawal, Dandan Sun, John S. Kuo, and Justin C. Williams. "Microfluidics-based devices: New tools for studying cancer and cancer stem cell migration." Biomicrofluidics 5, no. 1 (2011): 013412.

i Solvas, XavieráCasadevall. "Droplet microfluidics: recent developments and future applications." Chemical Communications 47, no. 7, 1936-1942 (2011).

Ishikawa, Takuji, Hiroki Fujiwara, Noriaki Matsuki, Takefumi Yoshimoto, Yohsuke Imai, Hironori Ueno, and Takami Yamaguchi. "Asymmetry of blood flow and cancer cell adhesion in a microchannel with symmetric bifurcation and confluence." Biomedical microdevices 13, no. 1, 159-167 (2011).

Jaiswal, Jyoti K., Hedi Mattoussi, J. Matthew Mauro, and Sanford M. Simon. "Long-term multiple color imaging of live cells using quantum dot bioconjugates." Nature biotechnology 21, no. 1, 47-51 (2003).

Jaiswal, Jyoti K., and Sanford M. Simon. "Imaging single events at the cell membrane." Nature chemical biology 3, no. 2, 92-98 (2007).

Kawano, Yoshihiro, Enders RG. "Total internal reflection fluorescence microscopy." American Biotechnology Laboratory, 17, No. 13 (1999).

Kawano, Yoshihiro and Enders G. Reinhard. "Total internal reflection fluorescence microscopy." Application Note, 28-30, December (1999).

Kawano, Yoshihiro, Chikara Abe, Katsuyuki Abe, Kazuhiro Hayashi, Yoko Hatta and Keisuke Tamura. "Macro optical system for biological application." International Symposium on Optical Science and Technology, SPIE, 288-296 (2000).

Kawano, Yoshihiro, Chikara Abe, Toru Kaneda, Yasushi Aono, Katsuyuki Abe, Keisuke Tamura, and Susumu Terakawa. "High-numerical-aperture objective lenses and optical system improved objective type total internal reflection fluorescence microscopy." In International Symposium on Optical Science and Technology, SPIE, pp. 142-151 (2000).

Kawano, Yoshihiro, Christopher Higgins, Yasuhito Yamamoto, Julie Nyhus, Amy Bernard, Hong-Wei Dong, Harvey J. Karten, and Tobias Schilling. "Darkfield adapter for whole slide imaging: Adapting a darkfield internal reflection illumination system to extend wsi applications." PloS one 8, no. 3 (2013): e58344.

Kawano, Yoshihiro, Chino Otsuka, James Sanzo, Christopher Higgins, Tatsuo Nirei, Tobias Schilling, Takuji Ishikawa. (2015). Expanding Imaging Capabilities for Microfluidics: Applicability of Darkfield Internal Reflection Illumination (DIRI) to Observations in Microfluidics. PloS one, 10.3 (2015).

Kim, Minseok S., Taemin Kim, Sun-Young Kong, Soim Kwon, Chae Yun Bae, Jaekyu Choi, Chul Hwan Kim, Eun Sook Lee, and Je-Kyun Park. "Breast cancer diagnosis using a microfluidic multiplexed immunohistochemistry platform." PloS one 5, no. 5 (2010): e10441.

Kinoshita, Haruyuki, Shohei Kaneda, Teruo Fujii, and Marie Oshima. "Three-dimensional measurement and visualization of internal flow of a moving droplet using confocal micro-PIV." Lab on a Chip 7, no. 3, 338-346 (2007).

Kirby, Brian J., Mona Jodari, Matthew S. Loftus, Gunjan Gakhar, Erica D. Pratt, Chantal Chanel-Vos, Jason P. Gleghorn et al. "Functional characterization of circulating tumor cells with a prostate-cancer-specific microfluidic device." PloS one 7, no. 4 (2012): e35976.

Leble, Vladimir, Rui Lima, Ricardo Dias, Carla Fernandes, Takuji Ishikawa, Yohsuke Imai, and Takami Yamaguchi. "Asymmetry of red blood cell motions in a microchannel with a diverging and converging bifurcation." Biomicrofluidics 5, no. 4 (2011): 044120.

Lein, Ed S., Michael J. Hawrylycz, Nancy Ao, Mikael Ayres, Amy Bensinger, Amy Bernard, Andrew F. Boe et al. "Genome-wide atlas of gene expression in the adult mouse brain." Nature 445, no. 7124, 168-176 (2007).

Leong, F. J., and JO'D. McGee. "Automated complete slide digitization: a medium for simultaneous viewing by multiple pathologists." The Journal of pathology 195, no. 4, 508-514 (2001).

Lima, Rui, Mónica SN Oliveira, Takuji Ishikawa, Hirokazu Kaji, Shuji Tanaka, Matsuhiko Nishizawa, and Takami Yamaguchi. "Axisymmetric polydimethysiloxane microchannels for in vitro hemodynamic studies." Biofabrication 1, no. 3 (2009): 035005.

Lima, Rui, Shigeo Wada, Ken-ichi Tsubota, and Takami Yamaguchi. "Confocal micro-PIV measurements of three-dimensional profiles of cell suspension flow in a square microchannel." Measurement Science and Technology 17, no. 4, 797 (2006).

Lima, Rui, Shigeo Wada, Motohiro Takeda, Ken-ichi Tsubota, and Takami Yamaguchi. "In vitro confocal micro-PIV measurements of blood flow in a square microchannel: the effect of the haematocrit on instantaneous velocity profiles." Journal of biomechanics 40, no. 12, 2752-2757 (2007).

Lima, Rui, Shigeo Wada, Shuji Tanaka, Motohiro Takeda, Takuji Ishikawa, Ken-ichi Tsubota, Yohsuke Imai, and Takami Yamaguchi. "In vitro blood flow in a rectangular PDMS microchannel: experimental observations using a confocal micro-PIV system." Biomedical Microdevices 10, no. 2, 153-167 (2008).

Lima, Rui, Takuji Ishikawa, Yohsuke Imai, Motohiro Takeda, Shigeo Wada, and Takami Yamaguchi. "Measurement of individual red blood cell motions under high hematocrit conditions using a confocal micro-PTV system." Annals of biomedical engineering 37, no. 8, 1546-1559 (2009).

Lima, Rui, Takuji Ishikawa, Yohsuke Imai, Motohiro Takeda, Shigeo Wada, and Takami Yamaguchi. "Radial dispersion of red blood cells in blood flowing through glass capillaries: the role of hematocrit and geometry." Journal of biomechanics 41, no. 10, 2188-2196 (2008).

Link, D. R., Shelley L. Anna, D. A. Weitz, and H. A. Stone. "Geometrically mediated breakup of drops in microfluidic devices." Physical review letters 92, no. 5 (2004): 054503.

_____

Liu, Ziji, Lei Tian, Sijia Liu, and Laura Waller. "Real-time brightfield, darkfield, and phase contrast imaging in a light-emitting diode array microscope." Journal of biomedical optics 19, no. 10, 106002-106002 (2014).

Loerke, Dinah, Beate Preitz, Walter Stu, and Martin Oheim. "Super-resolution measurements with evanescent-wave fluorescence excitation using variable beam incidence." Journal of biomedical optics 5, no. 1, 23-30 (2000).

Long, Richard E., Adam Smith, Sam V. Machotka, Elizabeth Chlipala, Jennifer Cann, Brian Knight, Yoshihiro Kawano, Jesus Ellin, and Amanda Lowe. "Scientific and Regulatory Policy Committee (SRPC) Paper Validation of Digital Pathology Systems in the Regulated Nonclinical Environment." Toxicologic pathology 41, no. 1, 115-124 (2013).

Maheswaran, Shyamala, Lecia V. Sequist, Sunitha Nagrath, Lindsey Ulkus, Brian Brannigan, Chey V. Collura, Elizabeth Inserra et al. "Detection of mutations in EGFR in circulating lung-cancer cells." New England Journal of Medicine 359, no. 4, 366-377 (2008).

Manz, Andréas, N. Graber, and H. áM Widmer. "Miniaturized total chemical analysis systems: a novel concept for chemical sensing." Sensors and actuators B: Chemical 1, no. 1, 244-248 (1990).

Mauk, Michael G., Barry L. Ziober, Zongyuan Chen, Jason A. Thompson, and Haim H. Bau. "Lab-on-a-Chip Technologies for Oral-Based Cancer Screening and Diagnostics." Annals of the New York Academy of Sciences 1098, no. 1, 467-475 (2007).

Meinhart, Carl D., Steve T. Wereley, and Juan G. Santiago. "PIV measurements of a microchannel flow." Experiments in fluids 27, no. 5, 414-419 (1999).

Microscope History: find out about the history of microscope, http://www.visioneng.com/resources/history-of-the-microscope [accessed June 14, 2015].

Mikula, Shawn, Issac Trotts, James M. Stone, and Edward G. Jones. "Internet-enabled high-resolution brain mapping and virtual microscopy." Neuroimage 35, no. 1, 9-15 (2007).

Miyawaki, Atsushi, Hiroshi Homma, Hiro-omi Tamura, Michio Matsui, and Katsuhiko Mikoshiba. "Zonal distribution of sulfotransferase for phenol in olfactory sustentacular cells." The EMBO journal 15, no. 9, 2050 (1996).

Nagrath, Sunitha, Lecia V. Sequist, Shyamala Maheswaran, Daphne W. Bell, Daniel Irimia, Lindsey Ulkus, Matthew R. Smith et al. "Isolation of rare circulating tumour cells in cancer patients by microchip technology." Nature 450, no. 7173, 1235-1239 (2007).

Ng, Lydia, Amy Bernard, Chris Lau, Caroline C. Overly, Hong-Wei Dong, Chihchau Kuan, Sayan Pathak et al. "An anatomic gene expression atlas of the adult mouse brain." Nature neuroscience 12, no. 3, 356-362 (2009).

Ohara-Imaizumi, Mica, Yoko Nakamichi, Toshiaki Tanaka, Hitoshi Ishida, and Shinya Nagamatsu. "Imaging Exocytosis of Single Insulin Secretory Granules with Evanescent Wave Microscopy DISTINCT BEHAVIOR OF GRANULE MOTION IN BIPHASIC INSULIN RELEASE." Journal of Biological Chemistry 277, no. 6, 3805-3808 (2002).

Oheim, Martin, and Florian Schapper. "Non-linear evanescent-field imaging." Journal of Physics D: Applied Physics 38, no. 10, R185 (2005).

Oheim, Martin, and Walter Stühmer. "Multiparameter evanescent-wave imaging in biological fluorescence microscopy." Quantum Electronics, IEEE Journal of 38, no. 2, 142-148 (2002).

Hecht. Optics fourth edition (2002).

Pantanowitz, Liron, Paul N. Valenstein, Andrew J. Evans, Keith J. Kaplan, John D. Pfeifer, David C. Wilbur, Laura C. Collins, and Terence J. Colgan. "Review of the current state of whole slide imaging in pathology." Journal of pathology informatics 2, no. 1, 36 (2011).

Pluta M. Advanced Light Microscopy Volume 2 Specialized Methods. Elsevier. 102–113 (1989).

Park, Jae Sung, Chang Kyoung Choi, and Kenneth D. Kihm. "Optically sliced micro-PIV using confocal laser scanning microscopy (CLSM)." Experiments in Fluids 37, no. 1, 105-119 (2004).

Prabhakarpandian, Balabhaskar, Kapil Pant, Robert C. Scott, Christopher B. Patillo, Daniel Irimia, Mohammad F. Kiani, and Shivshankar Sundaram. "Synthetic microvascular networks for quantitative analysis of particle adhesion." Biomedical microdevices 10, no. 4, 585-595 (2008).

Prabhakarpandian, Balabhaskar, Ming-Che Shen, Kapil Pant, and Mohammad F. Kiani. "Microfluidic devices for modeling cell–cell and particle–cell interactions in the microvasculature." Microvascular research 82, no. 3, 210-220 (2011).

Prabhakarpandian, Balabhaskar, Yi Wang, A. N. G. E. L. A. REA-RAMSEY, Shivshankar Sundaram, Mohammad F. Kiani, and Kapil Pant. "Bifurcations: focal points of particle adhesion in microvascular networks." Microcirculation 18, no. 5, 380-389 (2011).

Prakash, Manu, and Neil Gershenfeld. "Microfluidic bubble logic." Science 315, no. 5813, 832-835 (2007).

Prasad, A. K., R. J. Adrian, C. C. Landreth, and P. W. Offutt. "Effect of resolution on the speed and accuracy of particle image velocimetry interrogation." Experiments in Fluids 13, no. 2-3, 105-116 (1992).

Reyes-Irisarri, Elisabet, Silvia Pérez-Torres, and G. Mengod. "Neuronal expression of cAMP-specific phosphodiesterase 7B mRNA in the rat brain." Neuroscience 132, no. 4, 1173-1185 (2005).

Rosano, Jenna M., Nazanin Tousi, Robert C. Scott, Barbara Krynska, Victor Rizzo, Balabhaskar Prabhakarpandian, Kapil Pant, Shivshankar Sundaram, and Mohammad F. Kiani. "A physiologically realistic in vitro model of microvascular networks." Biomedical microdevices 11, no. 5, 1051-1057 (2009).

Sackmann, Eric K., Anna L. Fulton, and David J. Beebe. "The present and future role of microfluidics in biomedical research." Nature 507, no. 7491, 181-189 (2014).

Santiago, Juan G., Steve T. Wereley, Carl D. Meinhart, D. J. Beebe, and Ronald J. Adrian. "A particle image velocimetry system for microfluidics." Experiments in fluids 25, no. 4, 316-319 (1998).

Schapper, Florian, José Tiago Gonçalves, and Martin Oheim. "Fluorescence imaging with two-photon evanescent wave excitation." European Biophysics Journal 32, no. 7, 635-643 (2003).

Schleifman, Erica B., Rachel Tam, Rajesh Patel, Alison Tsan, Teiko Sumiyoshi, Ling Fu, Rupal Desai et al. "Next Generation MUT-MAP, a High-Sensitivity High-Throughput Microfluidics Chip-Based Mutation Analysis Panel." PloS one 9, no. 3 (2014): e90761.

Schmoranzer, Jan, Mark Goulian, Dan Axelrod, and Sanford M. Simon. "Imaging constitutive exocytosis with total internal reflection fluorescence microscopy." The Journal of cell biology 149, no. 1, 23-32 (2000).

References

_____

Smith, Zachary J., Tingjuan Gao, Kaiqin Chu, Stephen M. Lane, Dennis L. Matthews, Denis M. Dwyre, James Hood, Keith Tatsukawa, Laurence Heifetz, and Sebastian Wachsmann-Hogiu. "Single-step preparation and image-based counting of minute volumes of human blood." Lab on a Chip 14, no. 16, 3029-3036 (2014).

Song, Jonathan W., Stephen P. Cavnar, Ann C. Walker, Kathryn E. Luker, Mudit Gupta, Yi-Chung Tung, Gary D. Luker, and Shuichi Takayama. "Microfluidic endothelium for studying the intravascular adhesion of metastatic breast cancer cells." PloS one 4, no. 6 (2009): e5756.

Sonnleitner, Alois, Lidia M. Mannuzzu, Susumu Terakawa, and Ehud Y. Isacoff. "Structural rearrangements in single ion channels detected optically in living cells." Proceedings of the National Academy of Sciences 99, no. 20, 12759-12764 (2002).

Sorger, Peter K. "Microfluidics closes in on point-of-care assays." Nature biotechnology 26, no. 12, 1345-1346 (2008).

Steyer, Jürgen A., Heinz Horstmann, and Wolfhard Almers. "Transport, docking and exocytosis of single secretory granules in live chromaffin cells." Nature 388, no. 6641, 474-478 (1997).

Suzuki, Toshinobu. "Immersion microscope objective." U.S. Patent 5,659,425, issued August 19 (1997).

Tanaka, Tatsuya, Takuji Ishikawa, Keiko Numayama-Tsuruta, Yohsuke Imai, Hironori Ueno, Noriaki Matsuki, and Takami Yamaguchi. "Separation of cancer cells from a red blood cell suspension using inertial force." Lab on a Chip 12, no. 21, 4336-4343 (2012).

Teh, Shia-Yen, Robert Lin, Lung-Hsin Hung, and Abraham P. Lee. "Droplet microfluidics." Lab on a Chip 8, no. 2, 198-220 (2008).

Terakawa S, Mannuzzu L, Feller B, Isacoff E, Visualization of a single K-channel by evanescence fluorescence microscopy. Abstract, Biophysical Society Meeting, Baltimore (1998).

Terakawa, S., T. Sakurai, and K. Abe. "Development of an objective lens with a high numerical aperture for light microscopy." Bioimages 5, 24 (1997).

Terakawa, Susumu, Takashi Tsuboi, Takashi Sakurai, Andreas Jeromin, Yoshihiko Wakazono, Seiji Yamamoto, and Katsuyuki Abe. "Fluorescence micro-imaging of living cells and biomolecules with ultrahigh NA objectives." In International Symposium on Photonics and Applications, 121-127. International Society for Optics and Photonics (2001).

Theberge, Ashleigh B., Fabienne Courtois, Yolanda Schaerli, Martin Fischlechner, Chris Abell, Florian Hollfelder, and Wilhelm TS Huck. "Microdroplets in microfluidics: an evolving platform for discoveries in chemistry and biology." Angewandte Chemie International Edition 49, no. 34, 5846-5868 (2010).

Tokunaga, Makio, Kazuo Kitamura, Kiwamu Saito, Atsuko Hikikoshi Iwane, and Toshio Yanagida. "Single molecule imaging of fluorophores and enzymatic reactions achieved by objective-type total internal reflection fluorescence microscopy." Biochemical and biophysical research communications 235, no. 1, 47-53 (1997).

Tousi, Nazanin, Bin Wang, Kapil Pant, Mohammad F. Kiani, and Balabhaskar Prabhakarpandian. "Preferential adhesion of leukocytes near bifurcations is endothelium independent." Microvascular research 80, no. 3, 384-388 (2010).

van't Hoff, Marcel, Vincent de Sars, and Martin Oheim. "A programmable light engine for quantitative single molecule TIRF and HILO imaging." Optics express 16, no. 22, 18495-18504 (2008).

References

_____

von Olshausen, Philipp, and Alexander Rohrbach. "Coherent total internal reflection dark-field microscopy: label-free imaging beyond the diffraction limit." Optics letters 38, no. 20, 4066-4069 (2013).

Wax, Adam, and Konstantin Sokolov. "Molecular imaging and darkfield microspectroscopy of live cells using gold plasmonic nanoparticles." Laser & Photonics Reviews 3, no. 1-2, 146-158 (2009).

Weinstein, Ronald S., Anna R. Graham, Lynne C. Richter, Gail P. Barker, Elizabeth A. Krupinski, Ana Maria Lopez, Kristine A. Erps, Achyut K. Bhattacharyya, Yukako Yagi, and John R. Gilbertson. "Overview of telepathology, virtual microscopy, and whole slide imaging: prospects for the future." Human pathology 40, no. 8, 1057-1069 (2009).

Whitesides, George M. "The origins and the future of microfluidics." Nature 442, no. 7101, 368-373 (2006).

Wlodkowic, Donald, and Zbigniew Darzynkiewicz. "Microfluidics: emerging prospects for anti-cancer drug screening." World journal of clinical oncology 1, no. 1, 18 (2010).

Yagi, Yukako, and John R. Gilbertson. "Digital imaging in pathology: the case for standardization." Journal of telemedicine and telecare 11, no. 3, 109-116 (2005).

Yagi, Yukako. "Color standardization and optimization in whole slide imaging." Diagn Pathol 6, no. Suppl 1, S15 (2011).

Yung, Tony KF, KC Allen Chan, Tony SK Mok, Joanna Tong, Ka-Fai To, and YM Dennis Lo. "Single-molecule detection of epidermal growth factor receptor mutations in plasma by microfluidics digital PCR in non–small cell lung cancer patients." Clinical Cancer Research 15, no. 6, 2076-2084 (2009).

Zervantonakis, Ioannis K., Shannon K. Hughes-Alford, Joseph L. Charest, John S. Condeelis, Frank B. Gertler, and Roger D. Kamm. "Three-dimensional microfluidic model for tumor cell intravasation and endothelial barrier function." Proceedings of the National Academy of Sciences 109, no. 34, 13515-13520 (2012).

Zhang, Weijia, Dong Soon Choi, Yen H. Nguyen, Jenny Chang, and Lidong Qin. "Studying cancer stem cell dynamics on PDMS surfaces for microfluidics device design." Scientific reports 3 (2013).

_____

Appendix

Theoretical background

This appendix presents the conceptual basis for a variety of microscope systems and the theoretical foundation of each type of microscope's optical system.

Section A1 describes conventional widefield fluorescence microscopy (CWFM) and conventional fluorescence microscopy (CFM). The CWFM is a very basic setup for an optical microscope. The CFM is one of the useful tools for biological investigation. Section A2 describes confocal microscopy (CM). CM is a technique to prevent out-of-focus light from affecting the image. Images captured using CM have higher contrast than CFM images. CM has been used for many biological samples using fluorescent markers. Section A3 describes the concept of Total Internal Reflection Fluorescence Microscopy (TIRFM). TIRFM is a useful technique to observe a cell's surface using fluorescent markers. TIRFM images generally provide even higher image contrast than CM. Section A4 describes the concept of darkfield microscopy (DFM). DFM is useful for the observation of a sample for detecting small structures without having to stain the sample.

Michael Davidson, Florida State University, created a robust educational website devoted to microscopy. A group from Olympus including Mort Abramowitz, Bill Fester and I supported Mr. Davidson's activities and helped with the website. This appendix includes much material on the theory of microscopy as cited on these listed web pages

The Florida State University Optical Microscope Primer

   URL: http://micro.magnet.fsu.edu/primer/index.html

Olympus Resource Center home page

   URL: http://www.olympusmicro.com/

_____

A1.   Conventional widefield microscopy and fluorescence microscopy

Section A1.1 presents information on the design of conventional widefield microscopes (CWFM) and conventional fluorescence microscopes (CFM). Section A1.2 presents theoretical concepts for lateral resolution, and Section A1.3 presents concepts for axial resolution.

A1.1. Design of conventional widefield microscopes (CWFM) and conventional fluorescence microscopes (CFM)

The basic design of the optical microscope was developed by Zaccharias Janssen in 1595. His basic concept remains in place in today's conventional widefield microscopy (CWFM). Of course, over time, performance of various subunits of the microscope, such as the light source, objective lens, and detection system, have greatly improved. The widefield microscope consists of an illumination unit, an observation unit, and an imaging device. If more magnification is needed, an extra magnification lens may be added.
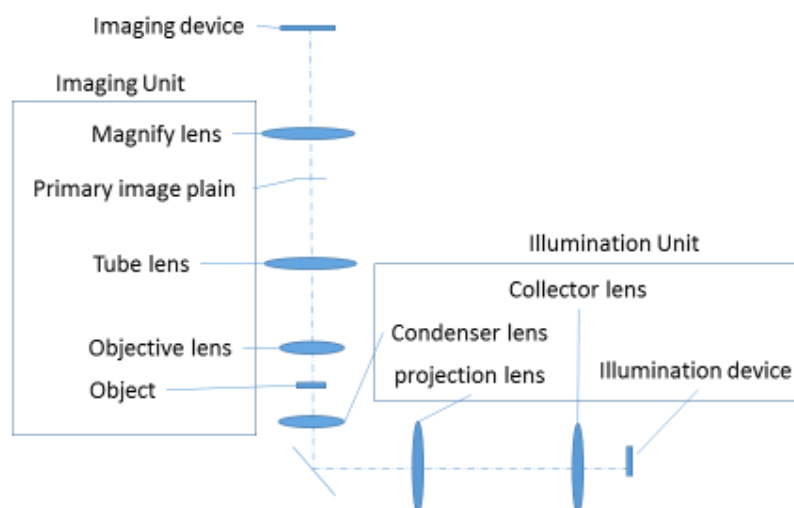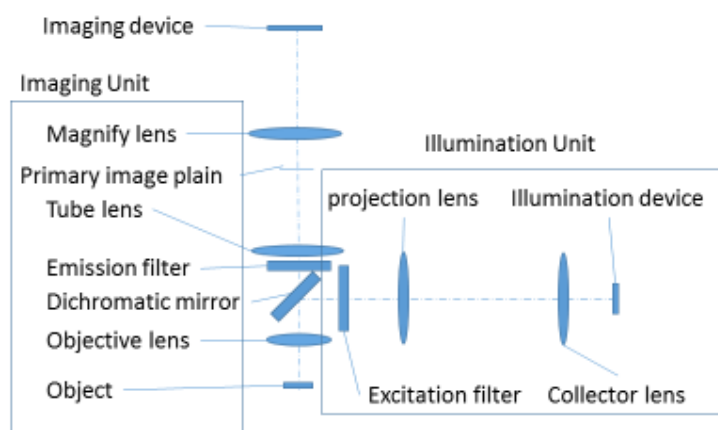

Fig. A-1. Widefield brightfield microscope system

_____

The basic design of a widefield brightfield fluorescence microscope (CWFM) is shown in Fig. A-1. The brightfield microscope consists of a transmitting illumination unit, an observation unit, and an imaging device. The transmitted illumination unit includes the light source, collector lens, a projection lens and a condenser lens. The most common light source is a halogen lamp. Recently, LED light sources are growing in use because they last far longer than a halogen lamp. Also, when the light intensity changes, the LED does not change color while a halogen lamp does change.

The observation unit consists of the objective lens, tube lens and extended magnification lens. Most advanced microscopes are based on an infinity optical design. Infinity optical design refers to the fact that the optical pass between the objective lens and tube lens is infinity. Furthermore, the infinity desigin fits the intermediate optical system in the infinity space. For example, without changing the magnification of the optical system, the epi-fluorescene unit can be fit into the infinity optical space. The ratio of the focal length of the objective lens and the tube lens provides the magnification.

Objective lenses range from about 1.25x to 100x. Some manufacturers have introduced objective lenses that that are lower than 1x and higher than 100x. When higher magnification images are required, it is possible to add an extended magnification lens after the tube lens. The imaging device is compatible with a variety of cameras. Two types of imaging device – CCD and CMOS – are most commonly used. Either color or black and white imaging can be done, depending on the application. Fig. A-1 shows a typical configuration for a brightfield microscope.

Fig. A-2. Conventional widefield fluorescence microscope system

The basic optical layout of a typical conventional fluorescence microscope (CFM) is

_____

depicted in Fig. A-2. A fluorescence microscope consists of an incident-light fluorescence illumination unit, an observation unit, and an imaging device. The incident-light fluorescence illumination unit consists of a mercury-vapor burner light source, a collector lens, a projection lens and a condenser lens. Until recently, a mercury-vapor burner was most commonly used, but recently, much work requires mercury-free experiments and equipment. Thus, the use of LED illumination is growing quickly. However, LED illumination still does not provide the brightness of a mercury burner. The observation unit consists of the objective lens, tube lens and extended magnification lens. The fluorescence microscope uses a higher-numerical-aperture and higher-transmission objective lens. Moreover, some applications require ultraviolet (UV) transmission for fluorescence excitation. When higher magnification is needed, it is possible to add an extended-magnification lens after the tube lens. The system is compatible with a wide variety of cameras, and CCD and CMOS cameras are the most commonly used. Both color and black-and-white imaging is available. Good cameras require high quantum efficiency and low noise. To achieve these conditions, the scientist usually uses scientific-grade, cooled-CCD or CMOS cameras.

A1.2. Lateral resolution of widefield microscopy and fluorescence microscopy

The key requirement for any microscope is the ability to resolve images. This section is devoted to explaining optical resolution.

Fundamentally, the resolution of any optical system is limited by the physics of light. Ernest K. Abbe discovered diffraction limits (Abbe (1873)). There are many articles published that explain the resolution of the microscope (Born et al. (1999); Inoue (1986), Pawley (2010); Davidson (2002); Abramowitz (2002); Goodman (1986)).

In the real world, it is hard to remove design and manufacturing error from an optical system, and most optical systems normally have some small level of design and manufacturing flaws. For purposes of discussion here, though, we will consider an ideal, aberration-free system. Microscope resolution is defined as the smallest distance apart that two points can be where the user is still able to distinguish between them. The resolution of a microscope depends on many physical factors: for example, the wavelength of light, often represented as λ, and the numerical aperture (NA). The NA is defined according to the formula below (A1.1), where n is the refractive index of the immersion medium and θ is the half angle of the maximum light that is collected by the objective lens.

$$NA = n \, sin \, \theta \qquad\qquad (A1.1)$$

The conventional widefield microscope (CWM) illumination system can use either LED or halogen light. Both are incoherent light sources. The formula (A1.2) below shows that two

_____

individual points are detected by a detector when their distance is not smaller than r lateral. According to the theory, on the line between the midpoint of the first point and the second point, the contrast between the maximum and minimum intensity should be at least 26% (ΔI = 0.26) lower than the maximum. The two points are overlapping, with the Airy disk of one on the first-order ring of the other. This standard for separation is known as the Rayleigh Criterion (A1.2).

$$r_{lateral} = r_{airy} = 0.61 \times \frac{\lambda}{NA} \qquad \text{(A1.2)}$$

Where r lateral is the minimum lateral distance between resolvable two points. λ is the wavelength of light. In the case of fluorescence, this is the emission wavelength. NA is the numerical aperture.

The Airy disk is described as a perfectly circular aperture for the objective lens. Also, the objective lens makes an optimally focused spot of light that limits diffraction. Radius lateral resolution is same as a radius Airy disk. Various objective lenses and their widefield lateral resolution are presented in Table A-1.

Table A-1. Common objective specifications & widefield lateral resolution. (*λ=500 nm.*)

Magnification	Type	*NA*	Working Distance	$r_{lateral}$
100X	Oil	1.4	0.13 mm	0.22 µm
60X	Silicon	1.3	0.13 mm	0.23 µm
60X	Water	1.2	0.28 mm	0.25 µm
40X	Dry	0.95	0.18 mm	0.32 µm
20X	Dry	0.75	0.6 mm	0.41 µm
10X	Dry	0.4	3.1 mm	0.76 µm
4X	Dry	0.16	13 mm	1.91 µm
2X	Dry	0.1	8.5 mm	3.05 µm

The basic configuration of CWM requires a sample stage, an objective lens, and a condenser lens. Then the NA of the objective lens and condenser lens are critical units for determining resolution. The formula (A1.3) shows that resolution is related to the

_____

condenser's numerical aperture and objective's numerical aperture. If the condenser lens has a numerical aperture that is far below the numerical aperture of the objective, it is extremely difficult to achieve high-resolution imaging.

$$r = \frac{1.22\lambda}{NA_{obj} + NA_{cond}} \qquad \text{(A1.3)}$$

The Rayleigh criterion is a very useful formula because it explains basic optical performance.

A1.3. Axial resolution of widefield microscopy

The objective lens can be focused for depth without any movement of the focus position. The depth of focus for the axial direction of the image is the total depth of field (d_{tot}). The total depth of field (d_{tot}) is given by the geometrical optical depths of field.

$$d_{tot} = \frac{\lambda_n}{NA2} + \left(\frac{n \times NA}{M}\right)e \qquad \text{(A1.4)}$$

where λ is the wavelength of illumination and n is the refractive index of the immersion medium or air. If the medium is air then $n = 1$. NA is the objective lens numerical aperture, M is the objective lens lateral magnification. e is the minimum distance that can be resolved by an imaging device that is placed in the image plane of the objective. This formula is useful for understanding the idea of the depth of field. The use of higher-NA objective lenses thus reduces the depth of field.

_____
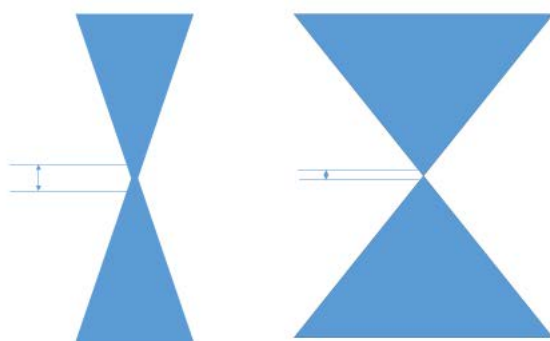
Fig. A-3. The depth of the axial direction of the focused image.

The key point is that the lateral resolution limit reduces to the first power of the numerical aperture. Also, the diffraction-limited depth of field is decreased in inverse proportion to the square of the numerical aperture. The result is that the axial resolution and the thickness of optical sections relate to the numerical aperture of the objective lens (see Table A-2). The conventional microscope can be used to observe not only the optical section of the focus-point image, but it also observes the entire Z direction (depth), although most of it is out of focus. When we observe three-dimensionally spread fluorescence beads using a widefield fluorescence microscope, we observe focused beads as well as out-of-focus beads. This is an important point of comparison with the confocal microscope, where only focused beads can be observed, as, typically out-of-focus light is eliminated from the image by the confocal pinhole.

Table A-2. Depth of field. ($e=1, \lambda=500\ nm$)

Magnification	Type	NA	Depth of Field	$r_{lateral}$
100X	Oil	1.4	0.20 µm	0.22 µm
60X	Silicon	1.3	0.22 µm	0.23 µm
60X	Water	1.2	0.23 µm	0.25 µm
40X	Dry	0.95	0.29 µm	0.32 µm
20X	Dry	0.75	0.35 µm	0.41 µm
10X	Dry	0.4	0.64 µm	0.76 µm
4X	Dry	0.16	1.57 µm	1.91 µm
2X	Dry	0.1	2.50 µm	3.05 µm

_____

Image resolution and image contrast are very important factors in an optical system. In a typical microscope such as a fluorescence microscope, contrast is determined by the number of photons collected from the specimen. There are many factors related to the signal-to-noise ratio for an image, such as lens aberrations, reflection at the edge of mechanical parts, the dynamic range of the signal, performance of the dichromatic mirror, and the cut-off level for the excitation and emission filters. Also, such things as the dynamic range of the detection system, pixel size and number of pixels of the imaging device are relevant factors as well. If the one component fails, then the imaging device gets unnecessary light, the contrast of image is reduced, and the image appears dimmer. It is essential to optimize the entire imagine system in order to attain a high-resolution/ high-contrast image.

Fourier optics

Fourier optics is thoroughly described by J. W. Goodman (Goodman (1968)). Our purpose here is to review Fourier optics' key points. When light goes across a sample, it makes diffraction. The diffracted light goes through the objective lens. A lower-numerical-aperture objective lens only passes zero order diffracted light but, high-order light will not pass through. A higher-numerical-aperture lens passes not only zero order, but one order, two order and more of the higher orders of diffraction light from the sample.

An important concept regarding image formation is that the nature of diffracted light rays from the sample intercepts from the circular edge of the objective lens aperture. Higher order diffracted rays experience interference at the edge of the objective and cannot be captured by objective. Then only light pass through and captured light recreates the image at the intermediate image plane of the optical system. A tube lens or eyepiece lens provides the intermediate image of the detection system, or eyepieces provide the image.

Large numerical apertures are an important part of the effort to create high-resolution images. The higher the numerical aperture of the objective, the higher the order of diffraction light, which results in needing a smaller Airy disk and ultimately provides a higher-resolution image. Lower-numerical-aperture objectives that transfer only lower-order diffraction light creates a bigger Airy disk, which provides a lower resolution image.

Light from the sample constructs a Fourier transform of the image (the field in the front focal plane) in the back focal plane of the objective lens. Spatial frequency is limited by the numerical aperture of the objective lens. Then the Fourier-transferred sample image is reconstructed on the image plane. The resulting image is usually low resolution because of the limited spatial frequency of the objective lens.

Real samples consist of many molecules, and light does not pass through only one point. The entire observation field of sample points passes through the objective and is reconstituted as an image.

_____

Airy disk

This section refers to theory described on the homepage of the Olympus Micro Primer:

 <URL http://www.olympusmicro.com/primer/anatomy/numaperture.html>.

Each point of the sample specimen projects to the image plane as a small-dot pattern known as an Airy disk pattern. The sample presents various distances of multiple-intensity points on the lateral surface on the specimen. However, these widely separated points are easily observed by the variation in image intensity on the lateral image plane.

During microscope observation, diffraction and scattering of sample light pass through the optical system and produce the image. This is the mechanism for the optical microscope. Sometimes, the size of the small, bright point that is being observed is smaller than the limit of optical resolution, such as a sub-micron-size fluorescent spherical bead. In this case, the light from the very small point goes thought the optical system and produces the image. This bright point is the Airy disk. Fig. A-4 shows Airy disks, which consist of small concentric light and dark rings. Airy disks and their intensity distributions as a function of separation distance are shown Fig. A-5.

The idea of the point spread function (PSF) is the three-dimensional diffraction pattern of a small light point source that transmitted from the objective lens. The pattern of light is a ringing pattern. The center of the ring has a bright dot and multiple rings of light surrounding the bright dot when viewed on the *x-y* surface of the image plane. This is the Airy disk. The maximum intensity of the central portion of the Airy disk and its multiple concentric rings of light correspond to intensity peaks in the distribution.

PSF intensity can be measured experimentally using a microscope. A sub-resolution-size fluorescence spherical bead is used as the specimen and the image is captured using a microscope with an extended-magnification lens. The intensity PSF is shown in Fig. A-5 (b). When considering the relationship between lateral resolution and contrast, it is critical to consider the lateral components of the intensity distribution of the Airy disk.

A smaller Airy disk provides more detail of the specimen; in other words, it provides a higher-resolution image. Objectives that have a higher numerical aperture and fewer aberrations produce smaller Airy disks. The key for obtaining higher-resolution images is to use the highest possible numerical aperture and lowest-aberration objective lens.

- 116 -
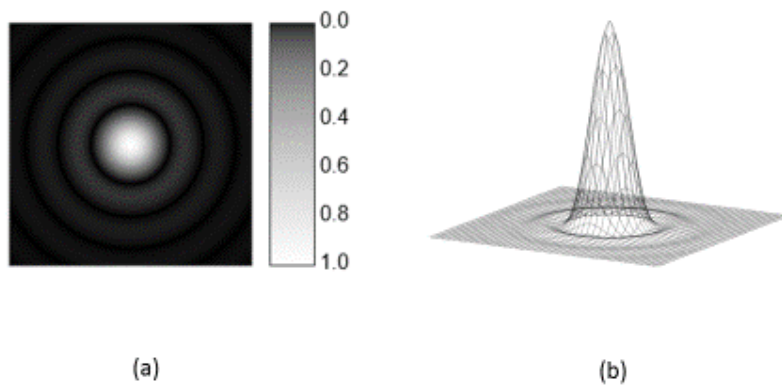
Fig. A-4. Airy diffraction patterns generated by computer simulation.

(a) A 2D Airy disk image

(b) A 3D model for the Airy Disk. The original figure is from Sakuranbo (Sakuranbo (2015)).
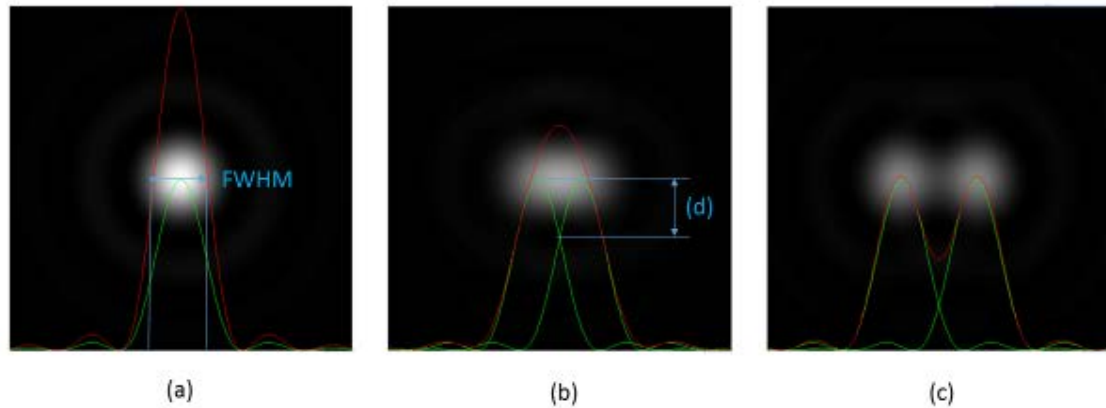
Fig. A-5. Airy diffraction patterns generated by light; Two points passing through a circular aperture (a, b, c). The original figure is from Hwang, Fu-Kwun (Hwang (2015)).

Fig. A-4 shows a computer-generated Airy disk (Sakuranbo provided image) that essentially consists of a diffraction pattern containing a central maximum. The result of Fraunhofer diffraction, the Airy pattern intensity distribution is created by the diffraction of light passing through a circular aperture. Moreover, a perfect optical system shows a central intensity maximum and higher-order maximum separated by regions of zero intensity. (However, the computer-generated image does not show higher-order light because higher-order light intensity is very weak.) The center of the picture shows a bright dot; this is called zero order. The pattern is surrounded by concentric one-order, two-order, three-order, and higher-order light. The intensity distribution of the order of diffracted light is decreasing as the order increases. At the zero crossing of the optical axis, the distance is normalized by the numerical aperture and wavelength.

Table A-3. An example of the distance between the zero crossings of the optical axis.

	Zero order	1 order	2 order	3 order	4 order
Distance	0	3.8	7.0	10.2	13.3
Intensity	100%	1.7%	0.4%	0.2%	0.08%

_____

An example of the intensity distributions of two Airy disks showing the limit of optical resolution is illustrated in Fig. A-5 (a). This figure was provided Hwang, Fu-Kwun. In this figure, the two disks exceed their radius, and these images are resolvable. The Rayleigh criterion often called the limit at two Airy disks resolved into separate entities. Fig. A-5 (c) shows two Airy disks and their intensity distributions in a situation where the intensity maximum to the maximum distance between the zeroth order.

_____

A2.   Confocal microscopy

The confocal microscope is widely used in many biological laboratories. Confocal microscopy provides high resolution and high-contrast images. The uniqueness of the confocal microscope is the way it uses a point of light to illuminate the sample and detect fluorescent light passing through a pinhole or slit. Confocal imaging provides higher contrast than conventional widefield fluorescence microscopy.

This section reviews the design of a confocal microscope optical system (A2.1) and theoretical concepts of the microscope optical system (A2.2).

A2.1.   Confocal microscope design

There are two basic types of confocal microscope. The first design is the laser scanning confocal microscope. A schematic drawing of the laser scanning confocal optical system is shown in Fig. A-6. The second type of confocal system is the disk scanning confocal microscope.

A laser scanning confocal microscope is more complicated than a conventional fluorescence microscope. It consists of two units: the microscope itself and the confocal unit, as shown in Fig. A-6. The microscope unit includes an objective lens and tube lens. These are the same as one would find in a conventional widefield microscope. Most researchers use commercially available microscopes, although some build custom-designed microscopes.

The confocal unit includes a laser, collimator lens, pinhole, lenses, excitation filter, galvano mirror, emission filter, pinhole and photomultiplier tube (PMT). The confocal system uses a collimated laser light source to create single-point sample illumination. Only the illuminated portion of the sample produces fluorescent light, and this fluorescent light goes through a pinhole, where a PMT detects the light. The galvano mirror provides the function of scanning the sample. Fig. 6 shows only one PMT, but most confocal systems have multiple PMTs to detect multicolor fluorescence.

The basic optical path for a laser scanning confocal microscope follows: In a confocal unit, the laser creates excitation light, the collimator lens is focuses the light, and the projection lens projects the laser light for infinity lay. The light passes through the dichromatic mirror, and the lens focuses it. The galvanometer mirrors stay in the projected position for the pupil position of the objective lens. The galvanometer mirror deflects the laser light onto the sample. The sample is excited by the laser light and provides emission light. The emission light returns to the objective lens, passes to the galvanometer mirror and goes to the dichromatic mirror, where it is reflected toward the pinhole. Out-of-focus emission light falls outside the pinhole and cannot pass through. Only focused emission light passes through the pinhole. Thus, only focused emission light enters the PMT and produces signal.
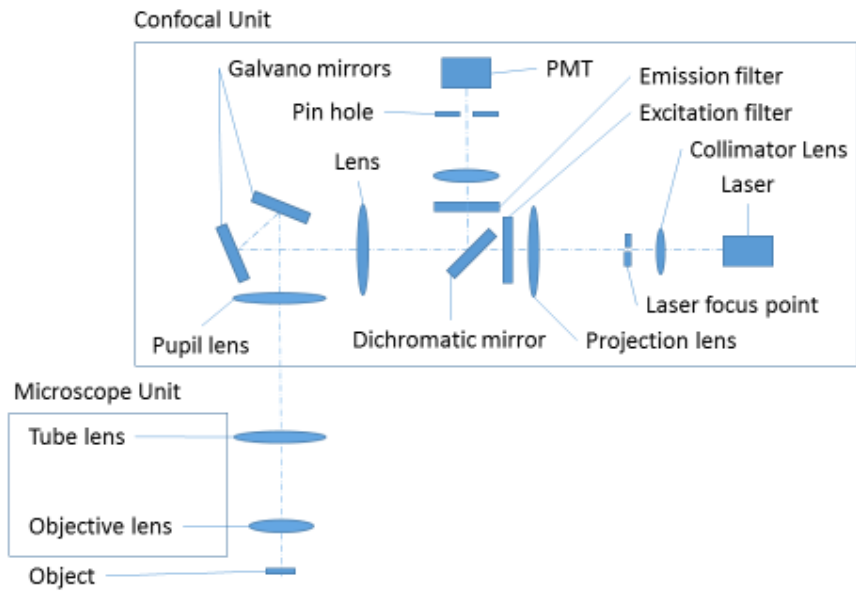
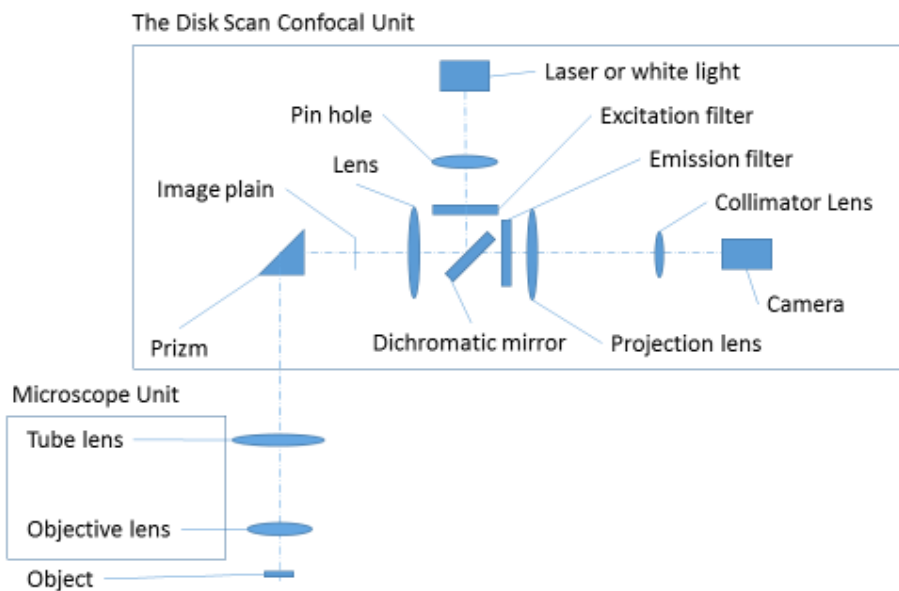**Fig. A-6. Laser scanning confocal microscope system.**

Fig. A-7. Disk confocal microscope system.

_____

Disk-based confocal systems work differently, and can provide faster acquisition times. They also are comprised of two units – the the microscope unit and the disk scan confocal unit, as seen in Fig. A-7. The microscope unit includes an objective lens and tube lens. These are the same as one would find in a conventional widefield microscope. Most researchers use commercially available microscopes, although some build custom-designed microscopes.

The disk scan confocal unit consist of a laser or white light source for creating excitation light and a collimator lens that collimates light, which passes through an excitation filter and is reflected by the dichromatic mirror before being focused to the disk. Disk scan confocal systems do not use a galvanometer mirror. Instead, the light goes through the confocal disk and creates multiple points of light on the sample. The sample is excited and creates multiple emission light that returns to the confocal disk. As light passes the confocal disk, all out-of-focus light is cut off so that only light that came from the area of focus on the sample continues to the emission filter. The emission filter cuts unnecessary wavelengths of light, so that only necessary light reaches the imaging device.

The imaging device for disk scan confocal is a camera, but in most cases is not a PMT. Most cameras used in this setup require high quantum efficiency and low noise. To achieve these conditions, the scientist uses a scientific-grade CCD or CMOS camera.

The disk scan confocal microscope requires a confocal disk. There are many types of systems with different types of disks. Some disks have multiple pinholes; others, instead of using pinholes, use vertical and horizontal lines. There is a disk that includes a micro-lens and pinholes available as well.

A2.2.   Resolution for confocal microscopy

This section references theory from the following homepages:

<URL http://www.olympusmicro.com/primer/techniques/confocal/resolutionintro.html>

<URL http://www.olympusconfocal.com/theory/resolutionintro.html>

The full-width half half-maximum (FWHM) of the point spread function is often used to measuring the Airy disk for confocal laser scanning microscopes. Normally, confocal imaging produces better resolution than conventional microscopy, but it is still proportional to the Rayleigh criterion. If we use the same numerical aperture objective lens, then the Airy disk size of the confocal fluorescence microscope is smaller than the widefield microscope Airy disk. Also, confocal imaging reduces the contrast cutoff distance. Moreover, the confocal microscope produces a higher-resolution image compared to the widefield microscope.

Regardless of the optical system, the lateral resolution has a proportional relationship to wavelength. Also, resolution has an inversely proportional relationship to the objective lens numerical aperture.

_____

Confocal microscopes are configured with point illumination and point detection systems so only the fluorophores located at the conjugate point of the illumination and detection for the pinhole are visualized. Point spread functions (PSF) can be detected from the confocal detection system. The intensity point spread function (IPSF) of a confocal system has two parts: illumination intensity and detection IPSF. In a confocal fluorescence configuration, the PSF is reduced by about 30 percent of the lateral distance of the widefield microscope, which means confocal microscopy increases lateral resolution by 30 percent.

Moreover, the axial extent of the PSF is reduced and provides an optically sectioned image that the widefield microscope cannot provide. Widefield microscopes can provides out-of-focus images even without changing the focus point. The confocal pinhole cuts out out-of-focus light. Confocal provides a narrower IPSF, the separation of two points required to produce acceptable contrast in the confocal microscope. The formula for lateral resolution is shown below:

$$r_{lateral} = 0.4 \ \times \frac{\lambda}{NA} \qquad\qquad \text{(A2.1)}$$

The above estimation is based on using two very small dots that illuminate incoherently in all directions. The diffraction of light limits the NA. Table A-4 shows sample objectives with specifications and confocal lateral resolution..

Table A-4. Popular objectives specifications & confocal lateral resolution. Used $\lambda=500\ nm$.

Magnification	Type	N.A.	Working Distance	$r_{lateral}$
100X	Oil	1.4	0.13 mm	0.22
60X	Silicon	1.3	0.13 mm	0.23
60X	Water	1.2	0.28 mm	0.25
40X	Dry	0.95	0.18 mm	0.32
20X	Dry	0.75	0.6 mm	0.41
10X	Dry	0.4	3.1 mm	0.76
4X	Dry	0.16	13 mm	1.91
2X	Dry	0.1	8.5 mm	3.05

_____

Fig. A-7 presents the axial intensity distributions for a typical widefield (Fig. A-7 (a)) and confocal (Fig. A-7 (b)) fluorescence microscope. Note the conventional fluorescence PSF has "wings" (Fig. A-7(a)) and the confocal PSF has removed the "wings" (Fig. A-7 (b)). The confocal pinhole removed the "wings" from the PSF. The original image is from Fellers and Davidson, Resolution and Contrast in Confocal Microscopy (Resolution and Contrast (2015)).
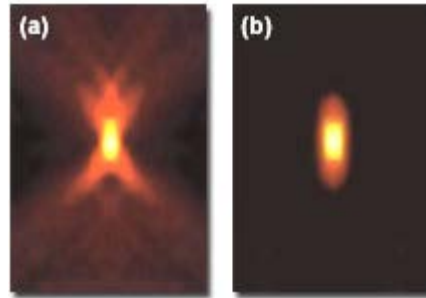
Fig. A-7. Axial PSF intensity profiles. (a) Fluorescence microscope. (b) Confocal microscope.

The original image is from Fellers and Davidson, Resolution and Contrast in Confocal Microscopy (Resolution and Contrast (2015))

The axial resolution of the confocal microscope is given below, with η representing the index of refraction, and the other variables as specified:

$$r_{axial} = 1.4 \; \frac{\lambda \times \eta}{NA^2} \qquad \text{(A2.2)}$$

The actual advantage of the confocal microscope is in its optical sectioning capability. The confocal microscope improves the axial resolution over that achievable with a widefield microscope. This function is helpful for observing thick specimens.

The IPSF of the conventional widefield microscope is a conjugate of the focused image overlapped with the out-of-focus image. Therefore, conventional microscopy does not produce an optically sectioned image. However, the optical sectioning properties of the confocal microscope arise from the size of the integrated IPSF, which has a maximum in the focal plane and reduces out-of-focus data. As a result, axial resolution when using confocal systems offers a dramatic improvement over conventional microscopy.

However, there are many practical restrictions to getting maximum performance out of any

_____

optical system, and resolution is always limited by the diffraction limit. Therefore, attaining optimum conditions for confocal imaging is critical for keeping the signal-to-noise ratio as high as possible.


Nyquist theorem

This section refers to theory listed on the Olympus Primer Confocal homepage:

<URL http://www.olympusmicro.com/primer/techniques/confocal/resolutionintro.html>

The Nyquist Theorem sheds light on a key aspect of image sampling. It specifies the sampling interval required to reconstruct a pure sine wave faithfully as a function of its frequency. The performance of the optical system can be measured by the contrast transfer function (CTF), signal-to-noise statistics, and the entire process in which the signal is sampled for digitization.

Nyquist sampling theory is usually explained in the spatial frequency domain rather than the real size of the object. A sample image consists of 2D distribution for intensity. This means the intensity is distributed in the *x, y* plain. Considering Nyquist theory, the sample specimen feature is transferred to the spatial frequency domain. This means the image intensity can transfer to several sine waves of varying frequency, then inverse the spatial frequency domain to the real domain and creating the sample image. Use of the spatial frequency domain is part of evaluating the performance of optical systems. Their ability to maintain contrast and resolution is same as the transfer of image information of different frequencies. Optical systems reduce contrast and resolution because the numerical aperture is limited and the optical system has slight errors in design and manufacturing. The effect of the reduction is more severe for higher spatial frequencies than for lower frequencies.

The contrast transfer function (CTF) of an optical system is used to create a periodic test pattern chart. The periodic test pattern chart consists of the black line and clear transmitted line at a wide range of frequency patterns. Fig. A-8 illustrates a hypothetical CTF for an optical system. Moreover, it includes curves indicating system response to a test target having black and white bars.
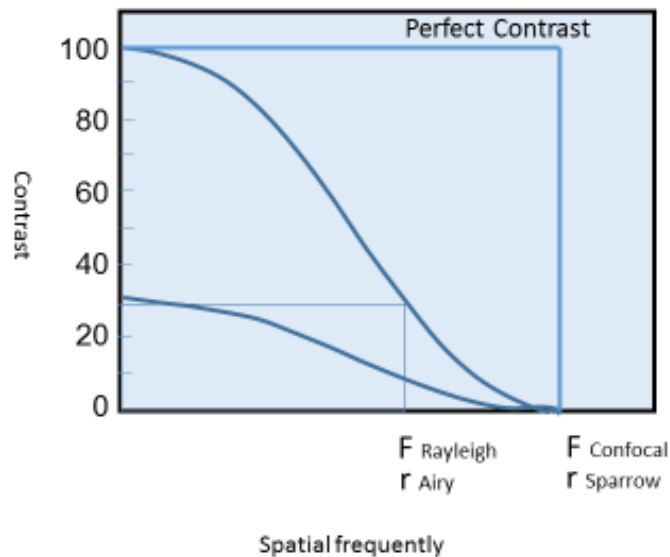
Fig. A-8. Specimen spatial frequency and contrast.

The original image is from Fellers and Davidson, Resolution and Contrast in Confocal Microscopy (Resolution and Contrast (2015))

Examination of the contrast transfer function curves of Fig. A-8 clearly illustrates the interdependence of resolution (vertical axis) and contrast (horizontal axis), and the problem of some common assumptions that are made. The image resolution is related to instrument performance (numerical aperture, errors, etc.). When defined as the highest spatial frequency that produces a certain image contrast, it is easily assumed that any features having frequencies within the stated resolution limit are equally visible. However, in fact, the sample specimen is more clearly visible than the original contrast for every frequency up to the contrast cutoff frequency. The transfer function curves (Fig. A-8) illustrate that specimen feature. Initially there is about 30% contrast due to staining characteristics or another factor. The Rayleigh limit assumes equal contrast at all frequencies up to the resolution limit that specified 26% contrast level at spatial frequencies near the theoretical limit, but it would not maintain. The contrast of small features that high-frequency images are slightly within the resolution limit produces contrast much lower than that of larger features after each has been degraded by the transfer function of the imaging system.

Nyquist said that for a sampling system to faithfully reconstruct a pure sine wave it must be

_____

sampled at least twice during each cycle of the wave, or sampled at two-times the temporal frequency. The Nyquist theorem usually applies to spatial imaging. The minimum sampling frequency employed in microscopy imaging applications is usually 2.3 times the maximum frequency to be reconstructed. The value of 2.3 is used as a practical matter to compensate for the low-pass filtration that is required for perfect image reconstruction in real optical systems.

_____

A3.   Total internal reflection fluorescence

This chapter presents the process of Total Internal Reflection Fluorescence (TIRF) and introduces the properties of light associated with the evanescent field. For the microscopy techniques presented in this appendix, the evanescent field constitutes the illumination. Here, Huang published an excellent TIRF article, so I refer to his article to explain the basis of TIRF microscopy (Huang, Peter et al. (2006)).

A3.1. Design for total internal reflection fluorescence microscope

The TIRFM is often used in biological research. There are two types of TIRFM commonly used. These are the objective illumination TIRFM and the prism illumination TIRFM. Prism illumination TIRFM (Fig. A-9 (a) uses a prism for the illuminator. Illumination light enters the prism and makes an evanescent wave between the prism and sample. This prism-type TIRFM can accept any objectives but working distance is a key factor because the brightest illumination point is the bottom surface of the prism, which is relatively far from the objective lens.

Objective illumination TIRFM (Fig. A-9 (b) requires objectives with NAs at or greater than 1.40. There are several objectives available in the market that meet this criterion (see table A-5).
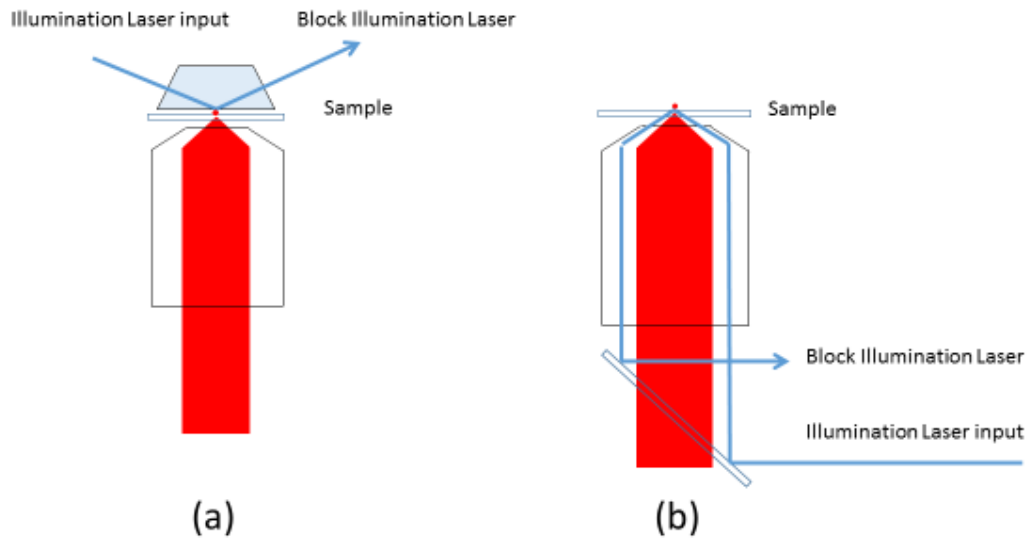
Fig. A-9. Two types of TIRFM microscopy.

Table A-5. The list of TIRFM applicable objectives.

| Magnification	Type	N.A.	Working Distance
150x	Oil (n=1.515)	1.45	0.08
100x	Oil (n=1.78)	1.7	0.08
100x	Oil (n=1. 515)	1.49	0.1
60x	Oil (n=1. 515)	1.49	0.1
60x	Oil (n=1. 515)	1.42	0.12
60x	Oil (n=1. 515)	1.4	0.15

A3.2. Total internal reflection fluorescence

TIRFM applications have been well explained by Axelrod (Axelrod (1981, 1990)). In summary, an evanescent field is created at the solid surface interface between two different indices (figure A-1).

When a wave of light enters the interface between two media with different refractive indices, it refracts and changes direction according to Snell's law (Goodman (1968)). The refractive indexes of n_i and n_t are the refractive indexes of the incident medium and transmitting medium. If a wave of light hits the interface under an angle greater than the critical angle θc, it reflects and undergoes Total Internal Reflection (TIR). It occurs when the exit angle in the transmitting medium, $θ_t$, becomes *90◦*. Using Snell's law the critical angle is then described by

$$\theta_c = arcsin\left(\frac{n_t}{n_i}\right) \qquad \text{(A3.1)}$$

Due to the boundary conditions set by Maxwell's equations a thin evanescent field will form in the transmitting medium right at the interface (Axelrod (1981, 1990)). The situation is illustrated in Fig. A-10, where a plane wave with wave vector **k**i undergoes TIR, and the parallel wave fronts of the evanescent field are drawn in the transmitting medium.

_____
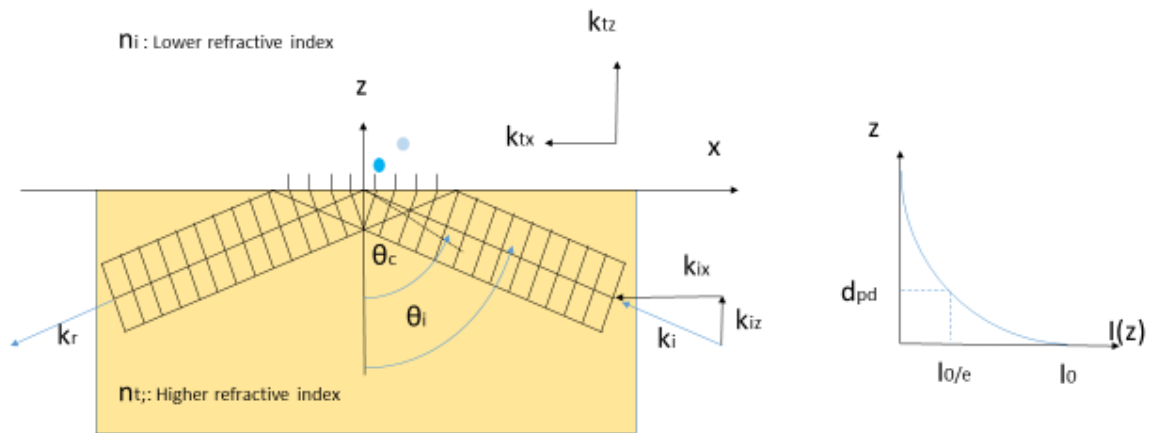
Fig. A-10. Scheme for Total Internal Reflection (TIR) at two different refractive indexes plane interface. OLSHAUSEN, Philipp von (2013)

A plane wave incident under the angle $\theta i > \theta c$ (critical angle for TIR) with the wave vector ki is totally internally reflected at a plane interface with refractive indices $ni > nt$. All intensity is reflected (Kr), but an evanescent field penetrates into the transmitting medium. To the left, the axial decay of the intensity is shown.

The following explanations are restricted to the *x-z*-plane (lateral direction) as shown in Fig. A-10 but are equally applicable to three dimensions. The components of the wave vector of the evanescent field depend on the incident wave vector ki and the indices of refraction of the two media. From Maxwell's equations, it can be deduced that the tangential component of the electric field at an interface is conserved (Axelrod (1981, 1990)). Thus, the tangential component of the evanescent field vector, ktx, is given by

$$k_{tx} = k_{ix} = k_0 \cdot n_i \cdot sin(\theta_i) \qquad \text{(A3.2)}$$

Where θi is the angle of incidence as shown in Fig. A-10. Equation A3.2 defines the wavelength of the evanescent wave, λev, traveling along the interface by

_____

$$\lambda_{ev} = \frac{\lambda_0}{n_i \cdot sin(\theta_i)} \qquad \text{(A3.3)}$$

The axial *(z)* component of the wave vector of the evanescent field, *ktz*, can be deduced from the condition

$$k_t^2 = k_{tx}^2 + k_{tx}^2 \qquad \text{(A3.4)}$$

Which result in

$$k_{tz} = {}_\perp\sqrt{k_t^2 \, k_{tx}^2} \qquad \text{(A3.5)}$$

Moreover, thus,

$$k_{tz} = -ik_0 \sqrt{n_i^2 \cdot sin^2(\theta_i - n_t^2)} \qquad \text{(A3.6)}$$

Here, *kt* = *nt* · *k0* is the wave vector in the transmitting medium. Equation A3.6 reveals that *ktz* is imaginary for *θi* > *θc*. Consequently, the evanescent electric field is described by

$$\mathrm{E}(x, z \geq 0) = E_0 \cdot e^{k_{ie} \cdot z} \cdot e^{tk_{ix} \cdot x} \qquad \text{(A3.7)}$$

This field travels along the interface and decays exponentially in the axial direction.

From equation A3.7, it follows that the evanescent wave intensity also decays exponentially in the axial direction that can be expressed by

_____

$$I(z \geq 0) = I_0 \cdot e^{-\frac{z}{d_{pd}}} \qquad \text{(A3.8)}$$

Where $I(0)$ is the light intensity at the interface and p is the evanescent wave penetration depth. The evanescent wave penetration depth p can be calculated from where $\lambda(0)$ is the wavelength of the incident light. The θ is the beam incident angle, and n_1 and n_2 are the indices of refraction of the solid and liquid, respectively.

$$d_{pd} = \frac{\lambda_0}{4\pi \sqrt{n_i^2 \cdot sin^2(\theta_i) - n_t^2}} \qquad \text{(A3.9)}$$

At a distance $z = d_{pd}$ from the interface the intensity has dropped to $I0/e$. The axial decay of the evanescent intensity is illustrated in the right part of Fig. A-10.
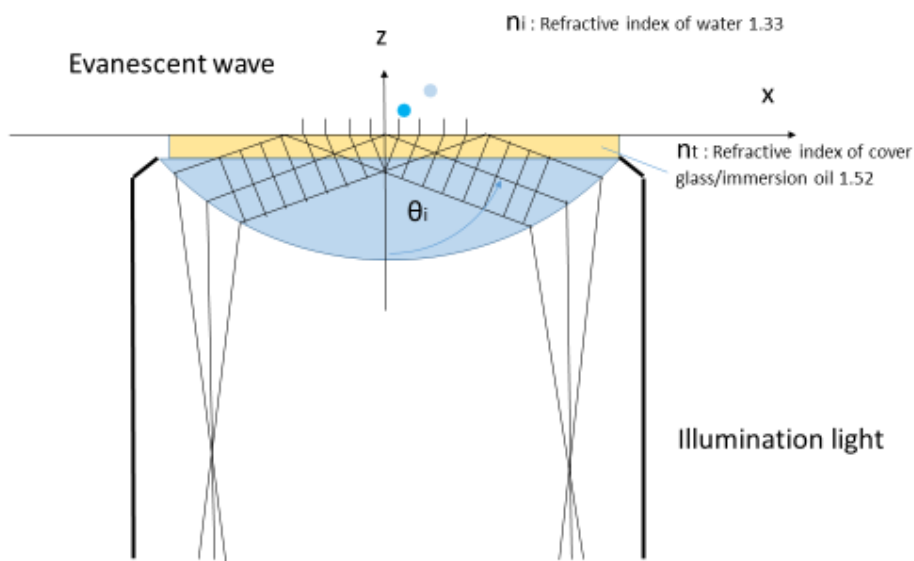
Fig. A-11. Objective-based total internal reflection fluorescence microscopy.

_____

Analysis of fluorescent particles

The methods of measurement of fluorescent beads (particles) using TIRFM were described by Kihm and Huang. The detection of emission for fluorescence beads includes some tolerances. Factors include statistical variations in illumination intensity, quantum effciency of the imaging system and distribution of the physical size of the particles. Parameterize all of these variations by an 'effective emission radius', r, the model the fluorescent bead's probability density function (PDF) of its effective emission radius with a Gaussian distribution is

$$\text{p(r)} = P_0 exp\left[-\frac{\left(\frac{r}{a}-1\right)^2}{\sigma_r^2}\right] \qquad \text{(A3.10)}$$

where *a* is the mean effective emission radius of the batch, *P0* is a normalization constant, and **σr** is the characteristic variation (standard deviation). This formula is using based on the calculation of *Kihm* et al. (2004) and the assumption that the emitted light intensity of a fluorescent bead is proportional to the number of fluorophores within its volume. The emission light intensity, **Ie**, of a particle in an evanescent field is

$$I^e(r,h) = \left(\frac{r}{a}\right)^3 \left[I_0^e e^{-(h-a)/d}\right] \qquad \text{(A3.11)}$$

where *h* is the distance from the fluorescent bead's center to the substrate surface at which total internal reflection occurs. *I^e* is the emitting light intensity of a single fluorescent bead with **r = a** located at **h = a** (i.e. distance from the substrate surface). Also, *d* is an intensity decay length that is not the same as the evanescent penetration depth. The length of intensity decay can be obtained experimentally by statistically measuring the fluorescent bead intensities. This fluorescent bead intensity is a particle distance from the substrate. As when fluorescent beads tracer are imaged, combining (A3.10) and (A3.11) gives the joint PDF of the emitted intensity and a fluorescent bead's distance to the substrate.

$$P(I^e,h) = \alpha \exp\left\{\frac{\left[\sqrt[3]{(I^e/I_0^e)e^{(h-a)/d}}-1\right]^2}{\sigma_r^2}\right\} \qquad \text{(A3.12)}$$

_____

The bead is located at a range of distances h from the substrate surface. A fluorescent bead touching the substrate surface is the lower limit of this imaging range. This is represented by $h = a$. The sensitivity of the detector such as an intensified CCD camera or cooled camera determines the upper limit of the imaging range. For a given imaging range of $h_1 < h < h_2$, the PDF of a fluorescent bead tracer 's intensity is given by

$$P(I^e, h_1 < h < h_2) = \int_{h_1}^{h_2} P(I^e, h)c(h)dh \qquad \text{(A3.13)}$$

where $c(h)$ is the concentration profile of fluorescent beads in the fluid. For low variation in effective emission radius (σr small), the fluorescent beads in the defined imaging range are sharply defined in intensity, with the brightest fluorescent beads located on the surface ($I^e/I^e = 1$). Also, the faintest fluorescent beads are on the outer edge of the evanescent field ($I^e/I^e = 0.2$). However, as the variation in fluorescent bead radius increases, the transitions become more blurred. Also, some larger fluorescent beads close to the wall contribute to the long tail at high observed intensities, whereas small fluorescent beads close to the edge of the imaging range are represented by a smooth transition close to $I^e/I^e = 0$.

When performing image analysis, however, one need not analyze all imaged fluorescent beads. Instead, using fluorescent bead intensity as a guide, one can choose to identify and analyze only the fluorescent beads within a certain desirable intensity range, ignoring fluorescent bead position distribution within a normalized intensity range of $\alpha < I^e/I^e_0 < \beta$ by

$$P\left(h, \alpha < \frac{I^e}{I_0^e} < \beta\right) = c(h) \int_{\alpha}^{\beta} P(I^e, h)d\left(\frac{I^e}{I_0^e}\right) \qquad \text{(A3.14)}$$

_____
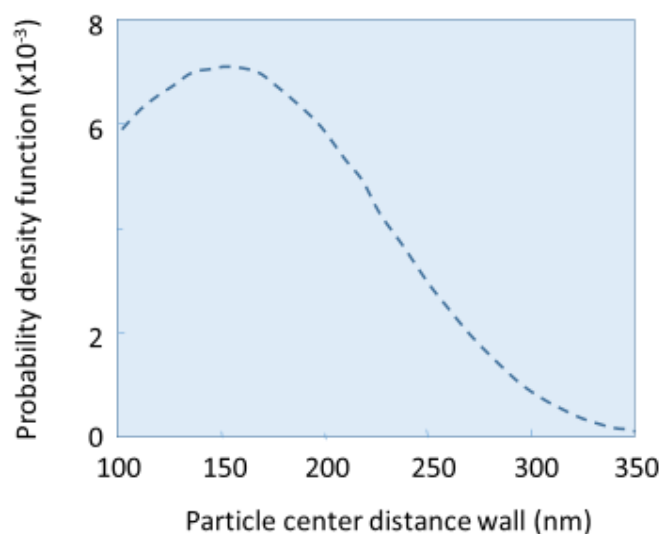
Fig. A-12. The predicted position distribution of particles with $0.5 <$ $I^e/I^e < 1$ in a uniform concentration field

In this prediction, $a = 100\,nm$, $d = 181\,nm$ and $\sigma r = 0.18$. This drawing is from originally from Huang (2006)).

An example of the position distribution fomula described here (A3.12) is shown in figure A-13 for a normalized intensity range of $0.5 < I^e/I^e < 1$. The most obvious feature is that the distribution is non-uniform with the majority of fluorescent beads contributing to this range of intensities coming from close to the substrate surface ($<250\,nm$). Also, the distribution has a long positive tail that gradually decays to zero far away into the fluid bulk because of the large-fluorescent bead effective radius variation in this example. A large fluorescent bead far away (for example, $>300\,nm$) can exhibit the same fluorescence intensity as that of smaller fluorescent beads close to the substrate surface. These observations reinforce the concept that a particle's intensity cannot be monotonically related to its distance to the solid surface. Moreover, attention should be given to any intensity-based quantitative analysis by recognizing the non-uniform position distribution and the contribution of fluorescent beads far away from the wall.

_____
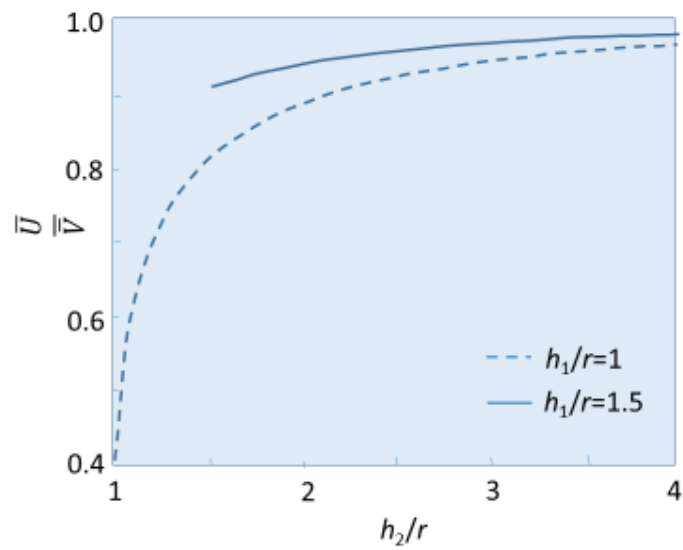
Fig. A-13. The ratio of the statistical apparent velocity of particles (mean fluid velocity) under no slip in an imaging range of $h_1 < h < h_2$, which is non-dimensionalized by particle radius.

$\bar{V}$ is computed with linear fluid velocity profile, which is a good approximation near a surface. In the computation of $\bar{U}$, $c(h)$ is assumed to be uniform. This original drawing is from Huang (2006)).

_____

A4. Darkfield microscopy

This section refers to theory found on the following homepages:

<URL http://www.olympusmicro.com/primer/techniques/darkfield.html>

<URL http://public.wsu.edu/~omoto/papers/darkfield.html>.

Stars are shining both night and day. But while the visibility of stars on a dark night is excellent, it is extremely difficult to observe stars during the daytime. The only difference is the brightness of the background. When the background of an object is darker, then it is easy to detect the object, whether it is a star or a small dark microscopic sample. To make a high-contrast image, having a dark background can be a critical factor.

This section presents the properties of darkfield microscopy. Darkfield microscopy uses a dark background to increase the contrast of the image. In general, objects imaged under proper conditions of darkfield illumination are quite spectacular to see. Often specimens that contain very low inherent contrast when observed in brightfield microscopy shine brilliantly in darkfield. Darkfield illumination also is one of the best methods for revealing outlines, edges, boundaries, and refractive index gradients.

During the early 20th century, histology became a crucial research method for the biological samples and darkfield microscopy became a strong research tool at that time. Scientists spent great effort expanding and optimizing darkfield condensers and illuminators. But over tide, this intense interest began to fade. After that, other advanced contrasting-enhancing techniques such as phase contrast, differential interference contrast, and Hoffman modulation contrast were developed and became the first choice of many scientists. Recently, a renewed interest in darkfield microscopy has arisen due to its advantages when used in combination with fluorescence microscopy.

Darkfield microscopy is the one of the most powerful label-free imaging methods. Even when the sample is labeled with fluorescent molecules, darkfield microscopy is still useful for label-free observation and imaging of the sample structure. Importantly, darkfield microscopy also is easy to add to existing microscopes and is one of the highest-sensitivity imaging methods, with its simple design and ease of implementation.

Darkfield microscopy is an excellent tool for both medical and biological investigations. It can be used effectively at high magnifications for observing such organisms as bacteria, cells, tissues. Darkfield imaging is still widely used in research because it provides a high-resolution image, particularly for observing the structure of the sample. The schematic drawing (Fig. A-14) is an example of fluorescence illumination (a), darkfield illumination (b), and brightfield illumination (c). When using either fluorescence or brightfield microscopy, darkfield microscopy is often able to

complement the other technique and provide information from the sample that the other method missed.
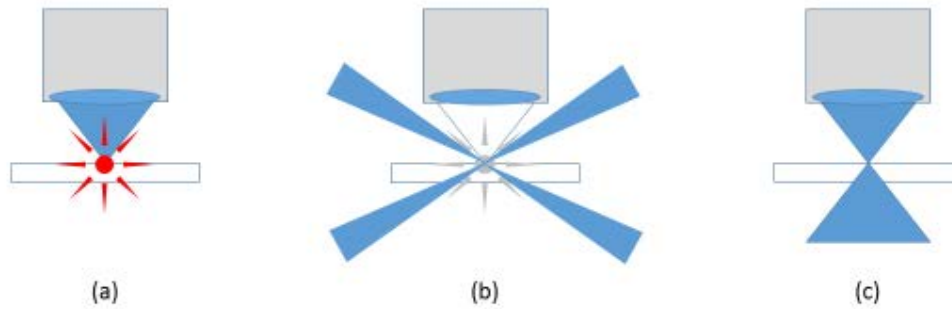

Fig. A-14. An example of observation methods. (a) fluorescence illumination, (b) darkfield illumination, (c) and brightfield illumination.

A4.1.   Theory of darkfield microscopy

In darkfield, only oblique illumination light entering from various azimuths around the center enters the observation area and the illumination light does not get back into the objective to be imaged. Thus, the background of the image field is dark, and only bright data coming from areas where scatter is caused by index mismatch is provided. Such areas might include cell membranes, nuclei and other surfaces where a mismatch might occur between the specimen and the background.

Contrast can be extremely high because diffraction light from the sample can be detected as an image against a dark background. The image typically consists of bright points or lines. Even if the diameter of the scattering object is smaller than the microscope's limit of resolution, the image may be detected as small objects that are not observable by brightfield microscopy can be observed in darkfield.

Darkfield microscopy is a simple and easy observation method for making unstained,

_____

transparent specimens visible. The sample objects often have a little absorption and small refractive-index-value differences between the sample and its surrounding area. For instance, many cells are difficult to see in detail in brightfield, but have a refractive index ranging from 1.2 to 1.4, resulting in a refractive index mismatch between the medium and sample.

There are many different darkfield illumination designs available. Rather than illuminating the sample specimen with a filled cone of light, the condenser is designed to produce a hollow cone of light (a kind of ring light). The light at the apex of the cone is focused at the plane of the specimen. After passing the sample specimen, this light spreads again into a hollow cone. The objective lens sits in the dark hollow of this cone. The illumination light passes through the sample and does not enter the objective lens. Light just passes around the objective lens. (Fig. A-15 (b)).

If a darkfield microscope has a no sample on the stage, then the entire image is dark (hence its name). When a sample specimen is on the stage, the light at the apex of the cone strikes the sample. The image is made only by those rays scattered by the sample and captured in the objective lens. A bright sample image appears against a dark background. The advantage of darkfield microscopy also can be its disadvantage; not only the sample, but dust and other light-scattering entities also can be prominently observed.
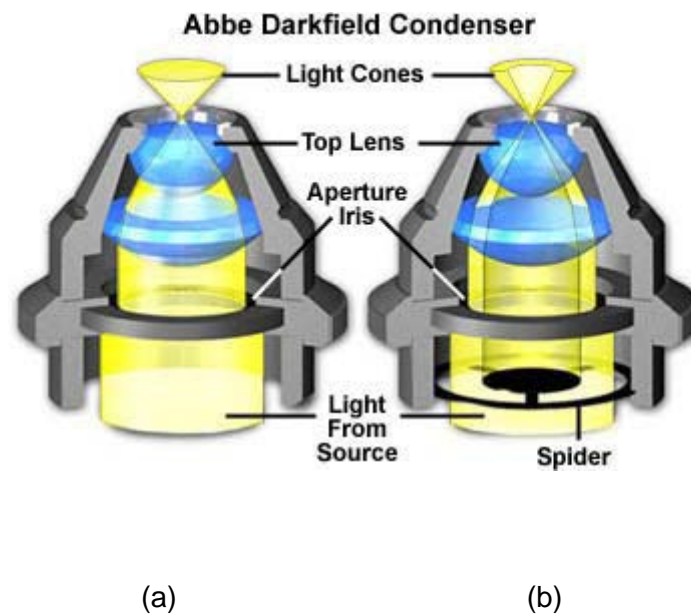
Fig. A-15. Brightfield illumination condenser (a) and darkfield condenser (b). The original image is from Davidson, Darkfield Illumination (Darkfield Illumination (2015))

Darkfield illumination requires using only oblique illumination rays. One of the examples is the Abbe darkfield condenser. This condenser lens has a spherically concave shape. This design allows light rays emerging from the surface in all azimuths

_____

to form an inverted hollow cone of light with an apex centered in the specimen plane. If no specimen is present, and the numerical aperture of the condenser is greater than the objective lens, the oblique rays cross, and all such rays will miss entering the objective lens because of their obliquity. The field of view will appear dark.

When an unstained and non-light absorbing sample on the slide glass is placed on the microscope stage, the oblique illumination rays cross the specimen and are scattered, diffracted, reflected, and refracted by optical discontinuities such as the granules, cell membrane, nucleus, and internal organelles, etc., allowing these faint rays to enter the objective. The scattered points or lines appear bright on a dark background.

Regarding Fourier optics, darkfield illumination removes the zeroth order (unscattered light) from the diffraction pattern formed at the objective lens back focal plane. Only higher orders of light pass into the imaging system. The result is an image formed exclusively from higher-order diffraction rays of light from the sample specimen.

Fig. A-16 illustrates the same point made earlier about viewing stars during the daytime. As seen in Fig. A-16 (b), visibility is extremely enhanced by the contrast between a brightly shining specimen and its dark background. As discussed above, the opaque stop for the darkfield condenser has blocked all the zero order rays. Oblique rays, now diffracted by the specimen, are yielding first, second, and higher diffracted orders at the rear focal plane of the objective. They proceed on the image plane where they interfere with one another to produce an image of the specimen.

(a) (b)

**Fig. A-16. Image of non-stained live cheek cells**

(a) Brightfield image, (b) Darkfield image.

_____

Fig. A-16 visualizes the effects of darkfield and brightfield illumination when observing non-stained live cheek cells with water. In an ordinary brightfield image (a), aperture stop open, the structure of cheek cells is not well observed because the image contrast is minimal. In the darkfield image (b), the structure of cheek cells is well observed because the image contrast is very high.

Darkfield microscopy at high magnifications

Using high-numerical-aperture reflecting condensers (Fig. A-18 and Table A-6) with darkfield illumination is the method of choice for observing and imaging very small particles or colloidal suspensions. The method can even be used when particle diameter is significantly lower than the limit of resolution of the objective because light, diffracted by the particles, passes through the objective and becomes visible as a bright diffraction disk. Each particle is visible as a minute diffraction disk, provided the lateral distance between neighboring particles is greater than the limit of the resolving power of the objective. As darkfield illumination intensity is increased, the optical difference between minute diffracting particles and their background light increases. Simultaneously, even smaller particles (detectable solely by their ability to scatter light) now diffract enough light to become visible and suspended particles can be seen even when their diameters are smaller than 40 nanometers. Which is about one-fifth the 200-nanometer resolution limit with oil immersion of the highest-numerical-aperture objective. In biological applications, the movements of living bacterial flagella that average about 20 nanometers in diameter can be observed. This size is too small to be seen in brightfield or DIC illumination. Moreover, high-numerical-aperture objectives requires high-numerical-aperture darkfield condensers.

For more precise work, if a darker-background-image is needed, the researcher may choose a condenser exclusively designed for the darkfield condenser, i.e. to transmit only oblique rays. There are several varieties: "dry" darkfield condensers with air between the top of the condenser and the underside of the slide; oil-immersion darkfield condensers that require the use of a drop of immersion oil; or water immersion condensers. The top of the condenser must contact the underside of the specimen slide. The oil immersion darkfield condenser has internal mirrored surfaces and passes rays of high obliquity. Also, its mirror is free of chromatic aberration, producing the best results and blackest background.

_____
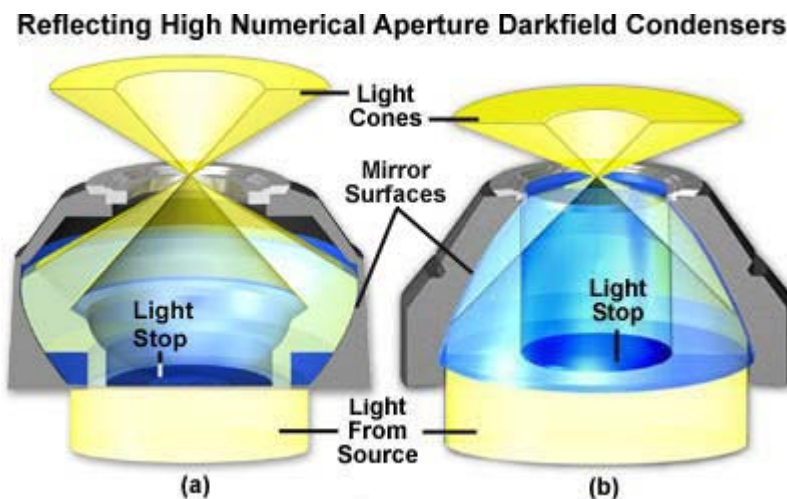
Fig. A-17. Reflecting high NA darkfield condenser. The original image is from Davidson, Darkfield Illumination (Darkfield Illumination (2015))

As discussed above, the dry darkfield condenser is useful for objectives with numerical apertures below 0.75 (Fig. A-15), whereas the paraboloid and cardioid immersion condensers (Fig. A-17 (a)) can be used with objectives of very high numerical aperture (up to 1.4) such as an oil immersion condenser. Objectives with a numerical aperture above 1.2 will require some reduction in their working aperture since their maximum numerical aperture objectives may exceed the numerical aperture of the condenser, thus allowing direct light to enter the objective. For this reason, many high-numerical-aperture objectives are designed for use with darkfield as well as brightfield illumination. Typically condenser lenses and some objectives come with a built-in adjustable iris diaphragm that acts as an aperture stop. This reduction in numerical aperture also limits the resolving power of the objective as well as the intensity of light in the image.

Table A-6 lists several properties of the most common reflecting high-numerical-aperture darkfield condensers. This table may be used as a guide when selecting condenser/objective combinations for use with high-numerical-aperture darkfield applications.

_____

Table A-6. High-numerical-aperture darkfield condenser specifications. The
original table is from Davidson, Darkfield Illumination (Darkfield Illumination (2015)).

Condenser Type	Hollow Cone Numerical Aperture	Objective lens Numerical Aperture	Number of reflecting Surfaces
Paraboloid	1.00-1.40	Less than 0.85	1 Parabolic
Cardioid	1.20-1.30	Less than 1.05	1 Spherical 1 Cardioidal
Bicentric	1.20-1.30	Less than 1.05	1 Cardioidal 1 Spherical
Bispheric	1.20-1.30	Less than 1.05	2 Spherical
Cassegrain	1.40-1.50	Less than 1.30	1 Aspheric 1 Spherical
Spot Ring (Bicentric)	1.40-1.50	Less than 1.30	2 Spherical
Nelson Cassegrain	1.30-1.45	Less than 1.20	1 Aspheric 1 Spherical

The condensers listed at Table A-6 cover a wide range of optical designs used to
produce the oblique hollow cone of light necessary for high-magnification darkfield
microscopy. Fig. A-18 shows an example of one - high-NA darkfield condenser called
the Bispheric double reflecting condenser.

_____

Bispheric Double Reflecting Condenser
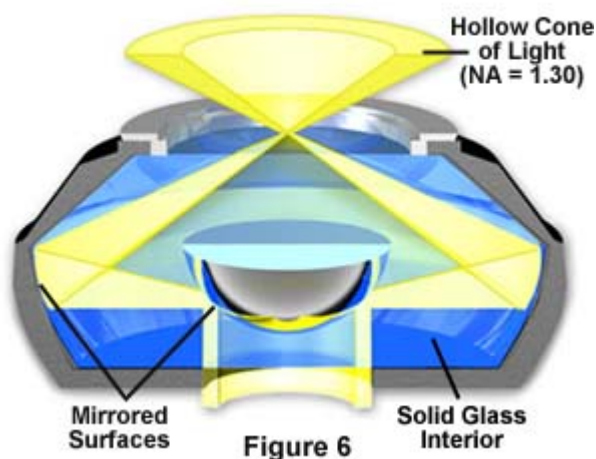
Fig. A-18. Bispheric double reflecting condenser.

The original image is from Davidson, Darkfield Illumination (Darkfield Illumination (2015))

Standard brightfield microscopy relies on light from the light source being gathered by the substage condenser and its rays being shaped into a cone whose apex is focused at the specimen plane.

Specimens are seen because of the refractive index mismatch, or areas where opacity produces refractive or scattered light from the specimen. When observing samples using a brightfield microscope, the light rays pass through the sample and the sample provides zero-order, 1st-order, 2nd-order and higher-order diffraction light. However, the sample has different absorption for different positions and if the objective lens passes most of the light then it will produce different parts of the image with different colors or intensities. If the specimen has no absorption and it has a refractive index too similar to the surrounding medium, it will not be seen. To observe a biological material using darkfield, the material must have this inherent contrast caused by the changes in refractive index as light moves through the specimen. These limitations require observers to find different refractive-index mounting media or to use appropriate fixation methods to enhance image contrast. Adequately visualizing transparent living materials such as cells or thin unstained tissue slices is difficult when using a brightfield microscope.

References in appendix

Abbe, Ernst. "Beiträge zur Theorie des Mikroskops und der mikroskopischen Wahrnehmung." Archiv für mikroskopische Anatomie 9, no. 1, 413-418 (1873).

Abramowitz, Mortimer, Kenneth R. Spring, H. Ernst Keller, and Michael W. Davidson. "Basic principles of microscope objectives." Biotechniques 33, no. 4, 772-781(2002).

Angular resolution - Wikipedia, the free encyclopedia. http://en.wikipedia.org/wiki/Rayleigh_criterion [accessed May 29, 2015].

Axelrod, Daniel. "Cell-substrate contacts illuminated by total internal reflection fluorescence." The Journal of cell biology 89, no. 1, 141-145 (1981).

Axelrod, Daniel. "Total internal reflection fluorescence at biological surfaces." Modern cell biology 9, 93-127 (1990).

Born, Max, and Emil Wolf. Principles of optics: electromagnetic theory of propagation, interference and diffraction of light. Cambridge university press (1959).

Darkfield Illumination - Olympus Microscopy Resource Center. http://www.olympusmicro.com/primer/techniques/darkfield.html [accessed May 31, 2015].

Davidson, Michael W., and Mortimer Abramowitz. "Optical microscopy." Encyclopedia of imaging science and technology (2002).

Depth of Field Calculator - Nikon MicroscopyU. http://www.microscopyu.com/tutorials/java/depthoffield/index.html [accessed May 03, 2015].

Goodman, Joseph W. Introduction to Fourier optics. Vol. 2. New York: McGraw-hill (1968).

Huang, Bo, Mark Bates, and Xiaowei Zhuang. "Super resolution fluorescence microscopy." Annual review of biochemistry 78, 993 (2009).

Huang, Peter, Jeffrey S. Guasto, and Kenneth S. Breuer. "Direct measurement of slip velocities using three-dimensional total internal reflection velocimetry." Journal of fluid mechanics 566, 447-464 (2006).

Hwang, Fu-Kwun. "Optical Resolution Model." ttp://www.compadre.org/Repository/document/ServeFile.cfm?ID=8198&DocID=866 [accessed 2 May 2015].

Inoué, Shinya, and Robert J. Walter. Video microscopy. New York: Plenum Press (1986).

Kihm, K. D., Arindam Banerjee, C. K. Choi, and T. Takagi. "Near-wall hindered Brownian diffusion of nanoparticles examined by three-dimensional ratiometric total internal reflection fluorescence microscopy (3-D R-TIRFM)." Experiments in Fluids 37, no. 6, 811-824 (2004).

Nikon MicroscopyU | Properties of Microscope Objectives. http://www.microscopyu.com/articles/optics/objectiveproperties.html [accessed May 31, 2015].

Numerical Aperture and Resolution - Olympus Micro. http://www.olympusmicro.com/primer/anatomy/numaperture.html [accessed May 03, 2015].

Olshausen, Philipp von. Total internal reflection microscopy: super-resolution imaging of bacterial dynamics and dark field imaging. PhD Thesis. Universitätsbibliothek Freiburg (2013).

_____

Pawley, James. Handbook of biological confocal microscopy. Springer Science & Business Media (2010).

Resolution and Contrast in Confocal Microscopy Resolution - Olympus Micro. http://www.olympusconfocal.com/theory/resolutionintro.html [accessed May 03, 2015].

Resolution and Contrast in Confocal Microscopy. http://www.olympusconfocal.com/theory/resolutionintro.html [accessed May 03, 2015].

Wikipedia Sakurambo, "Airy-3d" Wikipedia, The Free Encyclopedia. http://upload.wikimedia.org/wikipedia/en/e/e6/Airy-3d.svg [accessed May 4, 2015].

Wikipedia Sakurambo, "Airy-pattern" Wikipedia, The Free Encyclopedia. http://upload.wikimedia.org/wikipedia/commons/1/14/Airy-pattern.svg [accessed May 4, 2015].

_____

Research accomplishments

Publications

1. Yoshihiro Kawano, Chino Otsuka, James Sanzo, Christopher Higgins, Tatsuo Nirei, Tobias Schilling, and Takuji Ishikawa. "Expanding Imaging Capabilities for Microfluidics: Applicability of Darkfield Internal Reflection Illumination (DIRI) to Observations in Microfluidics." PloS one 10, no. 3 (2014): e0116925-e0116925.
2. Yoshihiro Kawano, Christopher Higgins, Yasuhito Yamamoto, Julie Nyhus, Amy Bernard, Hong-Wei Dong, Harvey J. Karten, and Tobias Schilling. "Darkfield adapter for whole slide imaging: Adapting a darkfield internal reflection illumination system to extend WSI applications." PloS one 8, no. 3 (2013): e58344.

Related publications

1. Richard E. Long, Adam Smith, Sam V. Machotka, Elizabeth Chlipala, Jennifer Cann, Brian Knight, Yoshihiro Kawano, Jesus Ellin, and Amanda Lowe. "Scientific and Regulatory Policy Committee (SRPC) Paper Validation of Digital Pathology Systems in the Regulated Nonclinical Environment." Toxicologic pathology 41, no. 1, 115-124 (2013).
2. Yoshiyuki Fukuda, Yoshihiro Kawano, Yoshihisa Tanikawa, Masahiro Oba, Masafumi Koyama, Hiroshi Takagi, Mineo Matsumoto, Kuniaki Nagayama, and Mitsutoshi Setou. "In vivo imaging of the dendritic arbors of layer V pyramidal cells in the cerebral cortex using a laser scanning microscope with a stick-type objective lens." Neuroscience letters 400, no. 1, 53-57 (2006).
3. Herlen Alencer, Umar Mahmood, Yoshihiro Kawano, Tadashi Hirata, and Ralph Weissleder. "Novel multiwavelength microscopic scanner for mouse imaging." Neoplasia 7, no. 11, 977-983 (2005).

International conference

1. Yoshihiro Kawano, Takuji Ishikawa. Research of extending whole slide imaging by using a Color Darkfield Internal Reflection Illumination (DIRI) for biological applications. SPIE/NIH Workshop, Biophotonics from Bench to Bedside at the National Institutes of Health. September 24-25 (2015).
2. Yoshihiro Kawano, Christopher Higgins, Yasuhito Yamamoto, Julie Nyhus, Amy Bernard, Hong-Wei Dong, Harvey J. Karten, Tobias Schilling. Adapting darkfield illumination system to extend the capabilities of whole slide imaging system and increasing image modality for brain mapping applications. The 37th Naito Conference, Bioimaging - a paradigm shift for the life sciences. July 15-18 (2014).
3. Yoshihiro Kawano, Christopher Higgins, Yasuhito Yamamoto, Julie Nyhus, Amy Bernard, Hong-Wei Dong, Harvey J. Karten, Tobias Schilling. Enhancing imaging options for brain mapping applications: Adapting a darkfield illumination system to extend the capabilities of whole slide imaging. Society for Neuroscience Annual meeting, Oct 13-17 (2012).
4. Amanda Lowe, Elizabeth Chlipala, Jesus Elin, Yoshihiro Kawano, Richard Long, and Debbie Tillman. "Validation of Digital Pathology in a Healthcare Environment." San Diego, CA: Digital Pathology Association, October (2011).
5. Richard E. Long, Adam Smith, Sam V. Machotka, Elizabeth Chlipala, Jennifer Cann, Brian Knight, Yoshihiro Kawano, Jesus Ellin, and Amanda Lowe. Validation of Digital Pathology

_____

Systems in the Regulated Nonclinical Environment. San Diego, CA: Digital Pathology Association, October (2011).

6. Yoshihiro Kawano, Nobuhiko Onda, Ikuko Sakai, Kiyotsugu Kojima. "Novel small animal imaging system and intravital laser scanning microscope help observing cellular to whole animal fluorescence images". Optical Imaging 2006, Fifth Inter-Institute Workshop on Optical Diagnostic Imaging from Bench to Bedside at the National institutes of Health. September, 25-27 (2006).

7. Yoshihiro Kawano, Chikara Abe, Katsuyuki Abe, Kazuhiro Hayashi, Yoko Hatta, and Keisuke Tamura. "Macro optical system for biological application." International Symposium on Optical Science and Technology, pp. 288-296. International Society for Optics and Photonics (2000).

8. Yoshihiro Kawano, Chikara Abe, Toru Kaneda, Yasushi Aono, Katsuyuki Abe, Keisuke Tamura, and Susumu Terakawa. "High-numerical-aperture objective lenses and optical system improved objective type total internal reflection fluorescence microscopy." In International Symposium on Optical Science and Technology, pp. 142-151. International Society for Optics and Photonics (2000).

Domestic conference

1. 東福寺幾夫、近藤 恵美、木下 善康、河野 芳弘、天川 玄太、高松 輝賢、花田 希、庄司 甲一、芹川 暁男、湯上 昌郁、小池 努、長谷川 幹夫、山田 雄二、依田 佳久、鈴木 昭俊、本村 秀人、佐藤 太一、小倉 隆、大石 英資、豊田 祐一、石下 郁夫、長門 将幸、岡村 秀樹、林 将之、遊間 顕一、笠井 啓之、王 海鷹、牧野 英哉、佐藤 圭、佐々木 毅、白石 泰三．病理診断のためのデジタルパソロジーシステム技術基準、第 1 版（Draft for Public Comment 版）、デジタルパソロジー技術基準検討会、日本デジタルパソロジー研究会（2015）

2. 河野芳弘、阿部勝行、金田徹、寺川進　対物レンズ方式全反射顕微鏡の性能向上レーザー顕微鏡研究会第 26 回講演会論文集、(2000): 40-47.

3. 藤原忠史, 塚本勝男, 島田佳弘, 河野芳弘, 高原政章, 松原正樹. "マイクログラビティーでの気相成長その場観察装置の開発." 日本結晶成長学会誌 15, no. 1 (1988): 121.

Committee member

1. White paper committee member, Digital Pathology Association, 2010-2012
2. デジタルパソロジー技術基準検討会コミッティーメンバー、日本デジタルパソロジー研究会、2014-2015